DOCTORAL THESIS IN PHYSICS

JOSEPHSON DEVICES BASED ON TOPOLOGICAL INSULATORS

ROBIN-PIERRE KLETT

CENTER FOR SPINELECTRONIC MATERIALS AND DEVICES

BIELEFELD UNIVERSITY, DEPARTMENT OF PHYSICS

Declaration of academic honesty

I hereby declare that the doctoral thesis at hand is entirely my own work and that no part of it has been written or provided by another person and that no part of it has been copied from another person's work or any other source. Additionally, I declare that all referenced work from other people is cited correctly and that it can be found in the bibliography.

Bielefeld, March 18, 2018

(Robin-Pierre Klett)

Reviewers:

Prof. Dr. Günter Reiss, Bielefeld University

Prof. Dr. Thomas Huser, Bielefeld University

Printed on non-aging paper ISO 9706

BIELEFELD UNIVERSITY, DEPARTMENT OF PHYSICS

CENTER FOR SPINELECTRONIC MATERIALS AND DEVICES

ABSTRACT

We live in the digital age. And with every passing day the digitization is progressing further. Our daily life is determined by smart devices, each equipped with dozens of sensors. They are designed to simplifiy our lives. For this purpose, huge amounts of data are gathered and have to be analyzed simultaneously. The processing and storing of these vast amounts of data are challenging in terms of clocking frequency, performance and space requirement. In modern computing architectures, current technology is going to hit its physical limit within the next few years - making demand for alternatives inevitable. This requires new materials and concepts for miniaturization.

Chipmakers started putting their hopes in *spintronics*. Unlike other state-of-the-art logic devices, this newly emerged field of research makes use of the electron spin degree of freedom and exploits it for basic logical operations. The general principle has already been demonstrated on silicon-based technology, but due to low spin-orbit coupling the devices lacked the required efficiency.

Therefore, new materials with porperties suitable for spintronic applications have to be discovered. One of the most promising examples among the candidates are *topological insulators*. These new states of matter show great potential, due to their spin-polarized surface states and an intrinsic robustness against disorder, for fu-

ture spintronic devices.

Within the framework of this thesis, superconducting devices consisting of topological insulators will be fabricated and investigated. That requires the production of crystals and thin films, the crystallographic characterization and successful patterning into devices, as well as the measurement of transport properties in both the resistive and the superconducting state. The primary focus will be given to potential "new physics" - known as *topological superconductivity* - which is predicted to appear in the investigated materials and material combinations. Topological superconductivity is expected to host new kinds of quasiparticle states: *Majorana fermions*. These special excitations are currently a prominent subject of solid state research as they might be exploited as a fundamental basis for quantum computing operations. Using devices as described in this thesis, enables one to draw conclusions about the existence of these peculiar quasiparticle states.

KEY WORDS: *spintronics, topological insulators, superconductivity, Majorana fermions*

Zusammenfassung

Wir leben im digitalen Zeitalter. Mit jedem Tag schreitet die Digitalisierung fort. Unser Alltag wird bestimmt von miteinander kommuniziernden Geräten, welche mit einer Vielzahl von Sensoren ausgestattet sind. Sie sind intelligent und sollen unser Leben vereinfachen. Die Datenmengen, welche dazu aufgenommen und zeitgleich analysiert werden müssen, sind dabei enorm. Dies führt zu extremen Anforderungen an die elektrischen Bauelemente bzgl. Taktfrequenz, Leistung und Platzverbrauch. Die momentanen Technologien stoßen dabei an ihre physikalischen Grenzen - Alternativen sind eine unausweichliche Folge. Dies verlangt nach neuen Materialien und Miniaturisierungskonzepten.
Ein Hoffnungsträger ist die *Spintronik*. Anders als bisherige Bauelemente, nutzt dieses neue Wissenschaftsfeld die quantenmechanische Spin-Eigenschaft des Elektrons für fundamentale logische Operationen. Das zugrunde liegende Funktionsprinzip wurde auf der Basis von Silizium bereits demonstriert. Aufgrund der geringen Spin-Bahn-Wechselwirkung erwiesen sich diese allerdings vergleichsweise ineffizient. Es werden daher Materialien mit besseren Eigenschaften für spintronische Bauelemente gesucht. Mögliche Kandidaten finden sich in der neuen Materialklasse der *topologischen Isolatoren*. Diese Materiezustände bieten, dank spinpolarisierter Oberflächenkanäle und intrinsischer Robustheit gegen

Störstellen, einizigartige Möglichkeiten für künftige spintronische Anwendungen.
Im Rahmen dieser Arbeit werden supraleitende Bauelemente, bestehend aus topologischen Isolatoren, konzipiert und untersucht. Dazu gehören die Herstellung und Charakterisierung der Kristalle bzw. Dünnfilme, die erfolgreiche Anwendung von angepasster Strukturierungsmethodik und die Untersuchung der elektrischen Transporteigenschaften im resistiven sowie supraleitenden Zustand.
Besonderes Augenmerk liegt dabei auf der Suche nach möglicher "neuer Physik", die sogenannte *topologische Supraleitung*, welche in den untersuchten Materialien - oder Materialkombinationen - vorhergesagt wurde und neuartige Quasiteilchen-Zustände unter dem Namen *Majorana-Fermionen* mit sich bringt. Diese besonderen Anregungen genießen in der aktuellen Festkörperphysik eine besondere Aufmerksamkeit, da sie prinzipiell als Basis für künftige Quantencomputer dienen könnten. Mit den in dieser Arbeit strukturierten Bauelementen können Rückschlüsse auf die Existenz der Quasiteilchen geschlossen werden.

Schlüsselworte: *Spinelektronik, Topologische Isolatoren, Supraleitung, Majorana-Fermionen*

Contents

Preface

"An Fortschritt glauben heißt nicht glauben, daß Fortschritt schon geschehen ist."

- Franz Kafka (∗1883 - †1924)

The pursuit of progress is one of the major driving forces behind humankind's accomplishments. The digitization of today's society is one of its outstanding examples. This technological revolution was ignited roughly fourty years ago, when in 1971 a small company named INTEL released a product known as „4004" – their first ever microprocessor[1]. The chip – being 12 *mm* in size - contained 2300 transistors, tiny electrical circuits generate the core of a computers logic as 1s and 0s. The space between each transistor unit was 10.000 *nm*, approximately the size of a human blood cell. Back in those days, the product was considered a masterpiece of miniaturization and set a new technological frontier. Today, this essay is being written on a „*Microsoft Surface 4 Pro*", working on one of INTEL's most modern chips – the Skylake, which would have rendered any scientist or inventor speechless 40 years ago. The chips themselves have grown ten times in size, but the gaps between each transistor have shrunk down to just 14 *nm*. But the main difference between both the 4004 and the Skylake can be described in terms of easy mathematical quantification: In 1965,

[1] Faggin et al. *IEEE Micro*, 16 (6):10–20, 1996

Gordon Moore, who would later become one of the founders of intel, wrote a publication noting that the number of electronic components which could be packed into an integrated circuit was doubling every year[2]. This exponential increase came to be known as *Moore's law*. In the 1970's the rate of doubling was reduced to once every two years. Even so, one would have been inconceivably optimistic to look at one of intel's 4004s in 1971 and believe that such a law would continue to hold for over four decades. But that is indeed what happened. intel does not publish transistor counts for its Skylake chips, but whereas the 4004 had 2300 of them, the company's xeon haswell E-5, launched in 2014, features over 5 billion just 22 *nm* apart[3]. The continued applicability of *Moore's law* was possible mainly due to an unusual property that transistors possess: the smaller they get, the better they become. A small transistor can be turned on and off with less power and at greater speeds than a larger one. This meant that one was able to use more and faster transistors without needing additional power or generating extra waste heat, and thus the chips could be built bigger and better. Making chips bigger and transistors smaller was no easy feat - semiconductor companies have for decades spent heavily on R&D. But each time that transistors shrank and the chips made out of them became faster and more capable, the market for them grew, allowing the makers to recoup their research costs and reinvest. The demise of this circle has been predicted many times. But now the computer industry is facing stagnation[4]. This is mainly due its components are approaching an absolute limit of smallness: the atom. A Skylake transistor is around 100 atoms across, and the fewer atoms available, the harder it becomes to store and manipulate electronic 1s and 0s. Even smaller transistors will need trickier designs and ex-

[2] Moore. *Electronics Magazine*, 38(8), April 1965

[3] Mutjaba. "intel xeon e5-2600 v3 and server processors unleashed for high-performance computing". Technical report, wccftech.com, September 2014

[4] Simonite. "intel puts the brakes on moore's law". Technical report, MIT Technology Review, March 2016

tra materials. *Moore's law* seems in danger: chipmakers are spending billions on customized designs, improved materials and better programming. But in spite of all these efforts, BOB COLWELL (former INTEL chief architect on the PENTIUM PRO, PENTIUM II, PENTIUM III and PENTIUM IV) described stagnation of the semiconductor industry in the following terms[5]:

> "OFFICIALLY MOORE'S LAW ENDS IN 2020 AT 7NM, BUT IN FACT NOBODY CARES, BECAUSE 11NM ISN'T ANY BETTER THAN 14NM, WHICH WAS ONLY MARGINALLY BETTER THAN 22NM. (...) WITH DENNARD SCALING ALREADY DEAD SINCE 2004, AND THERMAL DISSIPATION ISSUES THOROUGHLY CONSTRAIN THE INTEGRATION DENSITY - EFFECTIVLY ENDING THE MULTICORE ERA".

[5] Colwell. *Hot Chips Symposium*, 25(16035983), August 2013

This forecast is giving rise to *post-Moore technologies*[6,7]. Researchers have long started experimenting and putting their hope in a newly emerged field called *spintronics* (a portmanteau of *spin* and *electronics*)[8]. Whereas electronics uses the charge of an electron to represent information, spintronics uses the spin, another intrinsic property of electrons which is related to the concept of rotational energy possessed by an object. The digital industry already has experience with spintronics; it is used in hard drives. Research into spintronic devices started more than a decade ago. Appealingly, the voltage needed to power them is tiny: $10 - 20\,mV$, hundreds of times lower than for conventional transistors, which would solve the heat problem in one fell swoop. In recent years, a new spintronic candidate material has emerged: the *topological insulator*[9]. Topological insulators constitute a new state of matter and possess peculiar properties that make them highly attractive for chipmaker industry. The most appealing characteristic of the topological insulator is the *spin-polarized electronic states* on the material surface. The spin of electrons in one of these surface channels is fixed to a certain direction, which is determined by

[6] Waldrop. *Nature*, 530:144–147, 2016

[7] Soloviev et al. *Beilstein J. Nanotechnol.*, 8:2689–2710, 2017

[8] Savage. "a new spin on computing". Technical report, MIT Technology Review, August 2006

[9] Sato and Saitoh. *Spintronics for Next Generation Innovative Devices*. Wiley-VCG Verlag GmbH & Co., 2015

its moving direction (*spin-momentum locking*). These surface channels of topological insulators could therefore be exploited as next-generation transistors, which would be highly efficient and ultra fast compared to conventional ones. Interestingly, topological insulators exhibit additional properties of interest for industrial application when placed in close proximity to a *superconductor*. At the interface between topological insulator and superconductor new types of quasiparticles are predicted: *Majorana fermions*[10]. Despite other highly interesting physical properties (i.e. being their own antiparticles), Majorana fermions obey certain mathematical laws (non-abelian statistics) that might open the gateway to *topological quantum computing*[11]. The advantages of Majorana excitation based, fault-tolerant quantum computing are the high stability and robustness, a major bottleneck in current cutting-edge quantum technologies[12].

This thesis is dedicated to tackling these issues. Topological material candidates will be prepared and structural and electronic properties will be investigated. The main focus of electronic transport measurements is set to investigate the metallic surface states. Afterwards the materials are put in close proximity to superconducting materials - *Al*, *AlSi*, *Nb* and *Ta*. Microscopic devices are fabricated out of the topological insulator/superconductor hybrids, which are capable of identifying transport contributions of Majorana excitations. To provide the reader with a clear structure, the first part of this thesis will offer a rudimentary introduction to topological physics. It will begin with the illustration of the concepts behind topological matter and end with the presentation of material examples. The given examples are the topological insulators investigated in this thesis. In the second part the theoretical concepts of the fabricated superconducting devices will be pre-

[10] Fu and Kane. *Phys. Rev. Lett.*, 100(096407), 2008

[11] Das-Sarma et al. *npj Quantum Inf.*, 1(15001), 2015

[12] Skuse. "the trouble with quantum computing". Technical report, E&T .- Engineering and Technology, November 2016

sented, as well as a short overview of how Majorana fermions and topological superconductivity would enter the measurements. In the third and fourth part the results for various materials are presented and discussed. The last part will provide concluding remarks and an outlook on future research purposes in this field.

Part I

A Layman's Guide to Topological Physics

How Do Topology & Physics Relate to Each Other?

This chapter is intended as general introduction to the subject of topological insulators. It will give an idea of how the mathematical field of topology and condensed matter physics are linked together. This chapter is mostly written on basis of review articles by Ando & Fu[13], Hasan & Kane[14] and Ando[15]. All three reviews are highly recommended for further (and more detailed) reading as well as good starting point for beginners in the field of topological matter. They also considered a more mathematical approach to topological material. For the sake of simplicity, this introduction is written on more pedagogical niveau aiming to provide a basic understanding of the general concepts.

[13] Ando and Fu. *Annual Reviews of Condensed Matter Physics*, 6:361–381, 2015
[14] Hasan and Kane. *Rev. Mod. Phys.*, 82(3045):3045 – 3067, 2010
[15] Ando. *J. Phys. Soc. Jpn.*, 82(10200):1–32, 2013

Historical perspective

To begin with, it would prove useful to get a basic grasp on the historical background, as this will allow for greater appreciation of the impact topological insulators have had on condensed matter physics.
In solid state physics, electrons move within a periodically repeating enviroment - the *crystal structure* of a solid - and can be de-

scribed by *Bloch wavefunctions.* From a mathematical point of view, these wave functions span a *Hilbert space* - quantum mechaincal wave functions are here described by linear combinations of orthonormal vectors, creating a basis set which spans the Hilbert space. These Bloch states are the core of the *electronic band structure* of a solid, which describes the entire range of energies that an electron within this solid can possess (*energy bands*) and the range of energies it can not (*band gaps*). The highest fully occupied energy band is called the *valence band* and the lowest unoccupied or only partly occupied energy band is called *conduction band*. In this model, an electronic insulator can simply be illustrated as in *figure 1(a)* - the conduction band (CB) and the valence band (VB) are seperated by a finite energy gap (E_G). In a microscopical view of an insulator, E_G is generated through the strong localization of the valence electrons to the adjacent atomic cores, which supresses the electrical conduction.

A similar effect was discovered in 1980 by VON KLITZING ET AL.[16] in a high-mobility two-dimensinal electron gas (2DEG) semiconductor under high magnetic fields, known as *integer quantum hall effect* (QHE). The occurence of this effect is usually restricted to very low temperatures, where the localization of the electrons and the so-called *Landau quantization* of their energy spectrum lead to vanishing longitudinal conductivity, together with quantization of the Hall conductivity to integer multiplies of e^2/h when the chemical potential is located in the gap. Phenomenologically speaking the bulk electrons are localized to the atomic cores due to the Lorenz force induced by the high magnetic field B, which is expressed in nearly the same behavior as one would get for trivial insulators. The point which differentiates it from ordinary insulating states can be found at the edges. Here, electrons generate a

[16] von Klitzing et al. *Phys. Rev. Lett.*, 45(494), 1980

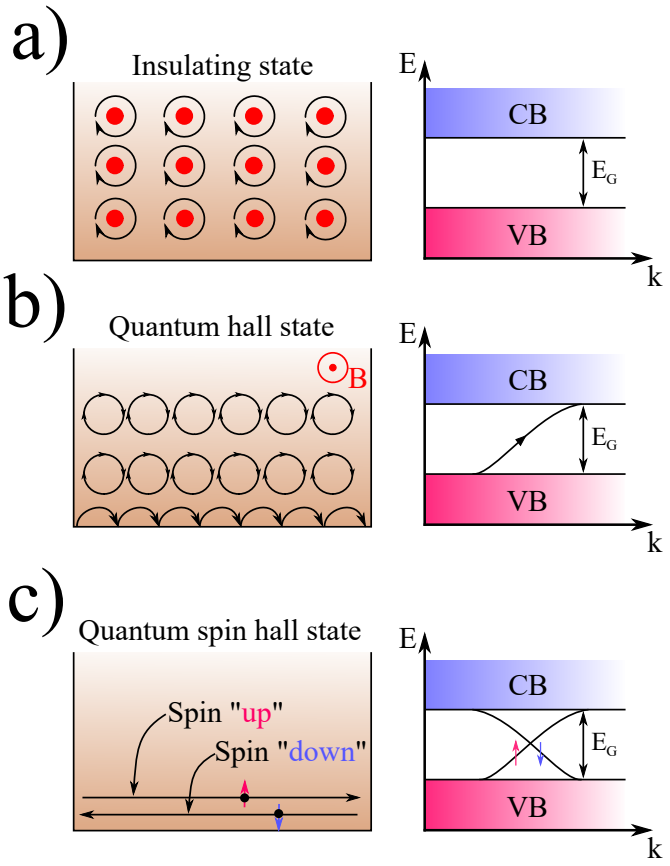

Figure 1: Illustration of the microscopic connection between a) the insulating state, b) the quantum Hall state and c) the quantum spin Hall state. Each effect is additionally pictured in a simple band dispersion model. In a) the conduction band (CB) and the valence band (VB) are seperated by an energy gap E_G. This is the same case in the quantum Hall state, but VB and CB are connected by a chiral, metallic edge state. c) demonstrates that the quantum spin Hall state is basically a copy of two quantum Hall states with spin-polarized edge channels.

closed current path between drain and source (illustrated in *figure 1(b)*). If one maps this effect onto a band structure illustration, the CB and the VB are still separated by an energy gap E_G, but with a *metallic* band connecting both electron bands. Since in the QHE the electrons in the metallic edge channels are bound to only a certain moving direction, the energy band in this illustration connects CB and VB only for $+k$ (k is the wave vector describing i.a. the moving direction of an electron). This edge transport is called *chiral*. The precise value of quantization and the strong robustness of the effect was puzzling back than, until in 1982 it was recognized by Thouless, Kohomoto, Nightingale and den

Nijs (TKNN)[17] that the effect is not only quantum mechanical in origin, but also *topological*. TKNN found that in the quantum Hall state the electrons are mapped into a *topological non-trivial* Hilbert space. This topology can be characterized by an integer topological invariant called TKNN invariant C (often named *Chern number* or *winding number*) and the Hall conductivity becomes equal to C times e^2/h. From this point of view a quantum Hall system could be considered as the first prototype of a topological material.

Concurrently, at a different front of condensed matter physics, generation and manipulation of spin currents had started to attract a lot of attention, even constituting a new field of research - *spintronics*. In this regard, the theoretical prediction[18] of the *spin Hall effect* (SHE) - the appeareance of transverse spin current in response to a longitudinal electric field - in 1970's and the experimental realization by Kato et al.[19] in 2004 promoted this field of study. The question was raised if there exists a quantized partner of the SHE analogue to the Hall effects QHE, and the idea of a *quantum spin Hall* (QSH) insulator was formed by independent proposals of Kane and Mele[20], followed by Bernevig and Zhang[21]. Essentially, QSH insulators consist of two copies of a quantum Hall system in which the chiral edge states are *spin-polarized* (as illustrated in *figure 1(c)*). In 2006 Bernevig, Hughes and Zhang[22] came up with a concrete QSH insulator candidate: a $CdTe/HgTe/CdTe$ quantum well. This guess was verified only one year later in 2007 by König et al. They observed a quantized value of $2e^2/h$ in the longitudinal conductivity in zero magnetic field when the chemical potential was tuned in the bulk band gap of the system.[23]. This was the first experimental proof of a 2D *topological insulator* (TI) and it heralded the quest for further topological materials.

[17] Thouless et al. *Phys. Rev. Lett.*, 49(405), 1982

[18] D'yakonov and Perel. *JETP Lett.*, 13:467, 1971

[19] Kato et al. *Science*, 306 (1910), 2004

[20] Kane and Mele. *Phys. Rev. Lett.*, 95(146802), 2005

[21] Bernevig and Zhang. *Phys. Rev. Lett.*, 96(106802), 2006

[22] Bernevig et al. *Science*, 314(1757), 2006

[23] König et al. *Science*, 318 (766), 2007

Topological Material: Basic Considerations

As mentioned in the previous section, with the experimental realization of a 2D TI science started the systematic search for other topological matter candidates. But how could this be done? This section will illustrate the rough principle of how theory is able to predict new topological materials.

As discussed earlier, topology is entering physics by means of the non-trivial topology of an underlying Hilbert space, which is formed via the Bloch wavefunctions of a solid state system. Therefore, the calculation of the band structure of desired materials is a plausible point to start. For this task, computational physics (i.e *density functional theory* (DFT)) has been proven to be a powerful tool[24]. For computational physicists in the field of semiconductor physics it is uncommon to express a calculated energy band gap E_G as we did above (as energy difference between CB and VB), but rather as

$$E_G = E_s - E_p. \tag{1}$$

Here, E_s and E_p describe the energy bands which are generated by *s-orbital* and *p-orbital* electrons, respectively. In many cases both definitions of E_G are identical, because generally the s-electrons form the CB and the p-electrons define the VB. These cases are topologically trivial. But for topologically non-trivial material this results in a formally *negative bandgap energy* and a so-called *inverted bandstructure,* as demonstrated in *figure 2*, because the p-orbital states push above the s-orbital bands. The inverted bandstructure is a direct relativistic consequence of alloys consisting of *heavy elements,* and therefor show intrinsically high *spin-orbit coupling*. An inverted bandstructure is necessarily linked to topo-

[24] Weng et al. *MRS Bull.*, 39 (10):pp. 849–858, 2014

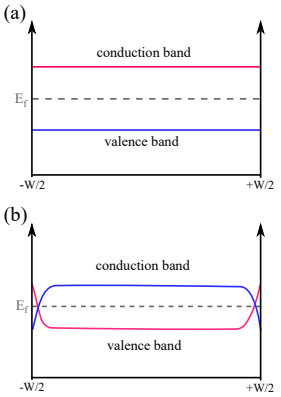

Figure 2: In (a) a trivial insulator band state is portrayed, in which the conduction band consists of electron s-states (pink) and the valence band of p-states (blue). (b) depicts an inverted bandstructure.

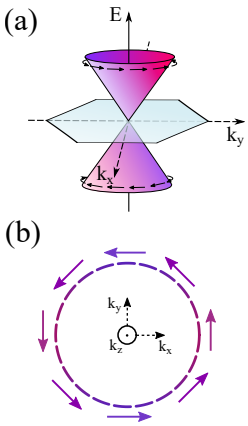

Figure 3: In (a) the surface state Dirac cone of a 3D topological insulator is illustrated. (b) shows a constant-energy cut through the dirac cone to depict the principle of spin-momentum locking.

logical non-trivial surface states, which manifest themselves at the boundary to a trivial insulator. This can be explained by taking a look at *figure 2(b)*. At the interface between topologically non-trivial to a topologically trivial material the energy bands need to be continously deformed into each other and necessarily have to cross (this holds for 2D as well as 3D). These crossings form one of the most prominent features of TIs - the surface *dirac cone.*

Dirac cones describe massless fermions (they share the same linear energy-momentum dispersion as photons) resulting in charge carriers with ultra high mobilities and are thus promising for future electronics. An illustration of a dirac cone in a 3D TI is given in *figure 3(a)*. In addition to these high carrier mobilities, topological surface states (TSS) possess additional properties: *spin-momentum locking* and *symmetry protection*. Spin-momentum locking (SML) means that the spin of a carrier is directly pinned to the moving direction. This is effect is demonstrated in *figure 3(b)*. It shows a constant-energy cut through a TSS Dirac cone and, depending on the k-point of the energy-contour, the carrier spin is pointing a fixed direction orthogonormal to k. Due to SML, TSSs are attractive for potential computer based electronic applications, as they were already demonstrated to be highly energy efficient memory logics in ferromagnetic TI hybrid devices[25,26,27]. Symmetry protection of TSSs is another property beneficial for future electronic applications. Essentially it means that in theory the TSSs cannot be destroyed by intrinsic or extrinsic crystalline defects or imperfections. And as long as the impurities are non-magnetic, the charge carriers in the TSSs are immune to elastic backscattering. Due to both these characteristics TSSs are called *robust*[28]. As will be discussed later in more detail, this robustness is a consequence of inherited underlying (global) symmetries.

[25] Fan et al. *Nat. Mater.*, 13: 699–704, 2014
[26] Dankert et al. *Nano Lett.*, 15: 7976–7981, 2015
[27] Yang et al. *Phys. Rev. B*, 94 (075304):1–10, 2016

[28] Moore. *Nature*, 464:194–198, 2010

Topological States of Matter - An Overview

In this chapter, different classes of topological matter will be discussed and what similarities, as well as differences, exist between them. Furthermore, two distinct classes - *topological insulators* and *topological crystalline insulators* - will be singled out and described in more detail, because both these topological species will be the matter of choice in the experiments presented in this thesis. The chosen materials will be introduced and the preperation and the initial characterization of the samples will be presented.

Topological Classification of Condensed Matter

Since the observation of the first TI a decade ago, the catalogue of newly discovered and proposed topological material is flourishing. This was mostly possible because of a successfully developed theory of TIs in terms of symmetry and resulting invariants. For 3D TIs *time-reversal symmetry* results in the $\mathbb{Z}_2$ invariant ν - which can be considered as Chern number C of the *Berry phase*. These $\mathbb{Z}_2$ invariants were found to be powerful tools, because they opened the gates to high throughput material prediction. But despite all these success, a years later the topological characterization by only

$\mathbb{Z}_2$ invariants was found insufficient. The reason for this is that it focused only on certain symmetries. Ideas came up that taking additional symmetries into account might lead to further topological branches. A famous example is the *topological crystalline insulator* (TCI), which is protected by *reflection symmetry* rather than time-reversal symmetry. At the point of writing only few topological phases have been discovered and it is likely that the next years will reveal many more. For this thesis only samples from two topological phases are investigated: the 3D ($\mathbb{Z}_2$) TI and the TCI. Both classes are in the following introduced in more detail and a representative compound example will be given.

Time-Reversal Symmetry Protected Topological Insulators

As mentioned previously, 2D TIs can be classified in terms of a new topological invariant $\mathbb{Z}_2$, which is (roughly speaking) the number of Dirac cones lying within the 1. Brillouin zone of a given material. When this number is odd (even), the $\mathbb{Z}_2$ invariant of the material is topological non-trivial (trivial). But until this point, a single $\mathbb{Z}_2$ invariant was always taken to be sufficient in defining the topological state. But this only holds for the specific cases of two dimensions or less. To classify TIs in 3D one has to take 4 invariants into account, distinguishing between 16 subphases within two general classes: weak TIs (WTI) and strong TIs (STI)[29]. WTI can be viewed as layered 2D QSH systems and can be destroyed by disorder, whereas STI represent the 3D version of 2D TIs. The mathematical reason for the additional invariants is that in 3D one finds 8 distinct time-reversal-invariant momenta (TRIM), which can be expressed in terms of primitive reciprocal

[29] Fu, Kane, and Mele. *Phys. Rev. Lett.*, 98(106803):pp. 1–4, 2007

lattice vectors as

$$\Gamma_{i=(n_1 n_2 n_3)} = (n_1 b_1 + n_2 b_2 + n_3 b_3)\,, \tag{2}$$

with $n_j = 0, 1$. The 4 $\mathbb{Z}_2$ invariants ν_0; $(\nu_1\nu_2\nu_3)$ are defined as

$$(-1)^{\nu_0} = \prod_{n_j=0,1} \delta_{n_1 n_2 n_3}, \tag{3}$$

$$(-1)^{\nu_{i=1,2,3}} = \prod_{n_{j\neq i}=0,1;\, n_i=1} \delta_{n_1 n_2 n_3}. \tag{4}$$

The $\nu_0 = 0$ states describe the WTI. These topological states are highly sensitive due to their dependence on translational symmetry. Disorder is predicted to easily destroy them, which is the reason why they are referred to as *weak*. The $\nu_0 = 1$ phases are more robust and are consequently referred to as *strong*. All 3D TIs investigated in this thesis belong to the STI phase.

Although the most investigated and successful representatives of 3D TIs are $HgTe$, Bi_2Se_3 and Bi_2Te_3[30], there exists a variety of other systems. One of the most versatile platforms beneath them is the family of *half-Heusler materials*. Heusler compounds are intermetallics with a *face-centered cubic* crystal structure and a composition of XYZ (*half-Heuslers* or *ternary Heuslers*) or X_2YZ (*full-Heuslers*), where X and Y are transition metals and Z is an element from the p-block. Both crystal structures are illustrated in *figure 4*. Many of these compounds exhibit widespread physical properties i.e. ferromagnetism, semimetallicity or superconductivity.

In 2010 Chadov et al.[31] and Lin et al.[32] proposed, based on *ab initio* studies and independently from each other, half-Heusler alloys as promising platforms for topological materials. Due to their close relatedness to HgTe (both belong to the $F\bar{4}3m$ space group), (odd-numbered) bandinversions at the Γ-point were predicted for several half-Heuslers with sufficently heavy constituents, i.e. *YPtBi* and *LuPtBi*, which are the two half Heusler systems investigated in this thesis. A "periodic table" of potential ternary Heuslers with negative band gap is illustrated in *figure 5*. Since all the possible candidates in this class are *zero bandgap semiconductors*, it is more appropriate to speak of *topological semimetals* (TSM) instead of TIs. However, soon after the theoretical prediciton several experimental smoking gun experiments were performed, showing *Shubnikov-de-Haas oscillations*[33], pronounced *weak antilocalization*[34] and non-saturating *magnetoresistance*[35] effects - all of which are indicators of ultrahigh surface carrier mobilities and therefore TSS. In 2016 the TSS of a half-Heusler TSM could be obeserved directly for the first time via ARPES (angle-resolved

[30] Zhang et al. *Nat. Phys.*, 5: 438–442, 2009

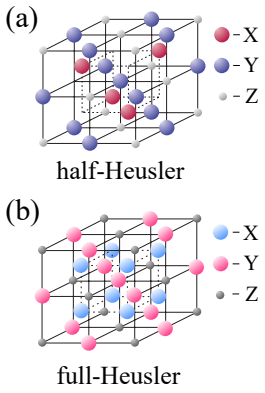

Figure 4: The crystal structures of Heusler compounds. (a) shows a half-Heusler alloy ($C1_b$ structure, $F\bar{4}3m$ space group). Figure (b) depicts the full-Heusler crystal structure ($L2_1$ structure, $Fm\bar{3}m$ space group).

[31] Chadov et al. *Nat. Mater.*, 9:541–545, 2010
[32] Lin et al. *Nat. Mater.*, 9: 546–549, 2010

[33] Wang et al. *Sci. Rep.*, 3 (2181):pp. 1–7, 2013
[34] Xu et al. *Sci. Rep.*, 4(5709): pp. 1–7, 2014b
[35] Hou et al. *Phys. Rev. B*, 92 (235134):1–9, 2015

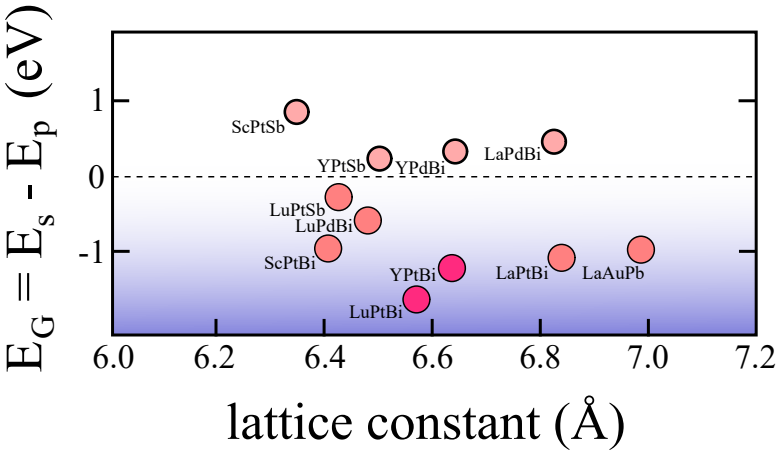

Figure 5: Illustration of the band gap energy in dependence of the lattice constant of half-Heusler systems. The alloys with negative band gap energies are expected to be topologically non-trivial. *YPtBi* and *LuPtBi* share the strongest band inversion within the given systems.

photoemission spectroscopy) by Lu et al.[36].

Even if the absence of a band gap in this material constitutes a major drawback for computational application devices, a huge advantage of the half-Heuslers is their diversity. In addition to their non-trivial topology, *YPtBi*[37] and *LuPtBi*[38] are reported to host unconventional superconductivity at $T < 1\,K$, making them *topological superconductor* candidates.

[36] Lu et al. *Phys. Rev. B*, 94 (014504):1–9, 2016

[37] Butch et al. *Phys. Rev. B*, 84 (220504):pp. 1–5, 2011

[38] Tafti et al. *Phys. Rev. B*, 84 (184504):pp. 1–5, 2013

Sample Preperation

The bulk single crystals used in this thesis are grown by Shekhar et al. at the Max-Planck-Institute for chemical physics of solids in Dresden. *YPtBi* and *LuPtBi* single crystal pieces are grown via the solution growth method. During growth, Bi acts as flux. Stoichiometric quantities of freshly polished pieces of *Y* or *Lu*, *Pt*, and *Bi* with a purity $> 99.99\,\%$ in atomic ratio of 0.5 : 0.5 : 10 for *Y* and 0.3 : 0.3 : 10 for *Lu* are put into *Ta* cruciables sealed within dry quartz ampoules under $3\,mbar$ partial argon pressure. The filled ampoules are heated at a rate of $100\,K/h$ to $1473\,K$, followed by 12 hours of soaking. For ideal

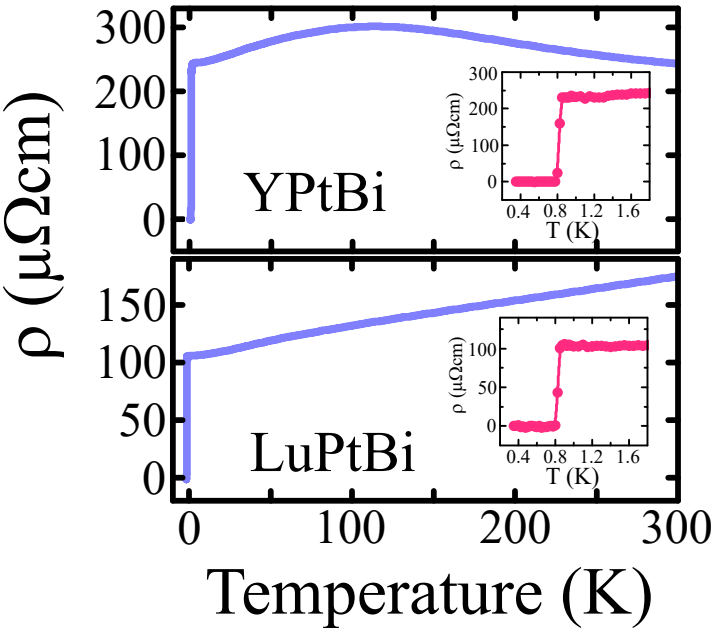

Figure 6: The temperature-dependent resistivity of *YPtBi* and *LuPtBi* single crystals. Each inset shows the zoom-in near T_c.

crystal growth, the temperature is slowly reduced by $2\,K/h$ to $873\,K$ and the surplus of *Bi* flux is removed by decanting the ampoules at $873\,K$. This procedure succeeds in triangular shaped crystals with preferred growth in (111) direction and a size of $4-5\,mm$. Shekhar et al.[39] checked the crystals for stoichiometry via energy dispersive x-ray analysis and the crystal structures are investigated by Laue x-ray diffraction. Electronic transport measurements of the single crystals confirmed the superconducting phase transition with $T_c < 1\,K$ (*figure 6*). Further Hall analysis in the temperature range $2-300\,K$ yield extremely high carrier mobilities and magnetoresistance effects of $\sim 300\,\%$. As a result of the linear Hall dependency, the conductivity is predominantly governed by holes. In conclusion, the electronic and structural analysis mirror the good sample quality and form a promising foundation for superconducting devices investigated in this thesis.

[39] Shekhar et al. *arXiv preprint*, arXiv:1502.00604v2, 2015b

Mirror Symmetry Protected Topological Matter - The Topological Crystalline Insulator

In 2012 Hsieh et al. published a paper[40] in which they predicted a new type of topological insulator class - the *topological crystalline insulator* (TCI). In this new generation of topological matter, the topological non-trivial nature of the electronic band structure arises from fundamental crystal properties. They found that non-trivial band inversions occur in the IV-VI semiconductor family with rock salt-type face centered cubic crystal structure (illustrated in *figure 7*).

[40] Hsieh et al. *Nat. Commun.*, 3(982):1–6, 2012

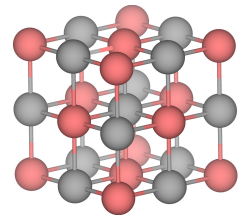

Figure 7: Illustration of the face centered cubic rock salt-type crystal structure of *SnTe*. The *Sn* atoms are depicted in pink and the *Te* atoms in grey.

The overall sum of these bandcrossings per Brillouin zone (BZ) is even and therefore the introduced $\mathbb{Z}_2$ is trivial, but if one considers mirror symmetry even-numbered, robust surface Dirac cones occur on all surfaces symmetrically about (110) *mirror planes* - which are $\{001\}, \{110\}$ and $\{111\}$- as depicted in *figure 8*. This can be pictured by considering the plane $\Gamma L_1 L_2$ in momentum space (illustrated in light red in *figure 8*). All crystal momenta on this plane are invariant under reflection with respect to the $\{110\}$ planes in real space. Mathematically this allows labelling of the Bloch wavefunctions by their eigenvalues $\pm i$ under mirror operation $\mathcal{M}$, still respecting $\mathcal{M}^2 = -1$ for spin $1/2$ systems. Each class of $\mathcal{M} = \pm i$ eigenstates can be associated to a specific Chern number $\nu_{\pm i}$ and the adjacent mirror Chern number is then defined by $\nu_M = (\nu_{+i} - \nu_{-i})/2$. Provided present mirror symmetry, ν_M is an integer-valued new topological invariant. A non-zero mirror Chern number defines the TCI state of matter.

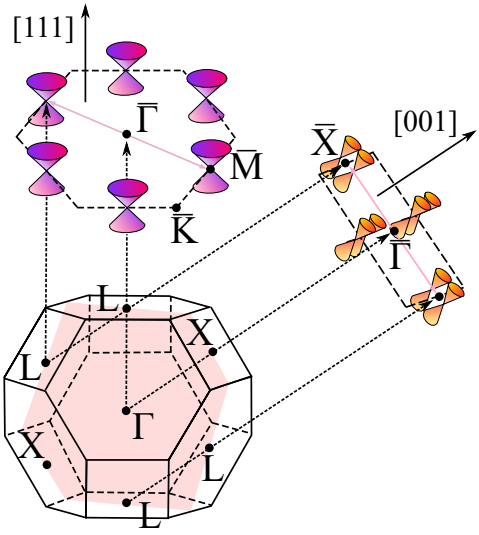

Figure 8: Illustration of the Brillouin zone of TCI and relevant high symmetric crystal momenta L, X, M and Γ. The (110) mirror plane (marked in pale red) gives rise to protected TSS along the [111] and [001] crystal orientations. The directions differ in their surface state properties.

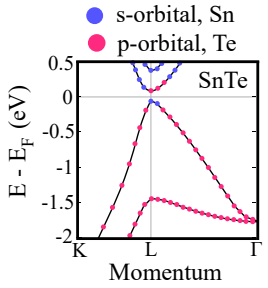

Figure 9: Electronic structure of *SnTe* in vicinity of the *L*-point indicating the bandinversion and the topologically non-trivial phase.

[41] Hsieh et al. *Nat. Commun.*, 3(982):1–6, 2012
[42] Tanaka et al. *Nat. Phys.*, 8: 800–803, 2012

SnTe - A Topological Crystalline Insulator

The theoretical prediction of Hsieh et al.[41] was proven in the very same year with the realization of the first TCI in the suspected candidate *SnTe* by Tanaka et al.[42]. Their angle-resolved photoemission spectroscopy (ARPES) experiments conducted on *SnTe* single crystals revealed the signature of metallic Dirac-cone surface bands, with the Dirac point slightly offset from the edge of the Brillouin zone.

SnTe belongs to the *IV-VI* semiconductor class and is a narrow band gap semiconductor with the *VB* maximum and *CB* minimum at four equivalent L points of the BZ. Orbital projected *ab initio* calculations show the inverted band structure at these points (*figure 9*). At this point the equal number of band crossings per BZ - and thus a trivial $\mathbb{Z}_2$ invariant - should be noted. As mentioned above, the non-trivial topology arises in this system if one takes the mirror symmetric face centered cubic crystal symmetry of the rock salt-type system into account. One may argue at this

point that in *SnTe* the well-known problem of rhombohedral distortion[43] would break the mirror symmetry with respect to the (110) plane and destroy the non-trivial bandstructure. The rhombohedral transition temperature is found sensitive to the carrier density and would manifest as a kink in the temperature dependence of the resistivity. Furthermore, i.e. the (001) plane of the cubic structure has two mirror planes, and the rhombohedral distortion breaks the mirror symmetry of only one of those two mirror planes. This means that two of the original four Dirac cones remain gapless even in the rhombohedral phase. In addition, as the rhombohedral distortion in *SnTe* is comparably weak (it induces only 1.6 displacement of the atomic positions[44]), the expected result is a small gap opening at the Dirac point in the other two cones. But density functional calculations so far suggest that the entire electronic structure remains topologically non-trivial up to a lattice distortion of roughly 4.1 [45]. Therefore, the small rhombohedral distortion, even if it happens to occur, would not significantly alter the surface state spectrum. Due to its simple cubic rock salt-type crystal structure and non-toxic constituents, *SnTe* can be seen as an ideal platform for growing TCI thin film samples.

[43] Iizumi et al. *J. Phys. Soc. Jpn.*, 38:443–449, 1975

[44] Iizumi et al. *J. Phys. Soc. Jpn.*, 38:443–449, 1975

[45] Hsieh et al. *Nat. Commun.*, 3(982):1–6, 2012

Sample Preperation

The *SnTe* samples investigated in this thesis are prepared via co-sputtering of *Sn* and *Te* in a BESTEC 3-inch target sputtering system. The thin films are grown on MgO (001) substrates as well as on wafers of $Si(001) + 50\,nm$ thermally oxidized amorphous SiO_2. The base pressure of the sputter system is $p \sim 5 \cdot 10^{-10}\,mbar$, the *Ar*-pressure is $p \sim 2.5 \cdot 10^{-3}\,mbar$. As shown in *figure 10*, *x-ray diffraction* (XRD) measurements in $\Theta - 2\Theta$ geometry clearly produce only the (002) and (004) diffraction peaks for films of $40\,nm$

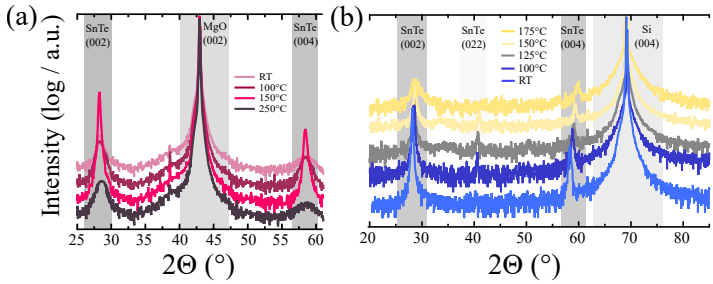

Figure 10: XRD measurements of co-sputtered 40 nm (002) orientated SnTe thin films for several deposition temperatures on (a) MgO and (b) $Si + SiOx$ substrates. The best film quality is obtained at $T_D = 150°C$ and $T_D = RT$ for MgO and Si, respectively.

thickness without any observable sub-phases . As indicated in the temperature series, the best crystal quality is obtained under deposition temperatures of $T_D = 150°C$ for growth on MgO substrate and room temperature (RT) for the growth on Si. The stoichiometry of the films is $49.1 \pm 1.1\%$ Sn and $50.9 \pm 1.9\%$ Te, checked by both *x-ray fluorescence* (XRF) as well as *energy dispersive x-ray* (EDX) spectroscopy. For higher temperatures the samples exhibited in higher roughnesses, crystallic sub-phases of $SnTe$ and optical defects. We attribute these effects to degassing of Te. Because of this, we carefully take $T = 140°C$ as the upper temperature limit in later patterning steps of the $SnTe$ thin films.

Atomic force microscopy (AFM) images of 40 nm $SnTe$ films on (a) MgO and (b) Si, both samples deposited under individually best growth conditions, are presented in *figure 11*. The data indicates that the films grow smoothly on the adjacent substrate, resulting in averaged rougness values of $RMS_{MgO} = 0.48nm$ and $RMS_{Si} = 0.27nm$. Several groups[46,47] have already pointed out that smooth surface texture and low roughness values are necessary conditions for TSS. Further proof for the low roughness of the $SnTe$ films are illustrated in the line scans, which are measured at the colored arrow within the neighboring AFM image, showing only slight changes in height across widths in μm range. (c) shows the height distribution of both films. The data shows that over the entirety

[46] Wand et al. *Nano Res.*, 3(12): 874–880, 2010
[47] Zeljkovic et al. *Nat. Phys.*, 10:572–577, 2014

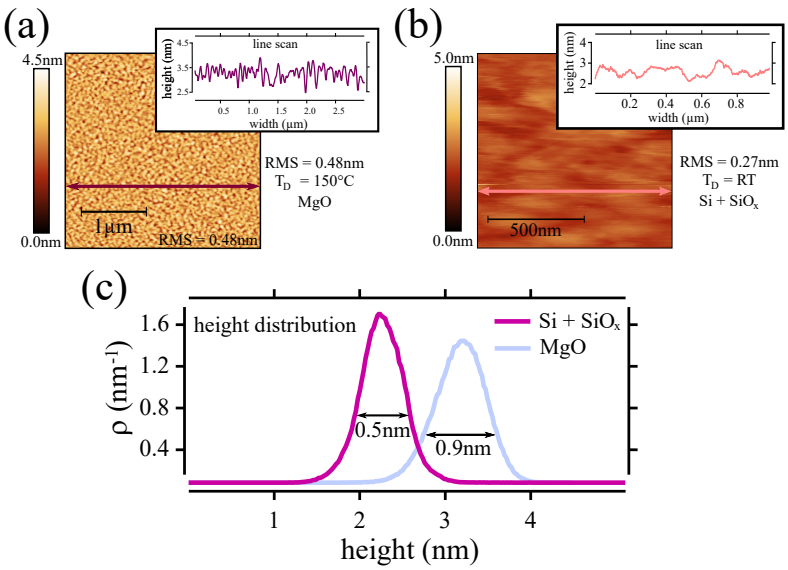

Figure 11: AFM data taken at 40 *nm* *SnTe* thin films grown on (a) *MgO* and (b) *Si* with 50 *nm* of amorphous *SiOx*. On both substrates the *SnTe* films possess smooth surfaces with *rms* values of 0.47 *nm* and 0.25 *nm* for *MgO* and *Si* respectively. (c) shows the height distribution of both film systems, each deposited under best growth conditions. The *SnTe* films grown on *Si* possess less variation in their surface profiles.

of the measured surface area, the average change in height is beneath 1 *nm* (0.9 *nm* for *MgO*, 0.5 *nm* for *Si*).

Texture measurements done with an Euler cradle along the (002), (202) and (222) crystal planes are provided in *figure 12*. The (002) measurement gives only one pronounced peak at $\Psi = 0°$, stemming from the strong [001] texture previously discussed regarding the XRD scans. Interestingly, the (202) and (222) scans show ring-like patterns, which means that the films are formed by [001] textured polycrystals. The fourfold symmetric ($\varphi = 45°$, $\varphi = 135°$, $\varphi = 225°$ and $\varphi = 315°$) peaks lying on the $\Psi = 45°$ ring show that the prevalent part of the crystals is growing along the [110] direction of the *MgO*. This matches the expectation, as the $\sqrt{2}\, a_{MgO} = 0.593\, nm$ diagonale results in the lowest lattice mismatch of roughly 6 % to the *SnTe* lattice constant $a_{SnTe} = 0.63\, nm$. This is further supported by the (222) scan. Once again, the ring-shape pattern with fourfold degenerated peaks at $\varphi = 0°$, $\varphi = 90°$,

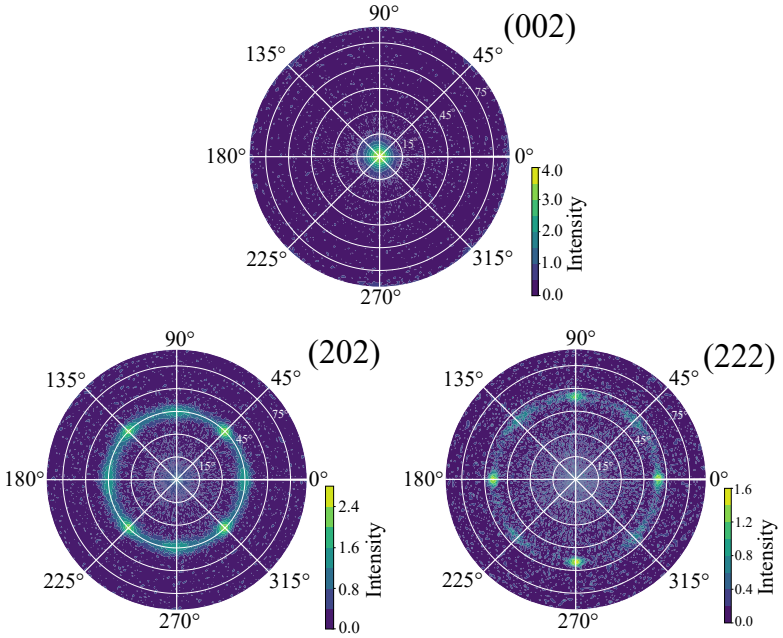

Figure 12: Pole figure measurements of the (002), (202) and (222) planes at *SnTe* thin films grown on *MgO* (001) substrate. The scans illustrate polycrystalline film growth with strong [001] texture only and show that *SnTe* grows 45° tilted with respect to underlying *MgO*. Measurements done at films deposited on *Si* substrate show similar textures and growth.

$\varphi = 190°$ and $\varphi = 270°$ can be observed. Slight impacts from crystals, which grow 45° tilted to the [110] MgO direction, can be identified by smaller intensity peaks.

To further support the texture measurement data, lamellas from a $MgO/SnTe/Nb/Ta/Ru$ thin film system are cut along the [100] direction of the *MgO* substrate and investigated via *transmission electron microscopy* (TEM) measurements. *Figure 13(a)* provides a TEM overview image of such a multilayer system, which shows a clear resolution of each individual layer. As expected from the texture measurements in *figure 12* the *SnTe* grows in strongly [001] textured crystal grains on top of the *MgO*. The average grain size in in-plane growth direction is $d_{ip} = 27\,nm$ (averaged over several crystallites from different images). In growth direction the crystallites match the film thickness and show single crystalline growth. *Figure 13(b)* shows a close-up image of a grain boundary between

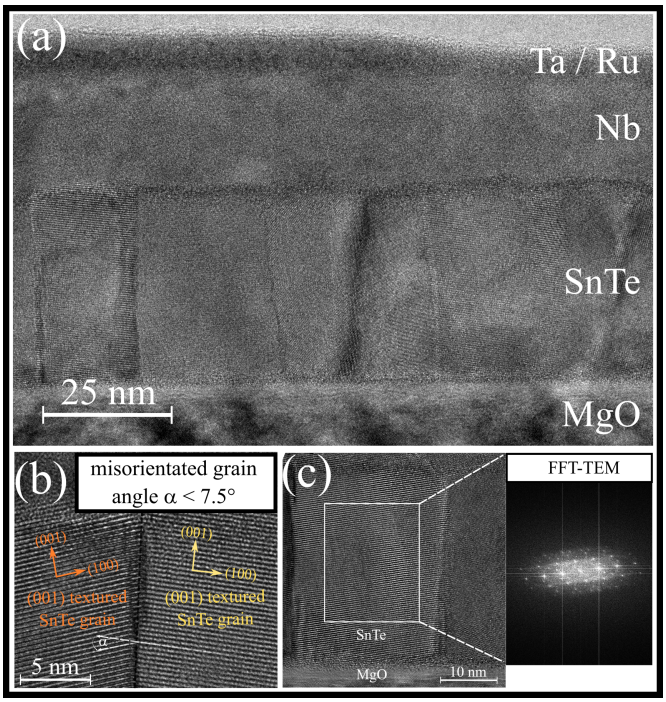

Figure 13: (a) TEM profile image of a *MgO/SnTe/Nb/Ta/Ru* thin film system lamella showing [001] textured growth of *SnTe* polycrystals with an average in-plane grain size of 27 *nm* and a homogenous single crystalline formation in growth direction. (b) close-up image of a grain boundary between two SnTe grains. The grains are misaligned by a small angle $\alpha < 7.5°$. (c) shows another *SnTe* crystal and the adjacent FFT-TEM image. The highly symmetric peaks show the high crystal quality of the individual *SnTe* grains.

two high textured SnTe grains. The single crystallites are tilted by an angle $\alpha \approx 7.5°$ to each other. In *figure 13(c)* a close up of a *SnTe* single crystallite is shown. The FFT-TEM image, created from the data within the white rectangle, shows highly ordered and symmetric peaks, and thus provides further evidence of the crystal quality of the individual *SnTe* grains.

Electrical Characterization

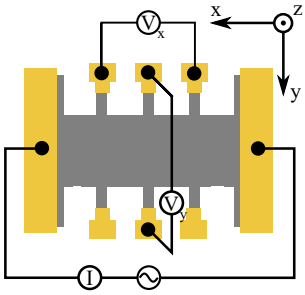

Figure 14: Illustrated Hall bar design of the investigated *SnTe* microstructures. The measurements are done in constant current 4*W DC* geometry.

The transport properties of the bare *SnTe* thin films are investigated using micro-patterned Hall bar devices. The micostructures are defined by conventional *UV*-lithography and dry etched by Ar^+ ion milling. An illustration of the fabricated Hall structures is shown in *figure 14*.

The resistivity of *SnTe* is measured in established *4 wire method* (4*W*) while cooling the Hall bar from RT ($T = 300\,K$) down to $T = 2\,K$. Despite of *SnTe* being a narrow band gap semiconductor, the films show entirely metallic behavior, as can be seen in *figure 15(a)*. It is important to mention that in the temperature window between $T = 2 - 120\,K$ no considerable kink in resistivity is observed. Therefore, we argue that the rhombohedral lattice distortion has no considerable influence on the electronic transport in the investigated samples. For further characterization, Hall measurements taken in the same temperature window show that the transport is governed by holes with fairly high carrier concentration of $n_h = 1.1 \cdot 10^{21} cm^{-3}$ at $2\,K$ to $n_h = 9.5 \cdot 10^{20} cm^{-3}$ at $300\,K$ (the dependence of the carrier densities is depicted in *figure 15(b)*). As *SnTe* is known to tend intrinsically to high carrier concentrations due to *Sn* vacancies (and hence to *p-type* character), the results are consistent with current reports of other reseachers[48]. The atypical behavior of decreasing n_h with increasing T is attributed to hopping transport activated by grain-boundary trapping, which is reported to govern the electronic transport of polycrystalline thin films[49]. In addition, the high carrier densities explain the metallic transport behavior of the *SnTe* films. From the measured charge carrier densities, one can further estimate the average fermi velocity v_F of the charge carriers in the system (shown in purple in *figure 15(b)*). The measured fermi velocities

[48] Mengui et al. *Braz. J. Phys.*, 36(A2):pp. 324–327, 2006

[49] Schuler. *Transport properties and defects in polycrystalline $CuGaSe_2$ thin films and heterostructures*. Phd thesis, FU Berlin, 2002

of $v_F = 3.65 \cdot 10^5 ms^{-1}$ at $T = 2\,K$ for the *SnTe* thin films match the values predicted for the Dirac velocity $v_D = 1.7 \cdot 10^5\, ms^{-1}$ of [001] orientated *SnTe* by *ab initio* calculations[50], giving indication of strong TSS transport contribution. An established all-electrical method of testing the presence of TSS transport are measurements of the longitudinal magnetoresistance (MR), where *weak antilocalization* (WAL) is expected due to surface states[51]. The MR data shown in *figure 15(c)* ais plotted in relative change of *magnetoconductivity* $\Delta\sigma_{2D} = \sigma(B) - \sigma(0)$ and show sharp cusp-like MR, which can indeed be attributed to WAL and evaluated with the Hikami-Larkin-Nagaoka (HLN) formalism

$$\Delta\sigma_{2D} = \alpha_0 \frac{e^2}{2\pi^2\hbar}\left(ln\left(\frac{\hbar}{4eBL_\phi^2}\right) - \psi\left(\frac{1}{2} + \frac{\hbar}{4eBL_\phi^2}\right)\right), \qquad (5)$$

where e is the electron charge, $\hbar$ is the Planck's constant, L_ϕ is the *phase coherence length* of a charge carrier in a given surface channel, $\psi(x)$ is the *digamma function*, B is the out-of-plane applied magnetic field and α_0 is a dimensionless *transport parameter* [52]. Data fitting in the low magnetic field region (indicated by the greyish box) yields information about L_ϕ and α_0, both of which are plotted as function of temperature T in *figure 15(d)*. L_ϕ is increasing steadily with decreasing T from $L_\phi = 20nm$ at $20\,K$ to $L_\phi = 120nm$ at $2\,K$, the same order of magnitude as found for other topological materials[53,54].

Interestingly, the coherence length we obtain from the WAL data is much larger than the average grain size of the bulk *SnTe* (observed in TEM images in the *structural characterization* section). Thus, it is well justified to attribute the value of $120\,nm$ to the surface conduction channels. The theoretical prediction of α_0 is supposed to yield $\alpha_0 = -0.5$ for one TSS contributing to transport[55]. As shown in *figure 15(d)*, fitting our data with eq.5 results in $\alpha_0 \approx -0.5$ over

[50] Hsieh et al. *Nat. Commun.*, 3(982):1–6, 2012

[51] Hikami, Larkin, and Nagaoka. *Progress in Theoretical Physics*, 63(2):pp. 707–710, 1980

[52] He et al. *Phys. Rev. Lett.*, 106(16)(166805):1–5, 2011

[53] Zhao et al. *Sci. Rep.*, 6 (22377), 2016

[54] Shekhar et al. *arXiv preprint*, arXiv:1502.00604v2, 2015b

[55] Hikami, Larkin, and Nagaoka. *Progress in Theoretical Physics*, 63(2):pp. 707–710, 1980

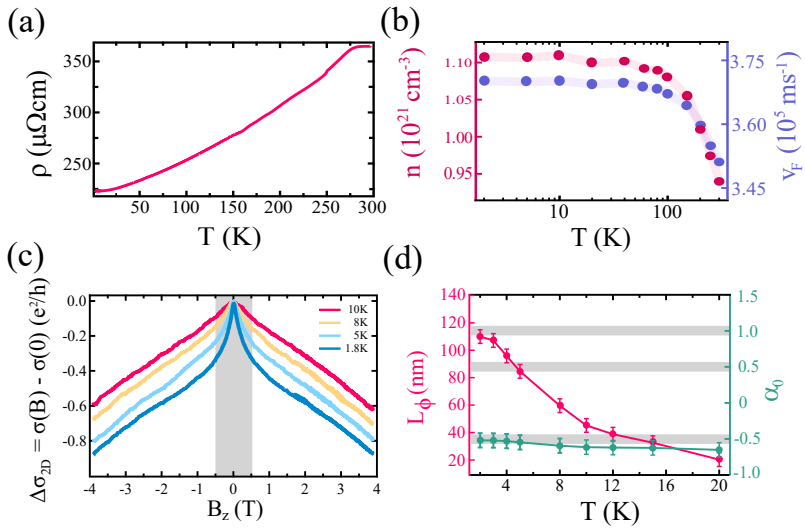

Figure 15: (a) Temperature dependence of the *SnTe* resistivity ρ between $T = 2 - 300\,K$, showing metallic-like behavior. (b) shows the dependence of the charge carrier concentration n and the fermi velocity v_F in the same temperature window as (a). (c) shows the relative longitudinal magnetoconductivity $\Delta\sigma$ as function of an out-of-plane magnetic field B_z, demonstrating weak antilocalization. (d) shows the temperature dependence of L_ϕ and α_0 yielded by fitting (c) with the HLN formalism.

the entire temperature range demonstrating topological transport. Anyhow, four TSS exist on the surface BZ of a TCI, each entering with an additional $\alpha_0 = -0.5$ contribution. If one considers that TSS occur on the top and the bottom interface, one would end up with a sum of $|\alpha_0| = 4$ [56]. A plausible explanation of measuring only a single TSS contribution per surface is due to *valley degeneracy* of the *SnTe* surface BZ, giving rise to two different coupling scenarios: *intra-* and *inter-surface valley coupling*. The first effect can be observed when a carrier is able to scatter coherently between Dirac valleys located on the same surface. Accordingly, a long coherence length results in string intra-valley coupling and thus a smaller α_0. Similar behavior is typically observed for other Dirac valley materials like graphene[57]. The second scatter mechanism is inter-surface valley coupling between bottom and top surface valleys. In this coupling regime charge carriers can scatter coherently between the top and bottom surface BZ Dirac valleys via bulk channels. This scenario has been observed by several

[56] Akiyama et al. *Nano Res.*, 9 (2):pp. 490–498, 2016

[57] Wu et al. *Phys. Rev. Lett.*, 98 (136801):1–6, 2007

other groups[58,59,60] and was attributed to the high bulk carrier concentration of *SnTe*. However, since WAL is predominantly a 2D phenomenon, the bulk bands are unlikely to be the origin of the WAL[61]. Thus, the measured WAL features can be considered as consequence of SML of the TCI TSS, but the bulk bands have strong influence on the WAL due to coupling to TSS transport channels.

[58] Akiyama et al. *Nano Res.*, 9 (2):pp. 490–498, 2016
[59] Assaf et al. *Appl. Phys. Lett.*, 105(102108), 2014
[60] Shen et al. *Nano Lett.*, 15(6): pp. 3827–3832, 2015
[61] Bergmann. *Phys. Rep.*, 107 (1), 1984

Part II

Superconducting Devices and Unconventional Superconductivity

Motivation

Soon after the prediction and discovery of the first topological insulators, initial suggestions were made about the possibility of an unconventional type of superconductivity hosted at the interface between TI and conventional superconductors[62,63]. Since then, considerable theoretical and experimental effort has been dedicated to the study of this exotic phase of matter.

A topic still debated to this day in solid state physics research concerns a special kind of non-trivial superconductivity - the *FFLO phase of superconductivity*. This state is predicted to host unconventional types of Cooper pairs possessing finite momentum due to unconventional order parameters and exchange couplings. These peculiar states open the gates to superconductivity, which keeps their superconducting properties even beyond their critical magnetic fields[64]. As promising platforms for the search for finite momentum Cooper pairing, topological materials, proximity coupled to nearby superconductors are proposed[65].

In terms of technological purposes, unconventional superconductivity in topological insulators is of major interest because it hosts a very specific excitation - *zero-energy Majorana bound states* (MBS) - which naturally occur in topological superconductors as edge states in one dimension[66] or bound to vortices in two and three dimensions[67] (which are indeed similar to Abrikosov vortices).

[62] Fu and Kane. *Phys. Rev. Lett.*, 100(096407), 2008
[63] Linder et al. *Phys. Rev. Lett.*, 104(067001):1–4, 2010

[64] Radovan et al. *Nature*, 425: 51–55, 2003

[65] Park et al. *Phys Rev B*, 96: 064518, 2017

[66] Mourik et al. *Science*, 336 (6084):1003–1007, 2012
[67] Xu et al. *Phys. Rev. Lett.*, 114 (1):017001, 2015b

These bound excitations can be externally manipulated, fused and obey non-Abelian statistics, altogether providing a profound basis for the intriguing proposals of topological quantum computing[68]. Consequently, the experimental hunt for these peculiar quasiparticles had begun[69].

Since then dozens of smoking gun experiments have been conducted, but the most striking results were delivered by current-phase related measurements of *Josephson junctions*[70] and *superconducting quantum interference devices*[71]. In the following parts, the thesis aims to connect to these experiments and participate in the investigation of unconventional superconductivity and Majorana fermions.

[68] Das-Sarma et al. *npj Quantum Inf.*, 1(15001), 2015

[69] Wilczek. *Nat. Phys.*, 5:614–618, 2009

[70] Kurter et al. *Nat. Commun.*, 6(7130):1–6, 2015

[71] Maier et al. *Phys. Scr.*, T164 (014002):5–8, 2015

Introduction to Conventional and Unconventional Superconductivity

This section provides a phenomonogical overview of conventional superconductor pairing mechanisms and introduces the superconducting order parameter. Following, unconventional superconductor pairing possibilities and their significance for Majorana fermions are emphasized. This chapter condorms to the review articles of Lindner & Robinson[72] and Sigrist & Ueda[73], which are highly recommended for deeper understanding, and the textbook of Tinkham[74].

[72] Lindner and Robinson. *Nat. Phys.*, 11:307–315, 2015

[73] Sigrist and Ueda. *Rev. Mod. Phys.*, 63:239–308, 1991

[74] M. Tinkham. *Introduction to Superconductivity*. Number 978-0-486-43503-9. Dover Publications, second edition, 2004

Phenomenology of Conventional Superconductivity and Superconductor Pairing

In the 1950's Bardeen, Cooper & Schrieffer[75] and Ginzburg & Landau[76] (abbreviated in the following as *BCS* and *GL*, respectively) formed their theories of superconductivity. Even in modern superconductor research the combination of both suffice to describe superconductivity in conventional and high-temperature superconductors by only requiring the following (well measurable) system quantities:

[75] Bardeen, Cooper, and Schrieffer. *Phys. Rev.*, 108: 1175–1204, 1957

[76] Ginzburg and Landau. *Zh. Teor. Fiz.*, 20: 1064–1082, 1950. [english translation]

1. *critical temperature* T_c

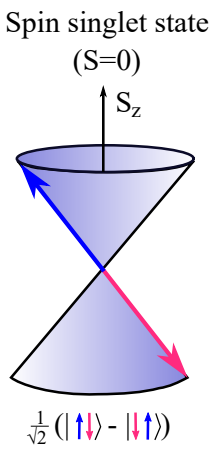

Figure 16: A sketch illustrating the spin singlet pairing state in superconducting BCS theory. The Cooper pairs consist of electrons carrying opposite momentum and spin constituting a "spinless" quasiparticle state.

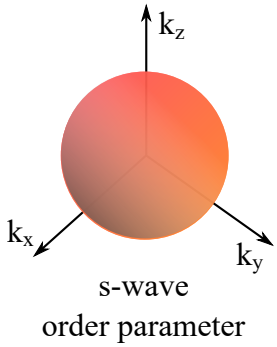

Figure 17: Isotropic order parameter of conventional superconductivity. Due to its spherical geometry it is referred to as s-wave pairing.

2. *crystal anisotropy*

3. *density of states (DoS)*

In both theories there is no doubt that superconductivity is carried by *Cooper pairs* (CP) with zero momentum. This stems from the countless amounts of experimental evidence given i.e. the Josephson frequency $2eV/h$, the magnetic flux quantum being the size $h/2e$ and the Knight shift dropping smoothly to zero for $T \mapsto 0\,K$, which implies trivial Cooper pairing of the spin-singlet $1/\sqrt{2}(|\uparrow\downarrow> - |\downarrow\uparrow>)$ type (as indicated in *figure 16*). An elegant way of obtaining a better understanding of the spin-singlet state is taking a closer look at the *superconducting order parameter* $\triangle$, which can be treated as a *complex scalar* as in GL theory

$$\triangle(k) = \triangle_0\, e^{i\varphi(k)}. \tag{6}$$

Here, $\varphi(k)$ is the superconducting phase factor, which is related to the supercurrent flowing through the material below T_c. An additional fundamental property of the order parameter is that it is $\triangle(k) \neq 0$ ($\triangle(k) = 0$) in the superconducting (conducting) state. At this point it should be noted that equation 6 is based on the assumption that pairing does take place only in an isotropic state, which means the CP exhibit zero center-of-mass momentum. This uniform superconducting order parameter is spherically geometric in momentum space - as illustrated in *figure 17* - and due to its geometry it is generally referred to as *s-wave superconductivity*, implying spin-singlet pairing as energetically favorable pairing opportunity.

But when combining superconductivity with magnetism, strong spin-orbit coupling or topological matter, these theoretical frameworks do reach their limit and pairing mechanisms occur that

can not simply be described thorugh conventional s-wave pairing. These cases are called *unconventional superconductivity* (or unconventional pairing) and will be discussed in the following section.

Unconventional Pairing: d-Wave and p-Wave Superconductivity

The term *unconventional* is used in regard to superconductor pairing, when the coupling of the CP is not necessarily given by the crystal lattice as it is described in the BCS framework. For all alloys consisting of heavier elements this is a considerable problem, due to the strong Coulomb repulsion being the magnitude of the phonon-mediated attractive interaction. To avoid large overlaps of the electronic wavefunctions, these systems tend "choose" ansiotropic channels, such as *d-wave* and *p-wave superconductivity*[77]. The name d-wave and p-wave are chosen analog to s-wave superconductivity due to their superconducting order parameter, which is no longer isotropic in momentum space. An illustration of the order parameters is provided in *figure 18*. *Figure 18(b)* in particular is of high interest for technological applications as it allows spin-triplet state pairing (demonstrated in *figure 19*) and therefore opens an avenue for spin-polarized supercurrents[78]. In an unbiased gedankenexperiment consisting of a hybrid device of *S-TI-S*, the spin-polarized supercurrents are proposed to be naturally present due to the TSS of the TI. This platform is predicted to host p-wave superconductivity and, as calculations by Fu & Kane[79] indicate, Majorana fermions. Yet incontrovertible experimental proof for MBS is still lacking, due to the high experimental challenge to detect them. In their prediction, Fu & Kane suggested the use of *Josephson interferometry*. But to be able to observe the predicted change in the *current-phase relation* one has to verify that

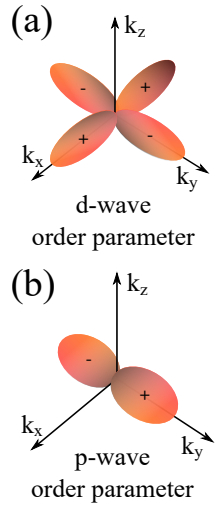

Figure 18: Illustation of unconventional superconducting order parameters. Due to their orbital geometry they are referred to as (a) d-wave and (b) p-wave superconductivity.

[77] Sigrist and Ueda. *Rev. Mod. Phys.*, 63:239–308, 1991

[78] Lindner and Robinson. *Nat. Phys.*, 11:307–315, 2015

[79] Fu and Kane. *Phys. Rev. Lett.*, 100(096407), 2008

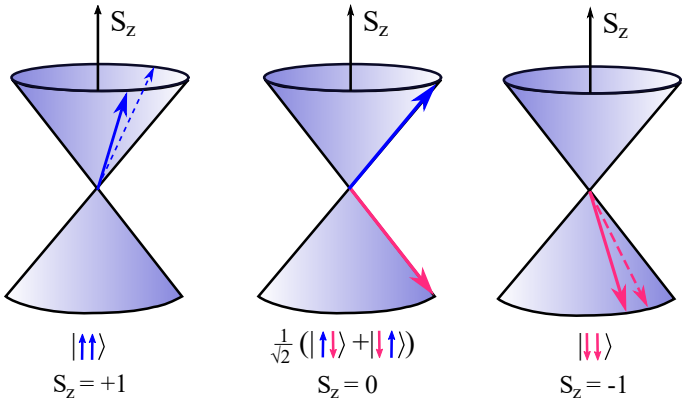

Figure 19: Illustration of spin triplet Cooper pairing in unconventional superconductors. This mechanism causes spin-polarized supercurrents. Superconducting TIs are a predestinated to host spin triplet pairing due to their TSS.

the chemical potential μ of the system lies directly in the center of the TIs Dirac cone, because only there the Majorana condition (a given particle is its own anti-particle)

$$\Gamma_k(E) = \Gamma^{\dagger}_{-k}(E) \tag{7}$$

is naturally satisfied due to the particle-hole symmetry of the superconducting state, as visualized in *figure 20*. Note that Γ ($\Gamma^{\dagger}$) represents the annihilation (creation) operator. Any offset between μ and the Dirac point would open access to "common" bulk channels, forming a trivial Andreev reservoir to be scattered in and hence loosing the information of gapless MBS[80]. Therefore, electrical gating to tune μ in real devices is essential. However, recent scientific progress led to propositions to find MBS in another type of superconductivity - the *FFLO phase*, which is introduced in the following section.

[80] Bocquillon et al. *Nat. Nanotechnol.*, 12:137–143, 2017

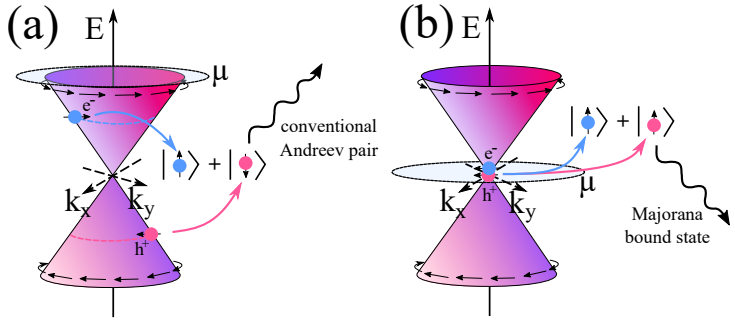

Figure 20: Illustration of the fulfilled Majorana condition in superconducting TI devices. In (a) the chemical potential μ is lying in the conduction band causing mainly conventional pairing. In (b) μ is tuned into the Dirac point and pairing of Majorana fermions is dominant.

Non-trivial Superconductivity: The FFLO Phase

Unconventional superconductivity with non-trivial (used in terms of magnetic exchange induced CP coupling) Cooper pairing states has been the subject of great interest in theoretical and experimental physics. A new state of superconductivity was predicted in the 1960's by Fulde & Ferrell[81], and Larkin & Ovchinnikov[82] (FFLO). In the FFLO state the superconducting order parameter has the unusual property of being modulated in *real space* rather as in momentum space, as it is for other order parameters (compare equation 6). To better investigate these peculiar superconducting phases the exploitation of materials with strong structural inversion asymmetry (SIA) and SOC coupled to nearby superconductors has been proposed[83,84]. This is predicted to stabilize the otherwise fragile superconducting FFLO state[85]. The SIA and SOC lifts the degeneracy in the fermi surfaces due to *Rashba spin-splitting* (RSS) and introduces an intrinsic anisotropy to the surface, making it more amenable to retaining a finite momentum phase[86,87] (illustrated in *figure 21(a) - (b)*). In particular, TIs and TCIs are listed as promising platforms for non-trivial superconductivity with finite momentum pairing, due to their TSS hosting massless and spin-momentum locked Dirac fermions[88].

[81] Fulde and Ferrell. *Phys. Rev.*, 135:A550–A564, 1964
[82] Larkin and Ovchinnikov. *Sov. Phys. JETP*, 20:762–769, 1965

[83] Loder et al. *J. Phys.: Condens. Matter*, 25:362201, 2013
[84] Zhang and Yi. *Nat. Commun.*, 4:2711, 2013
[85] Qu et al. *Nat. Commun.*, 4: 2710, 2013

[86] Dimitrova and Feigel'man. *Phys. Rev. B*, 76:014522, 2007
[87] Yoshida et al. *Phys. Rev. B*, 86:134514, 2012

[88] Park et al. *Phys Rev B*, 96: 064518, 2017

To understand the advantage of TIs for testing FFLO phases, it is recommended to revisit our gedankenexperiment defined in the previous subsection about unconventional superconductivity in the *S-TI-S* junction. The two-dimensional spin-momentum locked Dirac Hamiltonian of a TI (and TCI) surface can be expressed as

$$\mathcal{H}_{Dirac} = -\hbar v_F k_x \sigma_y + \hbar v_F k_y \sigma_x, \tag{8}$$

with v_F the fermi velocity, k_i the momentum components and σ_j the Pauli matrices. One can now consider an in-plane magnetic field $B = \big(0,\, B_y,\, 0\big)$ to induce the necessary magnetic exchange coupling in the system. Due to the acting *in-plane Zeeman field*, the Hamiltonian has to be modified to

$$\mathcal{H}_{Dirac} = -\hbar v_F \left(k_x - \frac{g\mu_B B_y}{\hbar v_F} \right) \sigma_y + \hbar v_F k_y \sigma_x, \tag{9}$$

where g is the *gyromagnetic factor* and μ_B is the *Bohr magneton*. A closer look at this Hamiltonian reveals that the location of the Dirac node has shifted away from the Γ-point (*L*-point) of the TI (TCI). The shift occurs along the x-direction by $\frac{g\mu_B B_y}{\hbar v_F}$ and results in a shift of the Fermi surface, which is depicted in *figure 21(c)*. As a result of this, the CPs gain a finite *center-of-mass momentum* (COMM) $q = 2\,\frac{g\mu_B B_y}{\hbar v_F}$. Consequently, one finds that the superconducting order parameter also has a phase modulation in x-direction. The FFLO order parameter is therefore given by

$$\triangle_{FFLO}(x) = \triangle_0\, e^{iqx} = \triangle_0\, e^{i\frac{2g\mu_B B_y}{\hbar v_F} x}, \tag{10}$$

with $q\,x$ being the phase modulation acquired from the finite momentum shift. Note at this point, that for COMMs aquired by TSS are strongly dependent on the choice of magnetic field direction $B_{x,y}$ according to the x, y-direction of the bias current. This is due

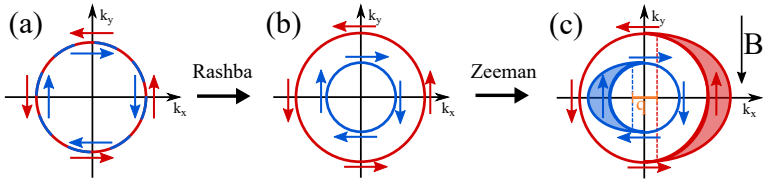

Figure 21: (a) shows the spin-degenerated fermi contour in absence of SOC. RSS lifts the spin degeneracy (b). In-plane magnetic fields B induce Zeeman splitting, leading to a finite COMM q and hence FFLO pairing (c).

to the SML giving rise to a fixed spin-orbit field. In-plane magnetic field response independent of the choice of B_x, B_y would be attributable to bulk RSS. Recent research, investigating Josephson junctions consisting of proximity coupled HgTe quantum wells (2D TI) in the electron-doped regime[89] and of strained Bi_2Se_3 (3D TI) flakes[90], was able to obtain first experimental evidence of spatially modulated non-uniform order parameters and FFLO phases in topological material. But despite all the intensive search, FFLO superconductivity still remains a heavily debated subject and further experimental work is highly desired.

[89] Hart et al. *Nat. Phys.*, 13:87–93, 2017

[90] Chen et al. *arXiv preprint*, arXiv:1801.08504v1:1–22, 2018

Basics of Superconducting Devices: Platforms to Investigate Unconventional Superconductivity

This chapter will provide an introduction to the fundamental principles of physical devices based on (induced) superconductivity. The introductional part is mainly based on the excellent textbook of Tinkham[91]. In recent years, Josephson interferometry has proven itself as one of the most powerful cornerstones in the search for unconventional superconductivity and zero-energy MBS. It is therefore necessary to briefly discuss the basics. Additionally, effects of technical nature (finite size effects, kinetic inductance etc.) and the way they modify measured signals will explained. At each point, the expected influence of topology and unconventional superconductivity will be highlighted to give the reader a better understanding of the pursued effects' relevance for later measurements.

[91] M. Tinkham. *Introduction to Superconductivity*. Number 978-0-486-43503-9. Dover Publications, second edition, 2004

DC and AC Josephson Effect

Half a century ago, B. D. Josephson[92,93] made the theoretical prediction that a zero voltage supercurrent

[92] Josephson. *Phys. Lett.*, 1: 251–253, 1962
[93] Josephson. *Adv. Phys.*, 14 (56):419–451, 1965

$$I_s = I_c \sin(\gamma) \tag{11}$$

should flow between two superconducting electrodes ("*banks*") seperated by a thin insulating barrier, where γ is the *gauge-invariant phase difference* and the *critical current* I_c is the maximum supercurrent a junction can support until superconductivity breaks down. This effect is referred to as *DC Josephson effect*. He further predicted that if a voltage drop V is maintained over a junction, the phase difference γ would evolve as follows:

$$\frac{d\gamma}{dt} = \frac{2eV}{\hbar}. \tag{12}$$

The result would be an *alternating current* of amplitude I_c and frequency $\nu = 2eV/h$, which is why this effect is referred to as *AC Josephson effect*. The quantum energy $h\nu$ is the change in energy of a given Cooper pair moving across the junction. DC and AC Josephson effects have been tested and confirmed by sheer countless experiments and form cornerstones of todays superconducting technologies.

Weak Links

Although Josephson predictions back in 1962 were based on microscopic theoretic model of quantum tunneling between two superconductors seperated by a thin insulating oxide layer, it is now clear that the effects are of a more universal nature and occur whenever two strongly superconducting leads are seperated by a *weak link*. As illustrated in *figure 22*, a weak link can be an insulating thin film, as Josephson originally proposed, a normal metal made weakly superconductive through proximity, or simply a short and narrow constriction in an otherwise entirely supercon-

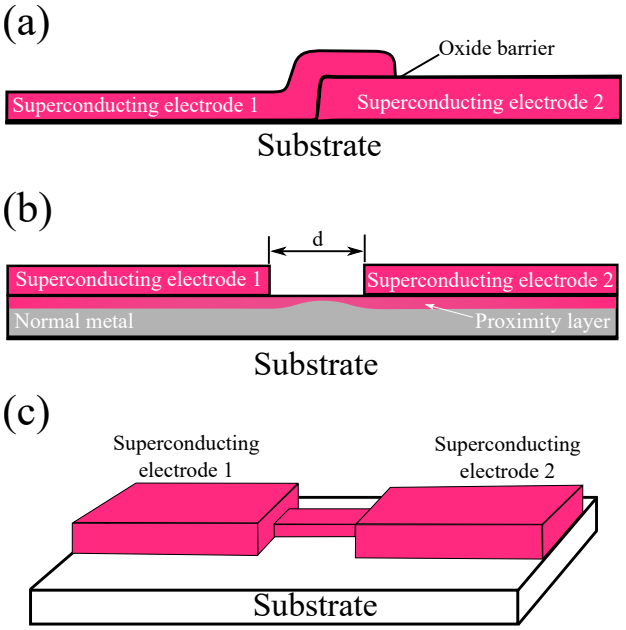

Figure 22: Three possible types of a weak link: (a) *S-I-S*, (b) *S-N-S* and (c) *S-c-S*. Designs (a) and (c) are used in patterned single crystal bulk samples, whereas all weak links of thin film samples are of type (b).

ducting material. These three typcial cases are often referred to as *S-I-S*, *S-N-S* and *S-c-S* junctions, where the *S*, *I*, *N* and *c* denote superconductor, insulator, normal metal and constriction, respectively. In this thesis, devices consisting of all types will be investigated. All thin film devices consist of *S-N-S* weak links and the focused ion beam structured bulk samples are formed out of *S-c-S* and *S-I-S* junctions.

Resistively and Capacatively Shunted Junction Model and the Tilted Washboard Potential

Although equation 11 and $I_c(T)$ suffice to fully characterize the zero voltage DC properties of a given weak link, for the finite voltage states a more detailed picture is necessary. Usually, this is provided by the RCSJ (*resistively and capacitively shunted junction*) model. In this context, the ideal Josephson junction (JJ) is

described as being shunted with a resistance R and a capacitance C, as sketched in *figure 23(a)*. The resistance R induces dissipation in the finite voltage regime by simultaneously leaving the lossless DC regime unaffected. An appropriate estimation of R is of the magnitude R_n (the normal state resistance) of the weak link near the transition temperature T_c. The capacitance C mirrors the geometric shunting capacitance between both banks. With these two additional parameters, the time dependence of γ in presence of a driving bias current can be derived by equating the bias current I_{sd} to the total junction current formed by the three parallel channels:

$$I_{sd} = I_{c,0}\, sin\,(\gamma) + V/R + C\, dV/dt. \tag{13}$$

It should be pointed out that the notation $I_{c,0}$ has been introduced in the above equation, which is for the purpose of clarity, as in later experiments I_c denotes the observable critical current (and can be less than $I_{c,0}$). By eliminating V in favor of γ, one obtains a second-order differential equation

$$\frac{d^2\gamma}{d\tau^2} + Q^{-1}\frac{d\gamma}{d\tau} + sin\,(\gamma) = \frac{I_{sd}}{I_{c,0}}, \tag{14}$$

where a dimensionless time variable $\tau = \omega_p t$ has been introduced, with

$$\omega_p = \sqrt{2eI_{c,0}/\hbar C} \tag{15}$$

being the *plasma frequency* of the weak link and Q being the quality factor defined as

$$Q = \omega_p RC. \tag{16}$$

It should be emphasized that Q^2 is identical to β_c, being the frequently used *Stewart-McCumber damping parameter*[94,95]. The differential equation 14 is in many cases able to describe the junction dynamics on a qualitatively sufficient level. Its solutions form the

[94] Stewart. *Appl. Phys. Lett.*, 12 (277), 1968
[95] McCumber. *J. Appl. Phys.*, 39(3113), 1968

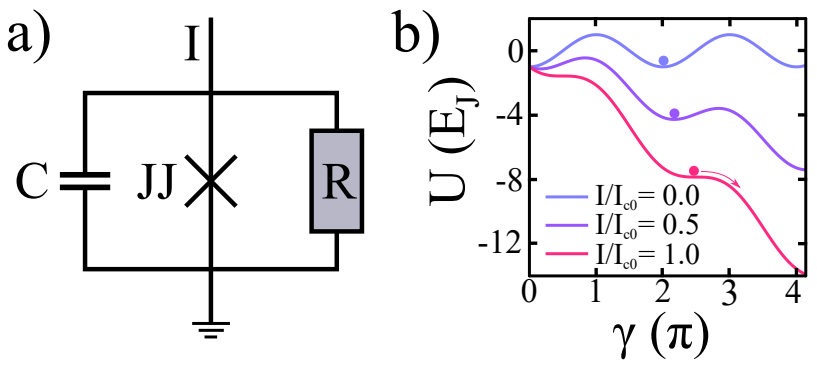

Figure 23: a) Equivalent circuit diagram illustrating the resistively and capacitively shunted junction (RCSJ). This application to a Josephson junction allows to describe the system in the resistive regime. b) illustrates the *tilted washboard potential* U of a Josephson junction for different bias currents I.

tilted washboard potential. It offers a mechanical analog owing to the fact that the equation of motion 14 is the same as for a particle of mass $(\hbar/2e)^2 C$ moving along the γ axis in an effective potential of

$$U(\gamma) = -E_J \cos(\gamma) - \left(\frac{\hbar I}{2e}\right)\gamma, \tag{17}$$

which is illustrated in *figure 23(b)*. The "particle" is subjected to a drag force $(\hbar/2e)^2 (1/R)\, d\gamma/dt \sim I_{sd}$ and the characteristic energy scale of the potential landscape in equation 17 is the Josephson coupling energy $E_J = (\hbar/2e)\, I_{c,0}$. The energy of the particle as it moves along its trajectory mirrors its total energy. In this picture the height of the trajectory above the cosine curve directly represents its kinetic energy. In absence of other energy sinks (as damping) such a trajectory is a horizontal, but coupling to e.g. a thermal heat bath randomly shifts the particle's energy up and down by a magnitude of $k_B T$ and is dependent on the time scale of RC. As will be discussed in the section *Superconducting Hysteresis - Thermal Escape & Retrapping*, these fluctuations cause $I_c < I_{c,0}$.

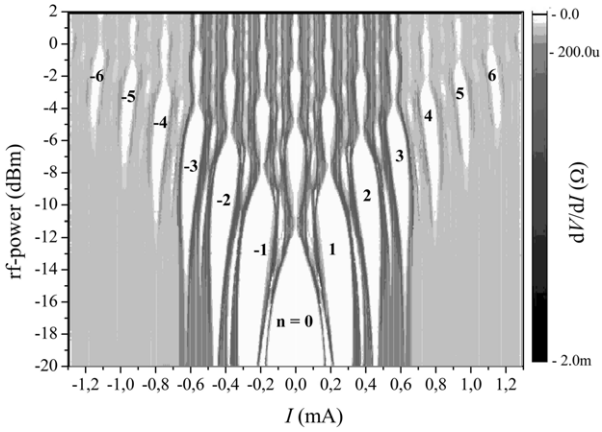

Figure 24: Grey-scale plot illustrating Shapiro measurements at S-N-S dependent on the bias current I and microwave power at fixed frequency. The regions with $dV/dI = 0\Omega$ represent the Shapiro steps. Illustration taken with courtesy from Kieler et al..

rf-Driven Josephson Junctions - Shapiro Steps

The irradiation of a JJ with microwave radiation of angular frequency ω_l causes the supercurrent to respond with constant voltage *shapiro steps* in the I-V (or *shapiro spikes* in the I - dV/dI) curves at voltages

$$V_n = n\frac{\hbar\omega_l}{2e}, \tag{18}$$

with $n = 0, \pm1, \pm2, ...$ If we consider DC voltage experiments at *S-N-S* weak links, which are exposed to finite microwave irradiation, this means that the device also possesses a characteristic voltage $V_c = I_c R_n$, where R_n is the normal state resistance, and therefore a characteristic frequency $f_c = 2eI_cR_n/h$. The evolution of the Shapiro response with respect to the rf power and bias current is in this way completely determined by the given characteristics. In *figure 24* an exemplary measurement of Kieler et al.[96] is shown as an illustration of later measurements. The Shapiro map is measured at an $Nb - HfTi - Nb$ *S-N-S* JJ array at fixed microwave frequency $f = 5\,GHz$. For superconducting devices consisting of topological matter, rf-driven investigations have recently been demonstrated as a powerful tool. This is mostly due

[96] Kieler et al. *Supercond. Sci. Technol.*, 20:318–322, 2007

to the far smaller interaction time scale in the microwave driven analysis compared to electrical DC investigations. This results in a higher propability of maintaining information about contributing MBS. These states are predicted to enter Shaprio measurements as a missing $n = \pm 1$ step (also referred to as *fractional AC Josephson effect*). First evidence was found in 2D TIs[97], 3D TIs[98] and Dirac materials[99].

[97] Bocquillon et al. *Nat. Nanotechnol.*, 12:137–143, 2017
[98] Wiedenmann et al. *Nat. Commun.*, 7(10303), 2016
[99] Li et al. *arXiv preprint*, arXiv:1707.03154v1, 2017

Magnetic Field Dependence of Josephson Junctions

Some of the most important investigations conducted in this thesis are based on the magnetic field response of a JJ. Introducing a magnetic field requires the rewriting of equation 11, which neglects the area of the weak link itself. *Figure 25* portrays the layout and device dimensions of a *S-N-S* weak link. The two superconducting leads A, B with width W are seperated by length L and the magnetic field is applied in z-direction, whereas the current I flows in x-direction. To calculate I_c the critical current density J_c has to be integrated over the junction area

$$I_c = \int \int dxdy\, J_c(x,y)\, sin\left(\gamma(x,y)\right). \tag{19}$$

To solve this equation one has to add the magnetic field influenced phase shift $\gamma_B(x,y)$ to the superconducting phase in the form $\gamma(x,y) = \gamma + \gamma_B(x,y)$. Using the approximation that the *London penetration length* λ_L is smaller than the thickness of the superconducting leads, the phase difference can be directly calculated by the enclosed flux. The complete flux within the JJ is given by $\Phi = AB$, with the effective area $A_{eff} = W(L + 2\lambda)$. This expression does not only include the device geometry, but also the additional size gained from finite London penetration[100]. If

[100] Maier et al. *Phys. Scr.*, T164 (014002):5–8, 2015

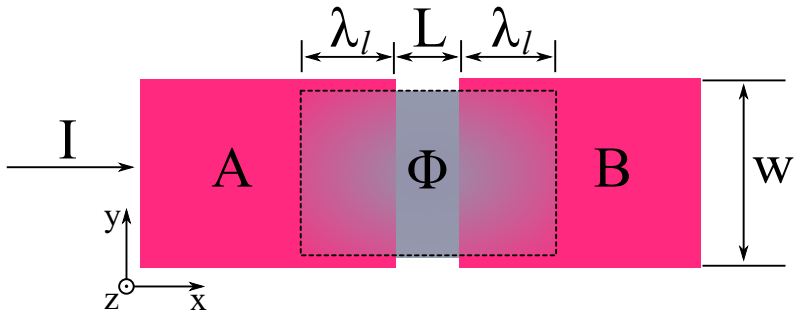

Figure 25: Illustration of a S-N-S Josephson junction geometry consisting of two superconducting leads A and B penetrated by the magnetic flux Φ within the effective junction area.

there are two electrical paths along the x-direction seperated by Δy, then only a part $\Delta\Phi$ of the total flux is embedded, leading to a phase shift

$$\gamma_B(\Delta y) = \frac{\Delta y}{W} 2\pi \frac{\Phi}{\Phi_0}, \tag{20}$$

with $\Phi_0 = h/2e$. Considering a homogenous current density $J_c(x,y) = J_c$ over the entire JJ, equation 19 can be solved. The resulting distribution of the maximum critical current is given by

$$\frac{I_c(\Phi)}{I_c(0)} = \left|\frac{sin(\pi\Phi/\Phi_0)}{\pi\Phi/\Phi_0}\right|. \tag{21}$$

Based on the similarity to light passing through a single narrow slit, this intensity distribution is referred to as *Fraunhofer diffraction pattern* and is visualized in *figure 26(a).* It can be observed that the critical current is at its maximum when the flux $\Phi/\Phi_0 = 0$ and thus the z-component of the magnetic field $B_z = 0\,T$. This property will be used in later measurements to gauge the maximum critical current of the devices, even without being able to detect the zero field value due to hysteretic behavior of the superconducting magnetic coils. Involving this technique, one can not rule out small field contributions in the xy-plane as the JJ is only set sensitive to the z-component of the magnetic field. Still, the influence is considered sufficiently small to be negligible.

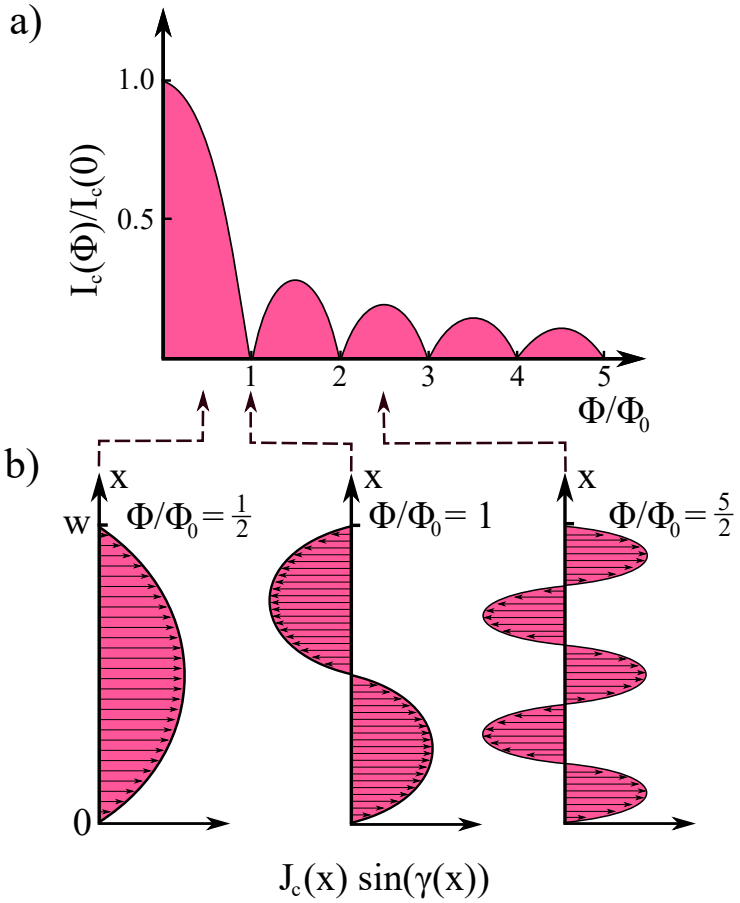

Figure 26: a) Illustration of the Fraunhofer pattern expected for a Josephson junction in dependence of the penetrating flux Φ. b) Spatial current distribution in the Josephson junction for $\Phi/\Phi_0 = \frac{1}{2}$, 1 and $\frac{5}{2}$.

To get a better feeling of the current paths in a JJ with applied magnetic flux, it is rather helpful to consider the *spatial current distribution* $J_c(x)\,sin(\gamma(x))$. In the case of half a flux quantum crossing through the junction, the phase shift caused by the magnetic field lies between 0 and π in the range from $x = 0$ and $x = w$ (illustrated in *figure 26(b)*). This results in a positive, but reduced current compared to the flux-free state. Every time the flux reaches $\Phi = n\Phi_0$, with integer $n = 1, 2, 3, ...$ the net critical current equals zero when equal amounts of spatial current are running in both directions. In between these regions the measured

total critical current is always positive, as shown for $\Phi = \frac{5}{2}\Phi_0$, but the reachable current maximum becomes smaller and smaller due to higher amounts of current running in the opposite direction. This visual concept will prove helpful for the interpretation of the measured Fraunhofer diffraction pattern. Topological weak links are expected to significantly influence the behavior of junction dynamics compared to trivial *S-N-S* junctions. Following the prediction by Fu & Kane[101], conventional Ss proximized to TSSs change the transport properties of the junction and allow new scenarios, which host MBSs. These quasiparticle modes have an unusual current-phase relation with a periodicity of 4π instead of 2π. This theoretical concept can be tested with Josephson interferometry and enters magnetic field dependent measurements by stretching/deforming the appearing Fraunhofer pattern according to the sine-function in equation11[102].

[101] Fu and Kane. *Phys. Rev. Lett.*, 100(096407), 2008

[102] Bocquillon et al. *Nat. Nanotechnol.*, 12:137–143, 2017

The Current-Phase Relation of a Josephson Junction

The *current-phase relation* (CPR) $I(\varphi)$ is one of the fundamental hallmarks of a JJ and describes the dependence of the measurable current I to the *absolute phase difference* φ over the weak link. Therefore, the Josephson equation 11 determines the CPR. As can be seen in the equation, for conventional junctions the CPR is supposed to show a sine-function behavior. To be accurate, this CPR holds specifically only for a *S-I-S* JJ. For the *S-N-S* weak links the CPRs have to be modified. It is therefore important to first distinguish between two distinct limits: *long junction* limit and *short junction* limit. A long junction (short junction) is given if $L \gg \xi_S$ ($L \ll \xi_S$), where L is the length of the weak link and $\xi_S = \frac{2\hbar v_F}{3k_B T}$ the *superconducting coherence length*. As in later measurements only long junctions are investigated, only CPRs within this limit are introduced in more detail. The CPR of a metallic weak link can in most cases be treated as a multichanneled, diffusive wire of the type[103]

$$I_{sd} \propto \sum \frac{(-1)^n}{(2n+1)(2n-1)} \sin(n\varphi), \tag{22}$$

where the phase can be written as $\varphi = 2\pi BA/\Phi_0$ as it is measured by external magnetic field dependence. This CPR is still sinusoidal, but allows slight deviations depending on the strength of the disorder. If one considers a weak link consisting of a TI hosting *ballistic* TSSs, the CPR is predicted to be *saw-tooth shaped*[104,105], thus

$$I_{sd} \propto \sum \frac{(-1)^n}{n} \sin(n\varphi)\, e^{-tn}, \tag{23}$$

where t is the *transmission parameter* of the ballistic channels with $0 \leq t \leq 1$. $t = 0$ means there is no ballistic transport contribution present in the weak link, whereas $t = 1$ characterizes the ideal ballistic transport regime. In *figure 27* the dependency of equa-

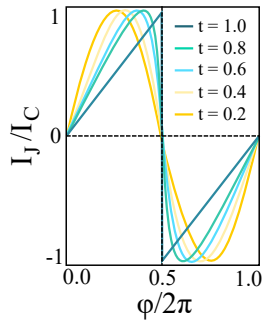

Figure 27: Simulated CPR showing the influence of ballistic transport. For weak links consisting of TIs ballistic sawtooth-shaped CPRs are predicted due to TSS. For $t \to 1$ the saw-tooth shaped CPR is obtained.

[103] Heikkilä et al. *Phys. Rev. B*, 66(184513), 2002

[104] Beenaker et al. *Phys. Rev. Lett.*, 110(017003), 2003

[105] Murani et al. *Nat. Commun.*, 8(15941), 2017

tion 23 is illustrated by simulating the ballistic CPR for several t. As closer $t \to 1$, the sharper defined appears the ideal sawtooth shape.

Modelling the Temperature Dependence of Josephson Currents

There exist a couple of techniques to model the T-dependency of the critical current of a weak link depending on whether type of JJ. In this thesis it suffice to take a closer look at the *S-N-S* junction. All hybrid devices containing superconductors can be described on basis of the *Gor'kov equations*[106]. In applications these junctions are often simplified by quasi-classical approximations. This can be justified as long as the fermi wavelength is much smaller than the device dimensions. In those cases frequently used approaches are the *Eilenberger quasi-classical equations*[107]. These equations treat the ballistic transport of the normal metal layer (and hence the transport in the *clean limit*). The in this thesis used TI weak links are supposed to hold the clean limit due to the TSS. The Eilenberger equation is given by

[106] Gor'kov. *Sov. Phys. JETP*, 7:505–508, 1958

[107] Eilenberger. *Z. Phys.*, 214: 195–213, 1968

$$I_c = a\frac{2}{\pi}ek_F^2\frac{k_BT}{h}\,sin\,(\gamma)\sum_{\omega_n}\int_0^1 \varsigma d\varsigma\,\frac{t^2}{Q^{1/2}\,(t,\gamma,\varsigma)}, \tag{24}$$

with $\varsigma = k_x/k_F$ and $t = D/(2-D)$ with D the transperancy of the S-TI interface and a the cross section of the junction and

$$Q = \left\{t^2 cos\,(\gamma) + \left[1 + \frac{\left(t^2+1\right)\omega_n^2}{\triangle^2}\right] cosh\left(\frac{2\omega_n L}{\mu\hbar v_F}\right) + \frac{2t\omega_n\Omega_n}{\triangle^2} sinh\left(\frac{2\omega_n L}{\mu\hbar v_F}\right)\right\}^2 - \frac{\left(1-t^2\right)^2\Omega_n^2}{\triangle^2}, \tag{25}$$

where $\omega_n = 2\pi k_BT\,(2n+1)$ is the *Matsubara frequency*, $\Omega_n = \sqrt{\omega_n^2 + \triangle^2}$ and $\triangle$ is the gap of the S electrodes. The integral runs over all trajectory directions and can be adjusted to actual junction geometries. If transport over the junction is not ballistic, but diffusive, the JJ is dominated by disorder. The transport is therefore given in the *dirty limit* by the *Usadel equation*[108]

[108] Usadel. *Phys Rev.Lett.*, 25: 507–509, 1970

$$\Upsilon_{S,N} = \triangle_{S,N} + \xi^2 \frac{\pi k_B T_c}{\omega_n G_{S,N}} \frac{d}{dx} \left(G^2_{S,N} \frac{d}{dx} \Upsilon_{S,N} \right), \tag{26}$$

where Υ is defined over the normal Green's function G and the anomalous Green's function F by $\Upsilon G = \omega_n F$. The normalization condition $FF^* + G^2 = 1$ then gives

$$G_{S,N} = \frac{\omega_n}{\sqrt{\omega_n^2 + \Upsilon_{S,N} \Upsilon^*_{S,N}}}. \tag{27}$$

The superconducting coherence length is given by $\xi = \sqrt{\frac{\hbar D}{2\pi k_B T}}$ with the diffusion constant $D = v_F L_\Phi / 3$. Often devices show temperature dependent critical current characteristics in the *intermediate regime*[109]. This is known for *S-N-S* weak links dominated by bulk shunted two-dimensional transport. These cases can be fitted with an *analytical model*[110]

$$I_c(T) \propto \sqrt{T}\, e^{-\frac{2\pi k_B T}{E_{th}}}, \tag{28}$$

where E_{th} is the *Thouless energy* of the system. Together, these three models has been found as key diagnostic of disentangling TSS contributions to superconductivity in the investigation of topological JJs[111].

[109] Galetti et al. *Phys. Rev. B*, 89(134512), 2014

[110] Kresin. *Phys. Rev. B*, 34 (7587), 1986

[111] Veldhorst et al. *Nat. Mater.*, 11:417–421, 2012

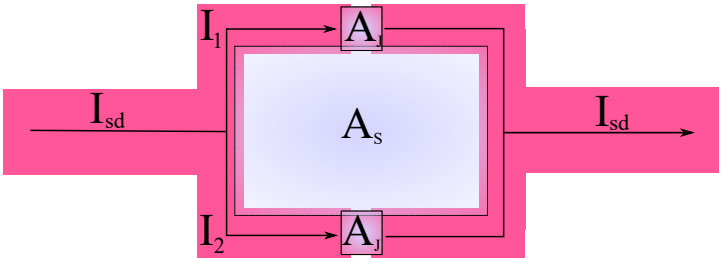

Figure 28: Schematical illustration of a DC SQUID with the area A_s driven by a bias current I_{sd} . I_{sd} seperates into I_1, I_2 each moving through each JJ with area A_J. The interference of both supercurrents in presence of a magnetic field causes the SQUID pattern.

DC SQUID - Two Josephson Junctions in a Parallel Circuit

A SQUID (*superconducting quantum interference device*) is a superconducting ring structure with at least one weak link. Technically, there are two main categories: RF SQUIDs and DC SQUIDs. RF SQUIDs are superconducting rings consisting only of one weak link and need to be inductively coupled to a rf-source. DC SQUIDs have two weak links, but can be used with just an applied DC bias. Both variants are commonly used devices to measure magnetization, as they provide ultra-high resolutions compared to other techiques like Hall sensors[112]. In this thesis only DC SQUIDs will be investigated. A known magnetic field is applied externally to the SQUIDs in order to manipulate the phase difference and study the resulting modulation of the critical current. Furthermore, different layouts, i.e. different s-wave Ss like *Nb*, *Ta* and symmetric as well as asymmetric SQUID geometries, are used to test the influence of the supercurrent carrying TSSs.

[112] Clarke et al. *SQUID Sensors: Fundamentals, Fabrication and Applications*, volume 329 of *Series E: Applied Sciences*. Kluwer Academic Publishers, 1996

Magnetic Field Dependence of Symmetric SQUIDs

The magnetic flux Φ_S inside the superconducting loop consists of two components. The first is the external applied magnetic field flux Φ_{ext}, which depends on the area of the ring structure A_s and the magnetic field applied perpendicular to the device B.

The second is the induced flux Φ_{ind} generated by the SQUID itself in order to fulfill the flux quantization in the given system. This means as long as the ring is in the superconducting state, the total flux will always be $\Phi_S = n\Phi_0$ with n being integer and Φ_0 the magnetic flux quantum. The induced flux is generated by an occuring shielding current J, which is related to the generated flux by the self inductance L of the SQUID. J can be positive or negative, depending on the induced flux being added or substracted. Pieced together, this means

$$\Phi_S = \Phi_{ext} + \Phi_{ind} = BA + LJ. \tag{29}$$

Due to flux quantization, J will generate the smallest necessary flux Φ_{ind} to round Φ_{ext} to the next integer part of Φ_0, which therefore means that the size of the self induced flux has to be $|\Phi_{ind}| \leq \Phi_0/2$. This can later be used to estimate the inductance of the system. This poses the question as to how much current is passed over each JJ, as they limit the possible total critical current of the SQUID (the sketch in *figure 28* gives a overview of the currents in the system). The biased source-drain current I_{sd} applied externally splits (for simplicity's sake here first equally) and runs through each JJ. As a result the currents through the JJs, while taking the ring current Ξ into account, are

$$I_1 = I_{sd}/2 + \Xi \ \wedge \ I_2 = I_{sd}/2 - \Xi. \tag{30}$$

In the previous chapter the phase dependent behavior of a JJ, neglecting its finite area, was given by equation 11, which in this case applies for both JJs individually, i.e. $I_n = I_{c,n} sin(\gamma)$, with $n = 1, 2$ referring to each of the two JJs. Intergrated over the entire loop, one is able to calculate the phase difference γ between both

superconducting regions seperated by the JJs to

$$\gamma = \gamma_2 - \gamma_1 = \frac{2\pi}{\Phi_0} \left(\Phi_{ext} + \Phi_{ind} \right). \tag{31}$$

Rewriting equation 30 and combining it with equation 31 as well as the CPR of each JJ, ones reaches the prominent formula for a symmetrical SQUID

$$I_{c,SQUID}^{sym} = 2I_c |cos\left(\pi \frac{\Phi_S}{\Phi_0} \right)| \tag{32}$$

under the simplifying assumption that both JJ can carry identical critical current $I_c = I_{c,1} = I_{c,2}$.

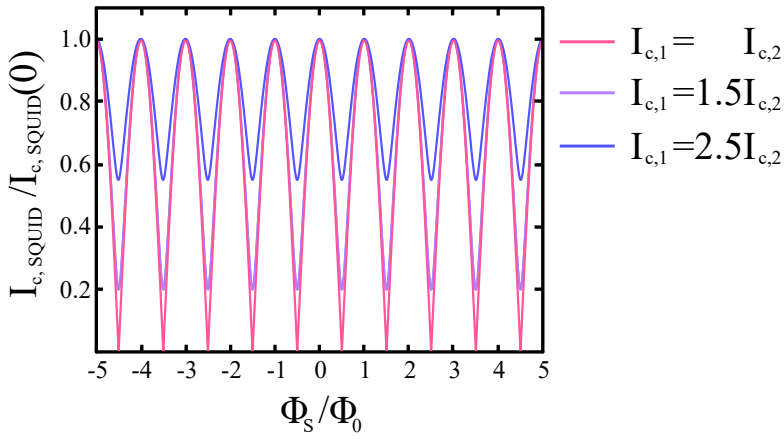

Figure 29: Numerical results for symmetrical ($I_{c,1} = I_{c,2}$) and asymmetrical ($I_{c,1} \neq I_{c,2}$) SQUIDs. In symmetrical SQUIDs the critical current oscillations are perfectly cancelled to $I_{c,SQUID} = 0$ for each $\Phi_S/\Phi_0 = \pm\frac{1}{2}, \frac{3}{2}, ...$ In the asymmetrical case, the critical current modulation shows an offset depending on the device asymmetry strength.

Asymmetric SQUIDs

Keeping Eq.32 more general, one can rewrite it for arbitrary values of $I_{c,n}$ to

$$I_{c,SQUID}^{asym} = \sqrt{(I_{c,1} - I_{c,2})^2 + 4 I_{c,1} I_{c,2}\, cos\left(\pi \frac{\Phi_S}{\Phi_0}\right)}. \qquad (33)$$

This more complex SQUID equation describes critical current modulation of asymmetrical SQUIDs, in which both weak links can carry different amounts of critical current and therefore result in different critical current modulation patterns. To get a better feeling how strong asymmetries in SQUID geometries enter the measurements, *figure 29* shows numerical simulations for the symmetrical ($I_{c,1} = I_{c,2}$) as well as asymmetrical case ($I_{c,1} \neq I_{c,2}$). The most prominent observation is that the minimum $I_c \neq 0$ in asymmetrical devices. The stronger the asymmetry, the higher the superconducting offset beneath the critical current oscillations. From a technical point of view, asymmetrical SQUIDs are compelling because they enable the investigation of the CPRs of single JJs with their accuracy[113,114]. For strong asymmetries $I_{c,1} \ll I_{c,2}$, the

[113] Murphy et al. *Phys. Rev. B*, 96(094507), 2017
[114] Nanda et al. *Nano Lett*, 17 (6):3396–3401, 2017

CPR of the weak link with lower critical current $I_{c,1}$ alone can be tested. Sufficiently large asymmetries can be created by SQUIDs consisting of e.g. one *S-N-S* and one *S-c-S* weak link, due to the commonly large critical currents of mirco-bridge devices[115].

[115] Murani et al. *Nat. Commun.*, 8(15941), 2017

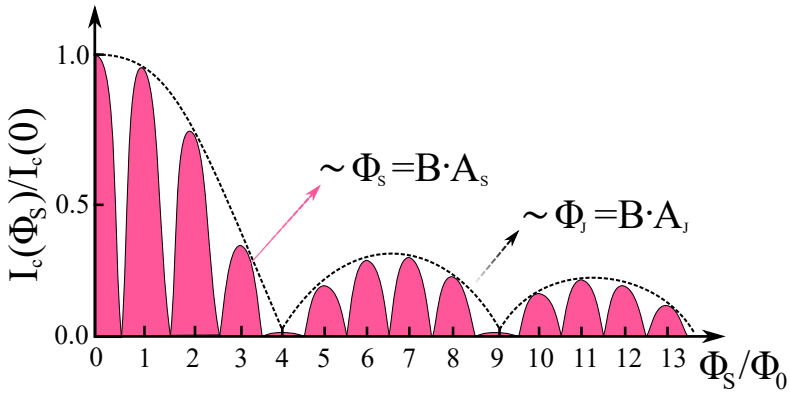

Figure 30: Illustration of the finite size influence on the SQUID pattern. Depending on the JJ sizes A_J with respect to the SQUID size A_S, the SQUID oscillations are modulated with the Fraunhofer pattern of the individual JJs.

Finite Size Effect in DC SQUID Patterns

However, the from equation 33 numerically calculated SQUID patterns of *figure 29* are inaccurate for most real devices. This can be attributed to neglecting the finite size of the weak links compared to the size of the SQUID itself. The real data is expected to have the form that was predicted for SQUID oscillations in equation 33, but are modulated by the generated Fraunhofer diffraction pattern, which is in turn determined by the size of the weak links given in equation 21. The illustration in *figure 30* visualizes what the measured I_c magnetic field response of a DC SQUID actually looks like. For most measurements in this thesis the size relations between SQUID and JJs are the way that only the first two nodes of the over-modulated Fraunhofer diffraction pattern can be witnessed before the superconducting leads are quenched.

Superconducting Hysteresis - Thermal Escape & Retrapping

In many applications the assumption $E_J \gg k_B T$ does not necessarily hold true and thermal escape from the tilted washboard potential is non-negligible. As expected, it results in "roundings" of measured I-V characteristics, which are depicted in *figure 31(a)*. But additionally, one can often measure superconducting hysteretical behavior of real devices in current-biased sweep (forth and back measured I-V curves) experiments (portrayed in *figure 31(b)*). This effect is contributed solely to thermal self-heating of the superconducting device itself[116]. This can be understood if one considers two distinct cases:

1. The current is biased from the superconducting into the resistive one: $I(0) \longmapsto I > I_c$. In the superconducting state the investigated device is defined by $R = 0\Omega$. Because there is no resistance, current induced Joule heating does not exist and the measurement gives the critical current I_c.

2. The current is biased from the resistive into the superconducting state: $I > I_c \longmapsto I(0)$. In the resistive state the investigated device is defined by the normal state resistance $R_n > 0\Omega$. Since there is resistive transport, current does induce Joule heating, which can result in some devices (dependent on material, dimensions, ...) in retrapping currents $I_R \ll I_c$.

For devices exhibiting giant thermal hysteretics, the Fraunhofer and SQUID pattern does consequently look strongly asymmetrical for positive bias currents I_{sd}^{+} and negative bias currents I_{sd}^{-} at fixed sweeping directions. In these cases only the magnetic field response in either I_{sd}^{+} or I_{sd}^{-} direction is measured and recorded.

[116] Skocpol et al. *J. Appl. Phys.*, 45(4045), 1974

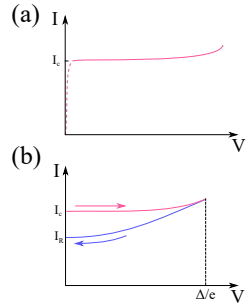

Figure 31: (a) Illustration of the influence of thermal escape in current-biased measurements. The curves appear thermally "smeared". (b) depicts a superconducting hysteresis loop of a device influenced by current induced self-heating.

Influence of (Kinetic) Inductance in DC SQUID Measurements

Due to the ring structure, and the therefore existing circulating currents, SQUIDs possess a *self inductance* (very similar to an electromagnetic coil) which dampens the critical current modulation. The dampening originates in most cases solely from the geometric design of the SQUIDs and can lead to multivalued switching currents[117] as well as reduced modulation depths (as in asymmetric SQUIDs)[118]. The *geometric inductance* L_G of a SQUID can be approximated by considering the inductance of a ring

$$L_G \approx N^2 R \mu_0 \mu_r \left\{ ln \left(\frac{8R}{a} - 2 \right) \right\}, \tag{34}$$

where the number of windings N is in case of a SQUID set to $N = 1$, R is the device radius and a is the width of the superconducting leads. The influence of L_G can be expressed by the geometric (inductive) screening factor

$$\beta_L = \frac{2 L_G I_{c,SQUID}}{\Phi_0}. \tag{35}$$

For values of $\beta_L < 1$ the shielding currents do not influence the SQUID behavior sufficiently to be noticeable, but if they result in values of $\beta_L \geq 1$, self-inductance can significantly alter ther magnetic field response. For all the devices investigated in later measurements screening factors in the range of $\beta_L \simeq 0.03 - 0.21 \ll 1$ are obtained and geometric inductance is therefore negligible. However, we will see that most of our devices are dominated by large *kinetic inductances* L_K of the weak links, associated with the kinetic energy of the superconducting condensate in the weak links[119]. Within certain limits, a large kinetic inductance can in-

[117] M. Tinkham. *Introduction to Superconductivity*. Number 978-0-486-43503-9. Dover Publications, second edition, 2004

[118] Faucher et al. *Physica C*, 368:211–217, 2002

[119] Meservey and Tedrow. *J. Appl. Phys.*, 40(2028), 1969

fluence the SQUID $I_c(B)$ curves in a manner comparable to the geometric inductance. For a *long* weak link the CPR is derived from the non-linear GL equation. For the CPR, one obtains

$$I = \frac{\Phi_0}{2\pi L_K}\left(\varphi - \frac{\xi_S^2}{l^2}\varphi^3\right), \tag{36}$$

with φ as phase across the junction. L_K is directly linked to the length l and the cross-section σ of the weak link through the expression

$$L_K = \mu_0 \lambda^2 \frac{l}{\sigma}. \tag{37}$$

This connection allows the introduction of, by analogy to the geometric screening factor β_L, the *kinetic screening factor*

$$\beta_K = \frac{2\pi L_K I_c}{\Phi_0}. \tag{38}$$

This parameter can than be used to rewrite eq. 36 to:

$$I = \frac{I_c}{\beta_K}\left(\varphi - \frac{\xi_S^2}{l^2}\varphi^3\right). \tag{39}$$

For all $\beta_K > 1$ the $I_c(B)$ dependence becomes *multivalued*[120]. Additionally, the phase φ spans only a limited range before switching to the neighboring state and leads to a linear (*triangular shaped*) CPR $I(\varphi)$ dependency. However, an impartial reader may wonder at this point why one should bother with kinetic inductance phenomena at all: the answer becomes apparent when we think about integrating a TI as a weak link. In the most unbiased picture a TI contributes to transport only via TSSs. As TSSs are *a priori* narrow in dimension and possess high carrier mobilites[121], entering charge carriers experience a change in electromotive force. This is countered by inertia, making the massive charge carrier take finite

[120] Likharev. *Rev. Mod. Phys.*, 51(101), 1979

[121] Wang et al. *Nat. Commun.*, 8(366), 2017

time to accelerate. This acceleration time manifests itself then as a "phase lag" in SQUID measurements. Guided by this mental image, SQUIDs consisting of TI weak links would be expected to possess high *intrinsic kinetic inductances*.

Integer and Half-Integer Flux Quantization

The previously mentioned integer flux quantization is among one of the most striking demonstrations of the macroscopic phase coherence of the charge carrier pair wavefunction in Ss. As already demonstrated by equation 6, Cooper pairs can be described by a single complex wavefunction, which includes the superconducting phase $\varphi(k)$. The *integer flux quantization* (IFQ) is a direct consequence of the single-valuedness of the pair function potential, or equivalently of the phase winding in multiples of 2π along a superconducting path. The superconducting loop is threaded by Φ and is hence quantized in Φ_0 by

$$\Phi = n\,\Phi_0,\ n = 0,\ 1,\ 2,\ ... \tag{40}$$

with $\Phi_0 = h/2e = 2.07 \times 10^{-15}\,Wb$. But there is a way to artificially incorporate a phase-shift of π in a superconducting loop (known as π-junction or π-transition). One established way of entering in such phases is through the use of Zeeman splitting fields, which can enable the spatial modulation of the superconducting pairing potential $\triangle(k)$ (as described in the section *Non-Trivial Superconductivity: The FFLO Phase*, equation 10). The magnetic flux states in a π-loop are governed by the following expression:

$$\Phi = \left(n + \frac{1}{2}\right)\Phi_0,\ n = 0,\ 1,\ 2,\ ....\tag{41}$$

The ground state $\Phi = \pm\Phi_0/2$ represents a pair of degenerated states, illustrated in *figure 32* through the free energy potential landscape of a π-loop and a 0-loop. The time-reversed partner states of a π–loop can be thought of as supercurrents flowing clockwise and counter-clockwise within the superconducting loop, respectively. This effect is called *half-integer flux quantization* (HIFQ).

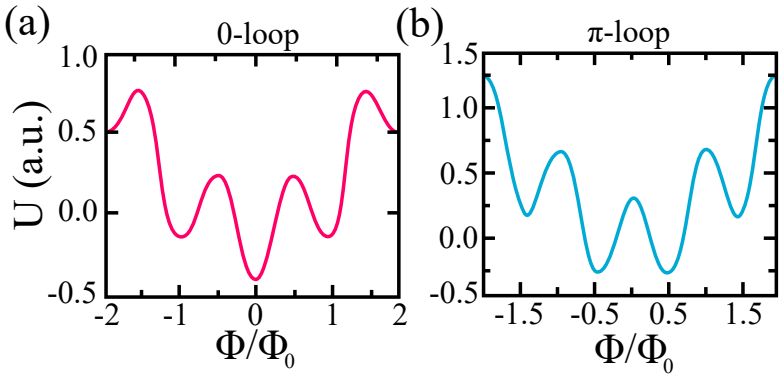

Figure 32: The free energy U landscape of a superconducting (a) 0-loop and (b) π-loop device. The ground state of the 0-loop is single-valued, whereas the π-loop ground state is degenerated at $\Phi/\Phi_0 = \pm 0.5$. Devices that can be systematically tuned between both states and allow $\varphi_0 \neq 0, \pi$ are labelled φ_0-*junctions*.

If such $0 - \pi$ transitions can be tuned periodically by controlling a system parameter, e.g. the assisting Zeeman field, such devices are called φ_0-*junctions* or φ_0-*SQUIDs* (where $\varphi_0 \neq 0, \pi$) . These systems are of high technological interest because of their potential applications in memory storage and quantum computing operations.

Magnetic Field Induced Topological Superconductivity in Planar Superconducting Devices

Recent theoretical findings by PIENTKA ET AL.[122], investigating superconducting transport of planar thin film JJs, have led to the prediction of topological superconductivity even in the absence of TSSs. In their calculations, they consider a 2DEG with strong uniform SOC contacted between two superconducting leads, which is subjected to in-plane magnetic Zeeman fields. The ABS energy spectrum of such a device is represented in *figure 33(a).* Without Zeeman fields, the spectrum as a function of the superconducting phase φ is degenerated twofold, which is illustrated by grey lines. Once a Zeeman field high enough to enable finite COMM of the carriers is present, the degeneracy is split and the lifted ABS form a topological phase for $\varphi_1 < \varphi < \varphi_2$, where φ_1, φ_2 mark the crossing of the ABS represented by blue and red lines, repectively. The resulting phase diagram is pictured in *figure 33(b)*. Strikingly, for a phase difference $\varphi = \pi$ the system is in a topological phase for arbitrary Zeeman fields and nearly independent of the choice of chemical potential. Accordingly, for a phase difference $\varphi = 0$ the system remains in a trivial superconducting state thoughout. It is further predicted that each trivial-to-topological phase transition (which is for $E_Z = E_{th}/2$) is accompanied by a minimum critical current I_c of the device and a $\Phi_0/2$ periodicity. As also pointed out, the system hosts Majorana fermions at all $\varphi = \pi$ phase differences, which are to a large extend independent of the choice of the chemical potential μ, the junction width W or induced pairing strength. This is interesting, as it stands in sharp contrast to other recent proposals, which require careful transport manipulation by electrical gating. Therefore, this technique enables a new

[122] Pientka et al. *Phys. Rev. X*, 7(021032), 2017

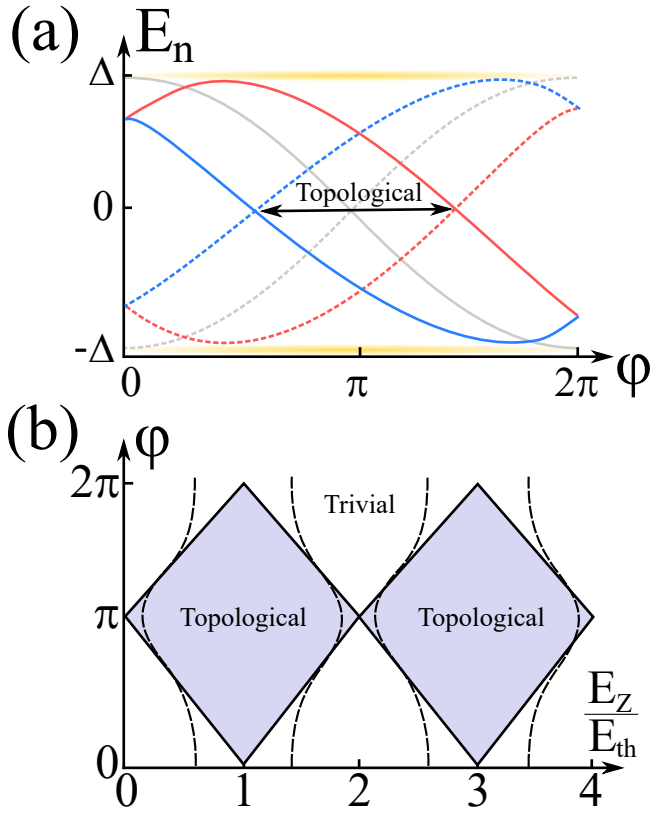

Figure 33: (a) The ABS spectrum of narrow junctions with strong SOC. The spectrum is, in absence of a Zeeman field, degenrated twofold (depicted as grey lines). Zeeman fields lift the degeneracy and split the states (indicated in red and blue), constituting a topological phase. (b) Illustrated superconducting topological phase diagram as a function of Zeeman field energy E_Z given in units of the Thouless energy E_{th} and phase difference φ. The dashed lines represent the effect of non-ideal superconductor-metal interface transparency $D < 1$.

methodology for the search of MBSs by not manipulating the superconducting phase of the system locally (e.g. by gating), but globally (through external in-plane magnetic fields).

Part III

Results of the Thin Film Devices

Thin Film Superconducting Devices

This part concerns itself with the experimental results obtained from the investigations of the superconducting devices consisting of TCI $SnTe$ thin films. Firstly the sample layout and the device fabriaction is presented. Concerning the transport analysis, first the development of the proximity-induced superconductivity is discussed. Following the devices' response to rf exposure, gating and magnetic fields is analyzed. The measurements are then reviewed in terms of unconventional pairing, induced by the spin-polarized TSS and high spin-orbit coupling of the TCI weak links.

Lithography, Fabrication and Sample Layout

The mesoscopic JJs and SQUIDs investigated within the following chapters are micropatterned through conventional e-beam lithography and physical dry etching techniques. The e-beam lithography is done in two steps, each with a negative resist. The e-beam resist is deposited on top of $SnTe/Nb$ and $SnTe/Ta$ film stacks. The superconducting films are deposited *in-situ* via DC sputtering at room temperature on top of the $30\,nm$ $SnTe$ films. The thickness of the superconducting materials is kept at $t_s = 30nm$. Transport measurements of bare $30\,nm$ thick Nb and Ta films show superconducting phase transitions at $T_c^{Nb} = 5.8\,K$ and $T_c^{Ta} = 2.8\,K$,

which is visualized in *figure 34*. Both T_c^{Nb} and T_c^{Ta} are below bulk literature values ($T_{c,lit}^{Nb,bulk} = 9.3\,K$ and $T_{c,lit}^{Ta,bulk} = 4.4\,K$)[123]. This is a common feature observed for DC/RF sputtered superconducting thin films and is attributed to interstitial impurities[124]. In light of this, the measured T_c are well within the upper limit of reported values for sputter deposited Ta/Nb thin films of comparable thickness[125,126]. However, for lithography the e-beam resist is spin-coated with $5000\,rpm$ (resulting in an estimated resist film thickness of $t_{resist} \approx 100\,nm$) and baked out on a hotplate at $T_{hp} = 85\,^{\circ}C$ for 2 minutes. The temperature of the hotplate is chosen sufficiently moderate, so that the upper temperature limit $T = 140^{\circ}C$, where *Te* is found to evaporate out of the *SnTe* films, is nowhere near reached and can be neglected. After irradiation the exposed resist is developed in an adjacent agent for 8 minutes and afterwards placed in an Ar^{+}-ion milling chamber equipped with a secondary ion mass spectrometer. The dry etch is monitored in the first run until no spectroscopic feedback of the Nb/Ta is observed and in the second step until only substrate feedback is found. After each etching, the remaining resist is lifted by a 45 minute bath in cup of acetone, which is in turn placed in an ultrasonic bath. The resulting structures appear as demonstrated in *figure 35*. The false-color SEM image shows devices similar to-Hall bar shapes (*figure 35(a)*). At each of the 10 side arms, a JJ or a (symmetric or asymmetric) SQUID is placed. This is shown in *figure 35(b)*, which is a close-up taken from the gray shaded area in *figure 35(a)*. This device concept enables the measuring of several JJs and SQUIDs with different dimensions during one cooldown period. All samples are measured in *"sionludi"* table-top dilution cryostates[127]. These cryostate systems are designed in the Néel Insitute and are able to reach minimum temper-

[123] Theuerer and Hauser. *J. Appl. Phys.*, 35:554–555, 1964

[124] Gerstenberg and Hall. *J. Electrochem. Soc.*, 111(8):936–942, 1964

[125] Kodama et al. *J. Appl. Phys.*, 54(7):4050–4053, 1983

[126] Liu et al. *IEEE Trans. Appl. Supercond.*, 19(3):245–248, 2009

[127] Donnier-Valentin and Wernsdorfer. *Research Highlights Institute Néel*, 6, 2012

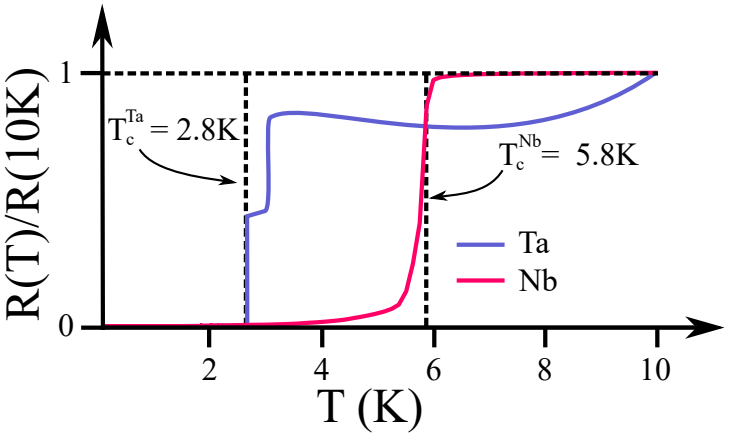

Figure 34: The temperature-dependent relative resistances $R(T)/R(10K)$ of $30\,nm$ Ta and Nb bare films. The measurements specify the critical temperatures of the sputtered samples. At $T_c^{Ta} = 2.8K$ and $T_c^{Nb} = 5.8K$ both values are lower than their bulk literature values.

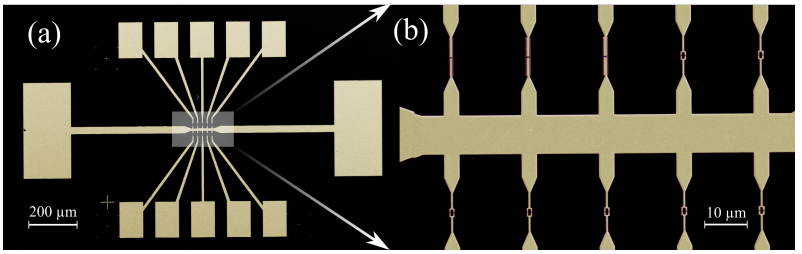

Figure 35: (a) false color SEM image illustrating the typical sample layout. (a) shows a Hall bar-type structure, each side arm contacts a single JJ or SQUID. This sample layout allows for several samples to cool down at once. (b) provides a close-up of the gray rectangluar area in image (a).

atures $T_{min} = 30\,mK$ by diluting liquid He^3 in liquid He^4. This mixing process is highly endothermic, thus extracting heat from its surroundings.

R (I) Temperature Dependency of SnTe Weak Links

In order to allow quantitative analysis, a crucial condition is that the devices have to possess a zero-resistance state over the proximity coupled weak links. The *differential resistance* $dV/dI = 0\,\Omega$ state demonstrates an entirely superconducting device with successfully proximity-induced superconductivity over the otherwise resistive weak links. The dV/dI measurements are performed in current-biased manner, which offers precise control of the super-

conducting state. *Figure 36* shows the current-biased dV/dI curves of mesoscopic junctions consisting of Nb ((a) and (c)) and Ta ((b) and (d)) superconducting leads. The leads of the Nb (Ta) based devices are seperated by length $L = 150nm$ ($L = 200nm$). The Nb devices show a defined $dV/dI = 0\,\Omega$ state only for $T \leq 85mK$, with a critical current in the magnitude of $I_{sd} \simeq 1.5\mu A$. Critical currents of comparable magnitude have been reported for other device systems consisting of thin film *S-TI-S* junctions of comparable dimension[128,129]. Due to the moderate I_c the Nb based devices are nearly free of thermal hysteresis, as indicated in (d) by current forth (back) sweeps illustrated in red (blue). The Ta-based devices show stronger proximity coupling, which is in a sense counter-intuitive, as the induced superconductivity is dependent, among other parameters, on the T_c of the parenting superconductor, which would under naive assumptions represent the scenario of stronger induced superconductivity for Nb-based systems. This is attributed to the reduced quality of the Nb. Due to its high chemical activity, Nb films are known to often suffer considerably under lithograpic processes (reacting with resist, developing agents etc.), resulting in reduced physical properties, e.g. transition temperatures[130]. Ta, on the other hand, is resilient and not reported to suffer degradation from conventional processing. However, the $dV/dI = 0\,\Omega$ state is already given for $T \leq 750\,mK$. For $T = 600\,mK$ the Ta-based devices already show $I_c = 10\,\mu A$ and are thus affected by thermal hysteretics as shown in yellow (teal) current forth (back) sweeps in *figure 36* (b)). At $T = 85\,mK$ the critical current of the Ta based devices is boosted to $I_c = 130\,\mu A$, as illustrated in *figure 36* (d). Due to the high critical current, the device heating results in *giant thermal hysteresis*. The origin of these extraordinary high I_c values in the

[128] Oostinga et al. *Phys. Rev. X*, 3(021007):1–7, 2013
[129] Williams et al. *Phys. Rev. Lett.*, 109(056803):1–5, 2012
[130] Bruno et al. *Physics Procedia*, 36:239–244, 2012

Ta/SnTe/Ta devices remains puzzeling. For further clarification the temperature depedence of the I_c values is investigated in the range between $T = 85mK$ and $T = 700mK$ and analyzed with respect to the different transport scenarios in the clean, dirty and intermediate regime. The fitting is done analog to section *Modelling the Temperature Dependence of Josephson Currents* in PART II. The resulting data is presented in *figure 37*. The data (marked in red) can be fitted with the *Eilenberger formalism* (teal) for ballistic transport, but shows considerable data agreement only in the temperature window $T \geq 300\,mK$. The fit results in a superconducting coherence length $\xi_{Eilenberger} = \frac{hv_F}{2\pi k_B T_c} = 61\,nm$ and a coherence length $l_e^{Eilenberger} = 101\,nm$ of ballistic channels for $T_c^{Eilenberger} = 1.98\,K$. Both, $l_e^{Eilenberger}$ and $T_c^{Eilenberger}$ are in agreement with the measured L_Φ surface state coherence length in the HLN framework and the T_c of the *Ta* thin films. It is further found that the transparency parameter D does not influence the fit quality or the parameter $\xi_{Eilenberger}$. Combined with the chosen lithographic layout, in which the S covers the TI across the entire device except the weak link, it can be concluded that altering effects originating in bad interface transparency are neglectable in further measurements[131]. However, the entire $I_c(T)$ scenario can be well fitted with the *analytical procedure* (purple) of transport in the intermediate regime. Transport in this regime type has been reported by other groups for several *S-TI-S* devices describing 2D electronic transport with strong bulk shunt[132,133]. The fit results in the Thouless energy $E_{th} = 65.59\,\mu eV$. Connected through $E_{th} = k_B T$, this gives a temperature $T_{th} = 0.74\,K$, which matches the first appearing $dV/dI = 0\,\Omega$ state for the *Ta/SnTe/Ta* devices. Furthermore, it allows to draw conclusions about the fermi velocity v_F in the 2D transport through the connection $E_{th} = \hbar v_F / L$,

[131] Marmorkos et al. *Phys. Rev. B*, 48(4):2811–2814, 1993

[132] Veldhorst et al. *Nat. Mater.*, 11:417–421, 2012

[133] Galetti et al. *Phys. Rev. B*, 89(134512), 2014

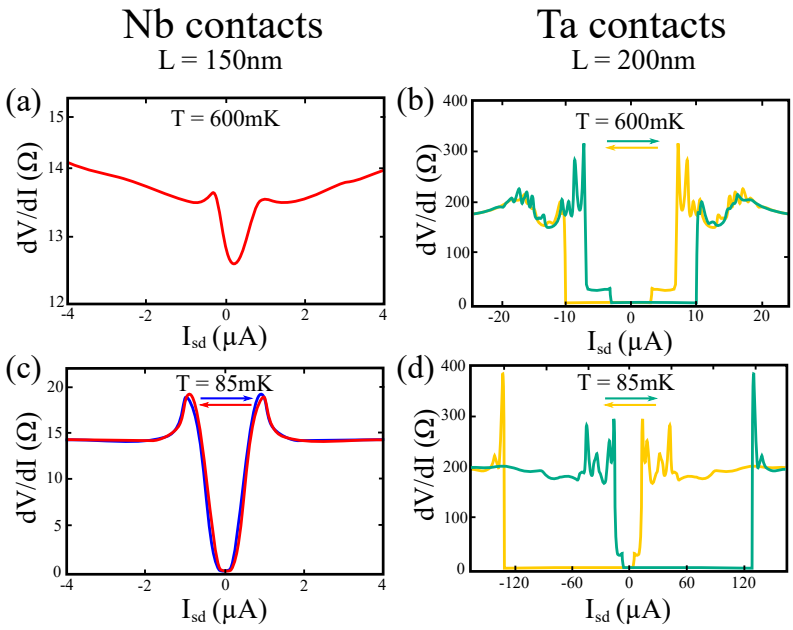

Figure 36: Current-biased dV/dI measurements of SQUIDs consisting of superconducting *Nb* and *Ta* leads. The data is measured at $T = 600\,mK$, which is presented in (a) and (b), and $T = 85\,mK$ as shown in (c) and (d). The SQUIDs consisting of *Nb* leads are in the $dV/dI = 0\,\Omega$ state only below $T = 85\,mK$ and possess a moderate critical current $I_c = 1.5\mu A$. The SQUIDs consisting of *Ta* leads posses a defined $dV/dI = 0\,\Omega$ state even at $T = 600\,mK$ and huge critical currents $I_c = 130\,\mu A$ at $T = 85\,mK$. Due to the high I_c the devices show strong thermal hysteresis.

giving $v_F = 1.83 \times 10^4\,ms^{-1}$ at $T = 700\,mK$ and $L = 200\,nm$. This value is one order of magntiude lower than the fermi velocities extracted from the Hall data analysis, but still within reasonable dimensions in comparison to theoretical predictions[134]. Fitting the data with the *Usadel* approach does not yield in a self-consistent scenario for any temperature window. Hence, transport described by a disordered system frame can be excluded for the investigated devices. In conclusion, the presented data strongly suggests bulk shunted surface state transport. Due to the fit agreement, and to counter the strong thermal device hysteretics originating in high I_c values, further measurements are mostly set in the temperature window $300mK \leq T \leq 700mK$.

[134] Hsieh et al. *Nat. Commun.*, 3(982):1–6, 2012

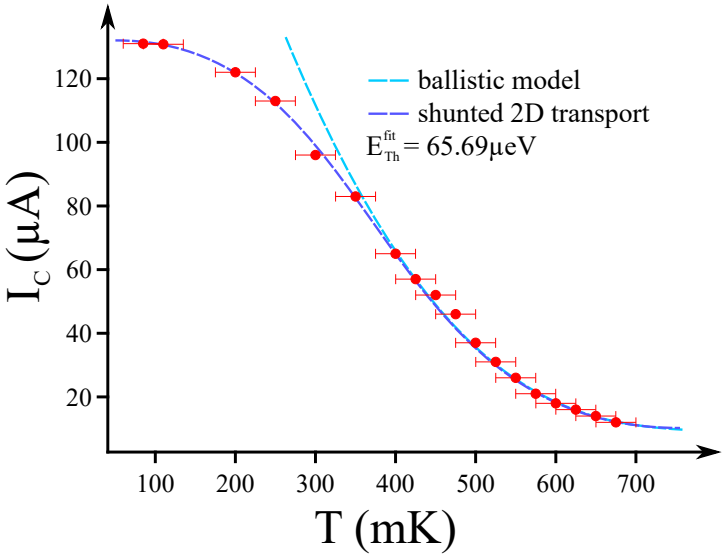

Figure 37: $I_c\,(T)$ dependence of a *Ta*-based JJ with a *SnTe* weak link with $L = 200\,nm$ length. The data is fitted with the Eilenberger formalism for ballistic transport and the analytical model for 2D bulk-shunted transport. The 2D bulk-shunted fit results in $E_{th} = 65.69 \mu eV$. Treating the measurements in the Usadel model does not end in a self-consistent scenario. Consequently, the transport regime is placed between the *intermediate* and the *clean limit*.

$R\,(I)$ Dependence on the Length of the SnTe Weak Links

For the *Nb*-based devices the influence of the length of the weak links is tested at $T = 85\,mK$. In *figure 38* (a) - (c) the current biased dV/dI measurements for weak link lengths $L = 50\,nm$, $L = 120\,nm$ and $L = 200\,nm$ are shown. The lengths of the weak links cover the range of the phase-coherence length L_Φ of the surface state electrons evaluated by the HLN analysis. Therefore, if surface state properties are contributing to the transport, the features resulting from proximity of the TSSs to the *Nb* should be most prominent for $L = 50\,nm$ in the dV/dI data (presented in *figure 38*(a)). For currents lower than $I_{sd} = 1.89\,\mu A$, a dissipationless supercurrent can flow through the system and the device exhibits a clear zero-resistance state, as demonstrated in the previous section. For larger currents the device can be characterized by its normal state resistance $R_n = 12\,\Omega$. Small thermal hysteretic behavior is present. The most prominent features in this dV/dI

data are the pronounced peaks flanking the outer-gap sides while sweeping forth (back) from the resistive into the superconducting state at $I_c = \pm 1.91\,\mu A$. Interestingly, when sweeping forth (back) from the non-resistive region, the device jumps at the same current back into the resistive state, where the back (forth) bias current reveals the prominent peak. We attribute these peaks to the contribution of TSSs carrying supercurrents. In this picture surface ABSs generated in analogy to the mirror-protected Dirac points on the (001) surface of the *SnTe* crystal can host CPs, which are robust and manifest themselves as additional peaks outside the bulk superconducting gap. HASHIMOTO ET AL.[135] predicted such mirror-protected surface ABSs hosted in superconducting TCIs on the (001) surface if an unconventional odd-parity superconducting potential is realized. In *figure 38*(b) the length of the weak link corresponds to the estimated coherence lengths of the surface channels ($L = 120\,nm$) and hence features of the surface ABS are expected to be weakened. The induced superconductivity still shows a zero-resistive behavior in the gap, but the observed gap-flanking surface ABS peaks have vanished. Interestingly, the superconducting gap does not show a sharp jump as in *figure 37*(a), but appears to be tilted outwards, which suggest that pure s-wave superconductivity is unlikely to be present. If superconductivity is partially carried by TSSs, it is theoretically predicted that a mixture of s- and p-wave pairings is present[136]. In *figure 38*(c) the dV/dI measurement of a device with the weak link length $L = 200\,nm$ is evaluated. At this length, a superconducting gap is still observable, but does no longer exhibit a $dV/dI = 0\,\Omega$ state, keeping a finite resistance $R_n \approx 55\,\Omega$. This result supports the suggestion that the phase-coherence lengths of the TSSs and the phase-coherence lengths of the CPs are correlated and have

[135] Hashimoto et al. *Phys. Rev. B*, 92(174527):1–8, 2015

[136] Fu and Kane. *Phys. Rev. Lett.*, 100(096407), 2008

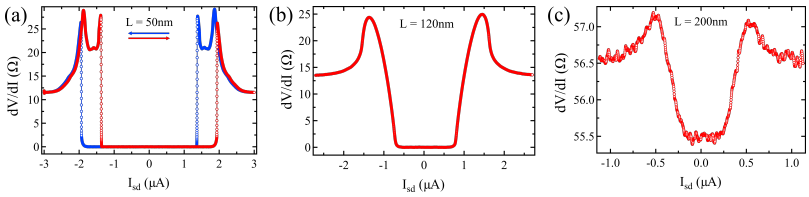

Figure 38: Current-biased dV/dI measurements of *S-N-S* devices with *SnTe* weak links. The length gap L between the *Nb* superconducting wires is varied between (a) $L = 50\,nm$, (b) $L = 120\,nm$ and (c) $L = 200\,nm$. The data is measured at $T = 85\,mK$.

crucial influence on the proximity induced superconductivity in the investigated TCI films.

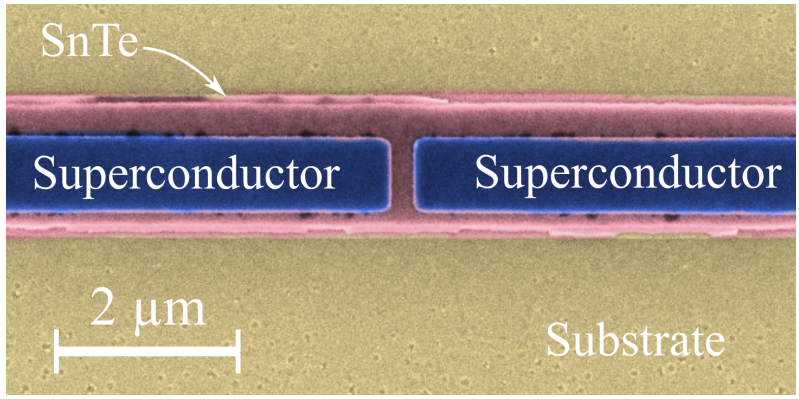

Figure 39: False color SEM image of a *S-N-S* JJ consisting of a *SnTe* weak link (pink). The superconducting material is *Ta* (blue). The effective area of the weak link is estimated to $A_{eff}^{JJ} = 0.32\mu m^2$.

Magnetic Field Dependence of Josephson Junctions with SnTe Weak Links

After investigating the proximity superconductivity and the classification of the transport regime, the magnetic field response of single weak links can be analyzed. Therefore, JJs like the one depicted in the false color SEM image in *figure 39* are tested with an out-of-plane orientated magnetic field B_z. The *Ta* (blue) is placed on top of the thin mesa of *SnTe* (pink). The effective area of the JJ is estimated at $A_{eff}^{JJ} = 0.32\mu m^2$. To counter the strong thermal hysteresis, the magnetic field mapping is measured at $T = 650\,mK$, firmly within the temperature window $300\,mK \leq T \leq 700\,mK$, showing transport characteristics of ballistic and 2D bulk shunted transport.

Interestingly, an anomalously shaped Fraunhofer pattern is observed for the *Ta/SnTe/Ta* weak link in *figure* 40. The Fraunhofer diffraction pattern for a conventional *S-N-S* JJ of the same effective area would yield a magnetic field response corresponding to the black dashed line. The anomalous pattern can not be attributed to the 4π-periodic Josephson effect (and thus MBSs) predicted by

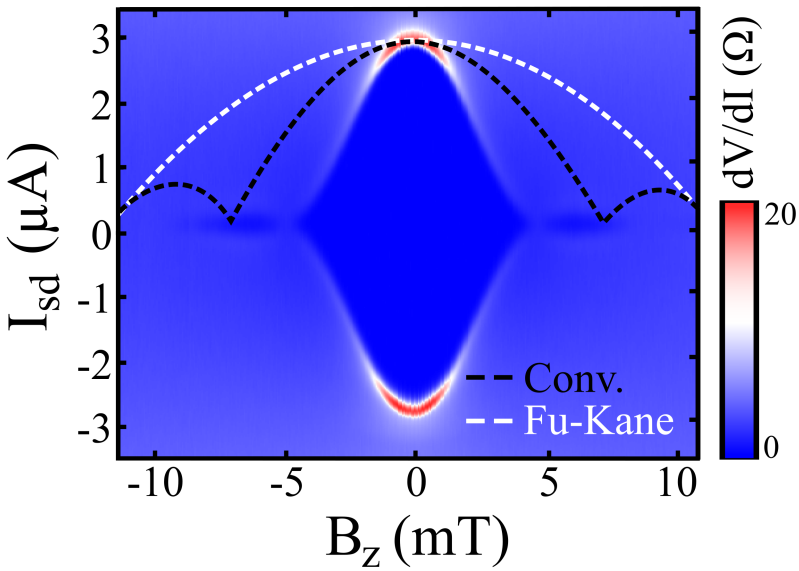

Figure 40: Magnetic response of a JJ with a *SnTe* weak link. An anomalous Fraunhofer pattern can be observed, deviating from the pattern of a conventional JJ (indicated in black). The deviation can not be attributed to the Fu-Kane model (white). The data is measured at $T = 650\,mK$.

the Fu-Kane scenario[137]. This effect would result in a magnetic field response equivalent to the white dashed line. Even if the effective area differs significantly from the taken SEM estimation, fitting the central peak would give periodics at $4.5\,mT$, $9\,mT$, ..., which can not be observed. Further parasitic effects harnessing conventional Josephson experiments, such as the Pearl effect or flux focussing, cannot explain the atypical magnetic field response. However, these *quenched Fraunhofer patterns*, being much smaller and occasionally resolving only the first critical current maxima, have recently been found in other *S-TI-S* JJs and are attributed to current inhomogenities within the weak links due to the presence of TSSs[138,139,140]. Further clarification of the origin of the anomalous Fraunhofer pattern can be obtained through RF driven experiments, which are insensitive to all effects of geometrical nature. The RF measurements are discussed in the following chapter.

[137] Fu and Kane. *Phys. Rev. Lett.*, 100(096407), 2008

[138] Suominen et al. *Phys. Rev. B*, 95(035307):1–11, 2017
[139] Qu et al. *Sci. Rep.*, 2(339): 1–5, 2012
[140] Williams et al. *Phys. Rev. Lett.*, 109(056803):1–5, 2012

RF Measurements at SnTe Based Josephson Junctions

To find an explanation for the unconventional Fraunhofer pattern detected in the magnetic field response of the TCI JJs, AC Josephson measurements are taken at the *SnTe* weak links. Recently, microwave driven measurements have proven a powerful tool in investigations of topological weak links, as they enable transport testing on a much shorter time scale compared to DC analyses[141]. Furthermore, Shapiro response is known to be insensitive to effects originating in sample geometry rather than of superconducting current-phase effects[142]. Therefore, JJs as depicted in *figure 39* are subjected to microwave exposure. To test the occurance of ambient Shapiro response, current-biased dV/dI scans are measured as the microwave frequency f_{rf} is tuned. The rf power in these measurements is held constant at $P_{rf} = 0\,dBm$ and the data is measured within the upper limit of the temperature window $T = 700\,mK$ to minimize self-heating influences as consequence of high I_c values. The obtained data is visualized in *figure 41.* The rf exposure strongly influences the superconducting state of the device and Shapiro transitions are observed in the frequency window $1\,GHz \leq f_{rf} \leq 2\,GHz$, which is highlighted by the yellow rectangle within the plot.

For further rf analysis, the microwave frequency is set to $f_{rf} = 1.768\,GHz$. To elucidate the Shapiro evolution, the microwave power P_{rf} is varied while the current-biased dV/dI sweeps are measured. The resulting data is presented in *figure 42* and shows distinct $dV/dI = 0\,\Omega$ plateaus indicating the individual Shapiro steps. The individual Shapiro steps $n = 1, 2, 3, ...$ are labeled within the plot and show no steps being suppressed. Thus, no feedback of the fractional AC Josephson effect, as reported for

[141] Bocquillon et al. *Nat. Nanotechnol.*, 12:137–143, 2017

[142] Chiodi et al. *Phys. Rev. B*, 86(064510), 2012

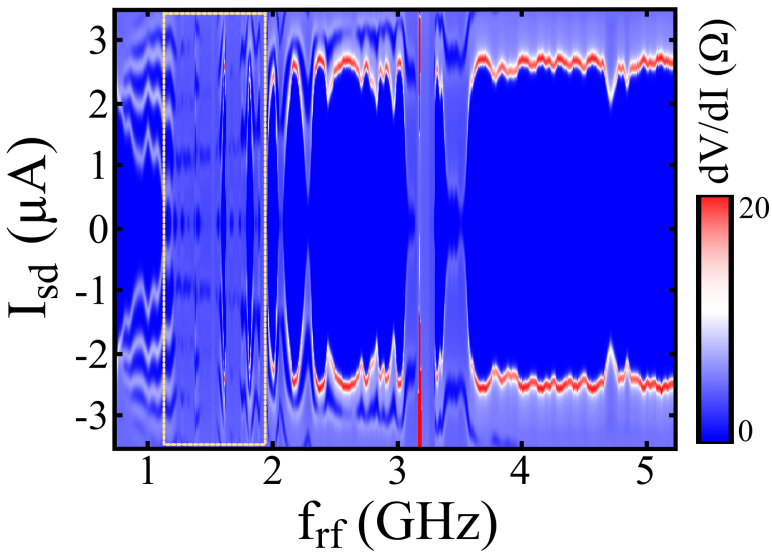

Figure 41: Dependency of the superconducting state measured by $dV/dI\,(I_{sd})$ on the frequency f_{rf} of the rf irradiation. The yellow border indicates the frequency window where Shapiro steps occur. The data is measured at microwave power $P_{rf} = 0\,dBm$ and $T = 700\,mK$.

2D TIs[143], 3D TIs[144] and Dirac semimetals[145] is found in the investigated JJs. Interestingly, recent rf experiments conducted on $Pb_{0.5}Sn_{0.5}Te$ TCI weak links by Snyder et al.[146] have also revealed the presence of all Shapiro steps. Further $dV/dI = 0\,\Omega$ substates between the primary Shapiro steps have been reported by them, which were attributed to the presence of saw-tooth CPRs of ballistic surface channels. Despite the measurements in this thesis not having been able to resolve the intermediate $dV/dI = 0\,\Omega$ states, the data matches up. Due to the fairly high base temperature $T = 700mK$, the measurements are strongly affected by enviromental thermal broadening. The resulting thermal smearing is the same magnitude as the reported substate features and would therefore mask their presence. Measurements at lower setup temperature T resulted in strong device self-heating and were unable to support to these statements. Thus, to conclude, the presence of all Shapiro steps in the $SnTe$ weak links has been demonstrated

[143] Bocquillon et al. *Nat. Nanotechnol.*, 12:137–143, 2017
[144] Wiedenmann et al. *Nat. Commun.*, 7(10303), 2016
[145] Yu et al. *arXiv preprint*, arXiv:1801.04365v1:1–25, January 2018
[146] Snyder et al. *arXiv preprint*, arXiv:1710.06077v2: 1–5, November 2017

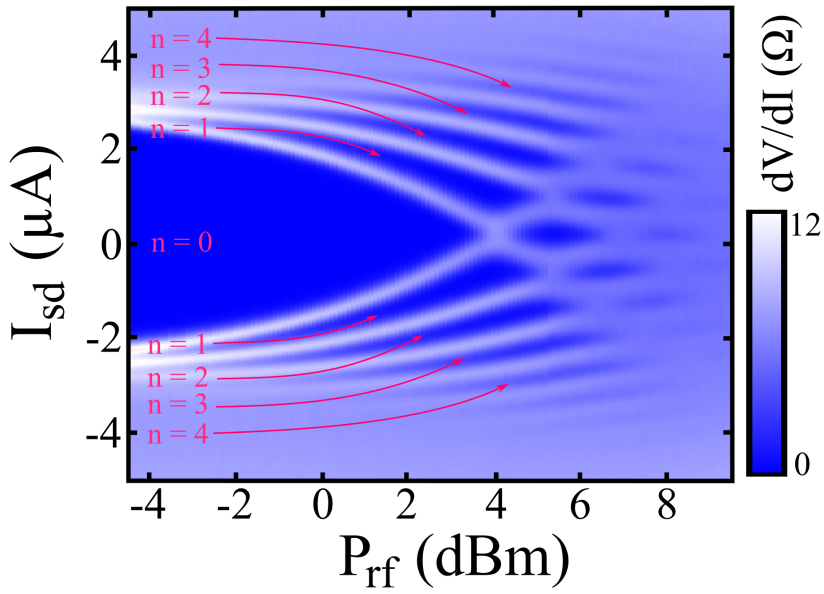

Figure 42: Influence of the microwave power P_{rf} on the superconducting $SnTe$ weak link. Clear $dV/dI = 0\Omega$ resistance plateaus indicate the Shapiro steps. The steps n are highlighted in pink. The $n = 1$ step is present and only conventional rf response is observed. The data is measured at $f_{rf} = 1.768\,GHz$ and $T = 700\,mK$.

and no fractional AC Josephson effect could be observed. Due to thermal limitation of the Shapiro measurements, two possible scenarios for the anomalous Fraunhofer pattern observed in the DC Josephson effect remain open: inhomogenities in the supercurrent distribution within the weak link and saw-tooth shaped ballistic transport.

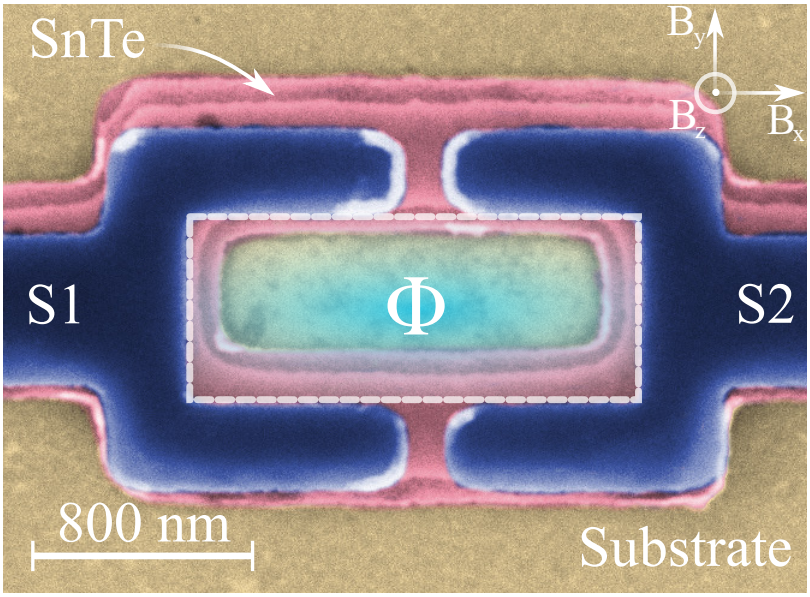

Figure 43: False color SEM image of a SQUID consisting of TCI *SnTe* (pink) weak links. The superconducting leads *S*1, *S*2 are highlighted in blue. The effective area surrounded by the superconducting leads S1, S2 (blue), where magnetic flux Φ can pass, is highlighted (teal).

Magnetic Field Dependence of SQUIDs with SnTe Weak Links

After the electrical characterization of single *S-N-S* JJs, the next aspect that can be approached is the transport analysis of two *S-N-S* JJs in parallel circuit. Here, SQUIDs as depicted in *figure 43* are patterned in various geometries. The color code of the SEM image is chosen as previously: the *SnTe* film is highlighted in pink, and the superconducting leads S1, S2 are colored blue. The effective SQUID area, penetrated by the magnetic flux Φ, is marked by the teal-colored zone surrounded by a white dashed line. To allow a discussion independent of the device geometry (i.e. different effective SQUID areas), the out-of-plane magnetic field B_z response will be given in units of magnetic flux dependence Φ/Φ_0.

Nb-Based SQUIDs

The magnetic field response of the current-biased differential resistance dV/dI measurements at SQUIDs consisting of $SnTe$ weak links proximized by Nb leads reveal critical current oscillations, which are illustrated as a color-coded plot in *figure 44.* The data is measured at $T = 85\,mK$. *Figure 44*(a) shows that the oscillations persist over a wide spectrum of magnetic flux, but show no modulated Fraunhofer influence caused by the finite JJ area. The SQUID pattern is symmetric and shows no kinetic inductance influence. In *figure 44*(b), a finely resolved measurement of the normalized magnetic flux between $0 \leq \Phi/\Phi_0 \leq 7.5$ is shown. The oscillations perfectly match the conventional Φ_0 periodicity and no anomalous SQUID responses are observed. This has also been reported for DC SQUID measurements of devices constituted of other topological materials[147,148]. Yet it has to be noted that the measured data has been offset to $I_c\,(0) = max$. The exact cause of the shifted pattern could not be determined. Such scenarios are reported for unconventional *p-wave* and *d-wave* superconducting pairing[149]. Despite additional supporting evidence obtained from the length varied $dV/dI\,(I_{sd})$ measurements, this is unlikely to apply to the investigated samples because of the immense bulk activation. As no gate-dependent measurements for the $Nb - SnTe - Nb$ SQUIDs are conducted, this suggested scenario remains disputable and has to be considered with caution. Thus, it has to be concluded that the $Nb - SnTe - Nb$ SQUIDs show conventional I_c response and no unconventional 4π-periodic modulation is encountered. The absence of anomalous modulation is attributed to 2π-signal poisoning caused by supercurrents carried by dominating bulk channels.

[147] Maier et al. *Phys. Scr.*, T164 (014002):5–8, 2015
[148] Qu et al. *Sci. Rep.*, 2(339): 1–5, 2012

[149] Wollmann et al. *Phys. Rev. Lett.*, 71(2134), 1993

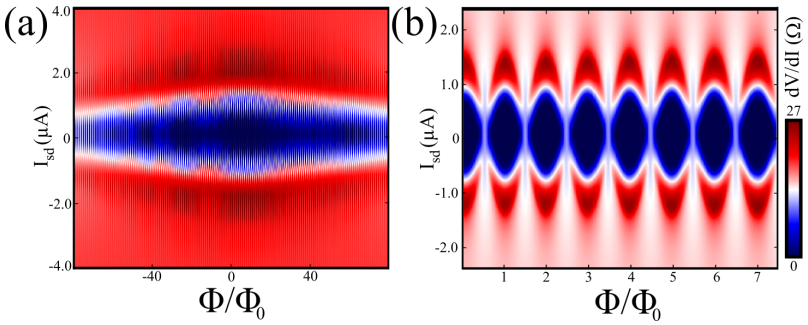

Figure 44: (a) Oscillations of a DC SQUID consisting of *SnTe* weak links with *Nb* superconducting leads. (b) Finely resolved measurement around zero magnetic flux Φ, revealing perfectly matching conventional oscillation periods of $\Phi/\Phi_0 = 1$. The data is measured at $T = 85\,mK$. The data in (b) has been offset to $I_c(0) = max$.

Ta-Based SQUIDs

The magnetic field response of the current-biased differential resistance dV/dI measurements at SQUIDs consisting of *SnTe* weak links proximized by *Ta* leads reveal the critical current oscillations illustrated as a color-coded plot in *figure 45*. The data is measured at $T = 625\,mK$. Regarding the *Nb*-based SQUIDs, the $Ta - SnTe - Ta$ devices show clear oscillations of the critical current in dependence of the penetrating magnetic flux, as illustrated in *figure* $45(a)$. However, the main difference between *figure* $44(a)$ and *figure* $45(a)$ is that the measurements at the *Ta*-based SQUIDs show a strong asymmetrical SQUID response. Since the investigated SQUIDs are patterned with symmetric JJs, this feature has to be attributed to the huge kinetic inductance L_k of the weak links[150], which would fit in the naive image of ballistic transport carried by narrow sized TSSs. In *figure* $45(b)$ a more finely resolved dV/dI measurement in the normalized magnetic flux window $25 \leq \Phi/\Phi_0 \leq 36.5$ is shown. Again, no unconventional modulations or higher harmonics in the SQUID pattern due to contributing 4π-periodic ABS are observed. The $I_c(\Phi)$ dependence shows a nearly triangular shape of the CPR characteristic for long JJs afflicted by high L_k. To further elucidate the L_k influence and

[150] Faucher et al. *Physica C*, 368:211–217, 2002

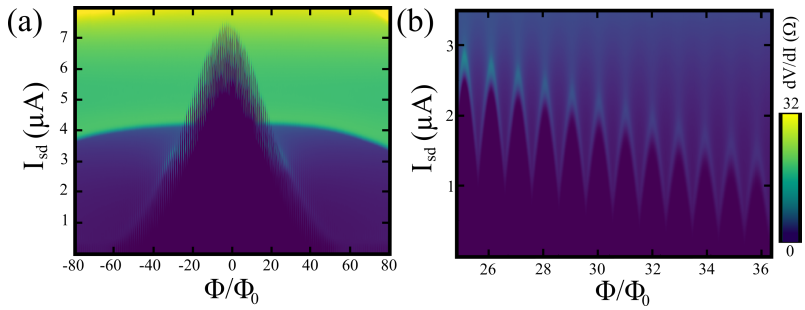

Figure 45: Magnetic field response mappings of *Ta* based DC SQUIDs consisting of *SnTe* weak links. (a) shows a huge kinetic inductance background. (b) finely resolved measurement of the $I_c(\Phi)$ oscillations. The oscillations match conventional behavior with width $\Phi/\Phi_0 = 1$. The data is measured at $T = 625\,mK$.

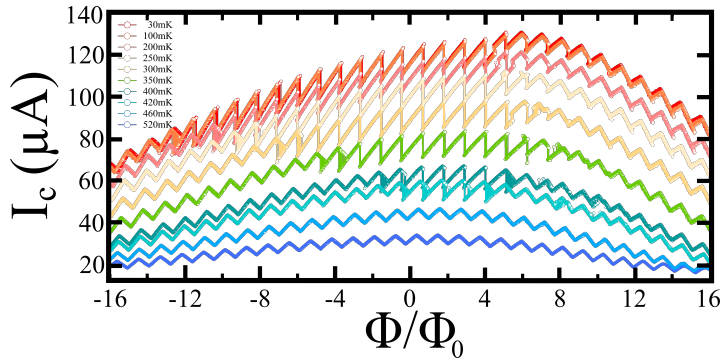

Figure 46: Evolution of the critical current $I_c(\Phi)$ oscillations for several temperatures T in the interval $30\,mK \leq T \leq 520\,mK$. A strong increase in the kinetic background and I_c is observed as T is decreasing. Furthermore, a change in the CPR from triangular to saw-tooth shape occurs for $T < 420\,mK$.

the CPRs of the *SnTe* weak links, temperature depedent I_c measurements are performed. The resulting data for temperatures in the range between $T = 30\,mK$ and $T = 520\,mK$ is visualized in *figure 46*. As discussed in the section *R(I) Temperature Dependence of SnTe Weak Links*, the *Ta*-based SQUIDs gain a a huge increase in I_c's for lower temperatures, up to $I_c = 131\mu A$ at $T = 30\,mK$. The higher the I_c, the higher the influence of the L_k background. Interestingly, the data reveals a transition from a triangular CPR ($T > 420mK$) to a saw-tooth CPR for $T \leq 420mK$. The origin and explanation of the *SnTe* CPR is given in the following section.

CPR of SnTe Weak Links

As described in the section *The Current-Phase Relation of a Josephson Junction* of PART II, a saw-tooth CPR is predicted for ballistic transport in TSSs. The CPR data shown in *figure 47* can therefore be fitted by equation 23 after the substraction of the kinetic inductance affected I_c background. The resulting fit matches the data perfectly and yields a quasi-ideal transmission parameter $t = 0.949$. The amplitude and the resilience to high magnetic fields of the current oscillations match the expectations for ballistic transport in 1D channels. An estimation of the current-confinement can be made by considering $W_{confined} = \Phi_0 / B_{max}\, L$, which results in a narrow region $W_{confined} \leq 10.9\, nm$ in space for $B_{max} = 0.6\, T$ and $L = 200\, nm$. The theoretically predicted supercurrent carried by one channel for a long JJ[151] is estimated to $I_{1D} \simeq e v_F / L \approx 292\, nA$, with $v_F = 3.6 \times 10^5 ms^{-1}$ measured in the Hall analysis of the bare *SnTe* films. Following the same reasoning discussed within the HLN analysis, a *SnTe* TCI shows four TSSs in (001) direction of the SBZ. Considering the four current-carrying surfaces of the weak link, one ends up with $I_{1D} \approx 4 \times 4 \times 292\, nA \approx 4.67 \mu A$, which matches closely with the measurements in *figure 47*. At this point, one may raise the question whether the measurements provide explicit evidence for ballistic transport by TSSs. Even though the high kinetic inductance, the appearance of saw-tooth CPR and matching system parameter estimations are all strong indicators for surface state carried transport, opinions differ on this topic. Despite distortions induced by self-induction through the high currents and the huge kinetic inductance can be excluded due to $\beta_L \simeq 0.03 - 0.1 \ll 1$, it has been well-investigated that flux-freezing effects in weak links of JJs and SQUIDs are able to mimic

[151] Beenaker et al. *Phys. Rev. Lett.*, 110(017003), 2013

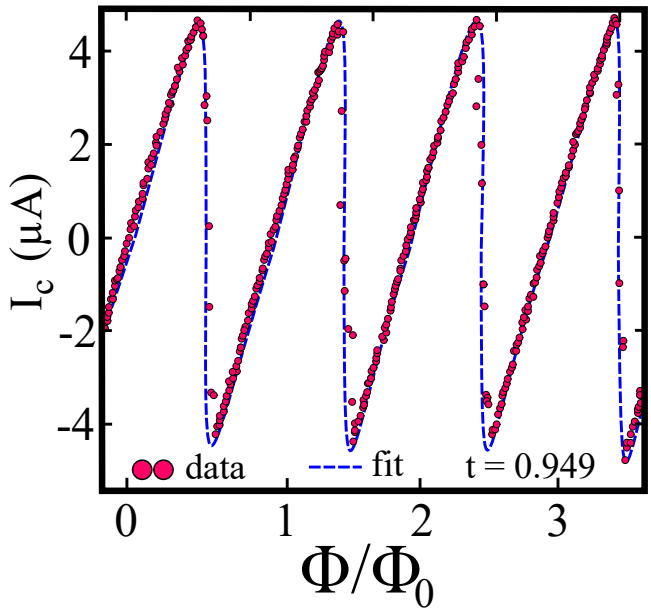

Figure 47: Saw-tooth CPR of a SQUID with *SnTe* weak links. The $I_c(\Phi)$ kinetic inductance background has been subtracted. Data fitting of the quasi-ideal saw-tooth CPR yields $t = 0.949$ for ballistic transport channels. The data is measured at $T = 30\,mK$.

ideal saw-tooth shaped CPRs[152]. The collected data is unable to explicitly refute this argument. Yet we argue that this is unlikely to be the case, as no magnetic hysteresis was found in any device, which would inevitably occur for trapped flux[153]. However, while available data does not have unequivocal proof, it does provide strong evidence for TSS contributed transport in the TCI weak links. One way of clarifying this argumentation are gate-voltage tuned transport measurements at the SQUIDs, as, compared to TSSs, flux-freezing would be less influenced by the niveau of the chemical potential in a given system. The gated SQUID measurements are discussed in the following section.

[152] Arutyunov et al. *Sci. Rep.*, 2012

[153] Mizuno and Aomine. *Jpn. J. Appl. Phys.*, 26:1607–1608, 1987

Electrical Gating of SnTe SQUIDs

To further test the TSSs in the *SnTe* weak links, SQUIDs are designed that possess local gates above each junction. Such a SQUID is pictured in the false color SEM image in *figure 48*. The color code is chosen as before: the *SnTe* is marked in pink and the superconducting leads are highlighted in blue. The gate electrodes (colored golden) consist of $5\,nm\ Ta/75\,nm\ Au$ and are placed directly on top of each weak link. To serve as dielectricum, $100\,nm\ Al_2O_3$ are deposited in advance via atomic layer deposition at $T = 120\,^{\circ}C$ on top of the device. This technique is known to result in smooth insulating films, which can withstand dielectrical breakdown up to high electric field strength[154]. Additionally, Al_2O_3 is a well established "*high - k material*" frequently used in gating experiments due to its high polarization efficiency[155].

In order to investigate the influence of the local gate voltages $V_{G,1}$ and $V_{G,2}$, the SQUID sensitivity dI_c/dB_z is shown as a function of magnetic field B_z for a gate voltage range $-20\,V \leq V_{G,i} \leq 20\,V$. For neither of the two weak links, a change in the SQUID modulation can be observed as $V_{G,i}$ is varied. This effect is attributed to the strong bulk activation and the high carrier concentrations $n \simeq 1 \cdot 10^{21}\ cm^{-3}$ observed by Hall measurements in the *SnTe* thin film characterization. Such high carrier concentrations screen the electrical fields applied by the gates. Thus, in order to test the TCIs via local gates, one has to first gain control of the strong doping effects reported to be a major challenge in this material family[156]. Because of this, no gate dependence on the superconducting devices with *SnTe* weak links can be reported in the frame of this thesis. Without the possibility to fine-tune the chemical potential μ in the electronic gap of the *SnTe* mesa and deplete the strong

[154] Puurunen. *J. Appl. Phys.*, 97(121301), 2005

[155] Brennan et al. *Appl. Phys. Lett.*, 101(211604), 2012

[156] Sist et al. *IUCrJ*, 3(5):377–388, 2016

bulk transport contribution, the investigation of MBSs is restricted at this point. Further effort in reducing the high carrier concentration of the $SnTe$ films will be necessary here. One possibility is counter-doping by preparing off-stochiometric $Pb_xSn_{(1-x)}Te$ films. This approach has recently been demonstrated as a promising alternative[157].

[157] Assaf et al. *Sci. Rep.*, 6 (20323), 2016

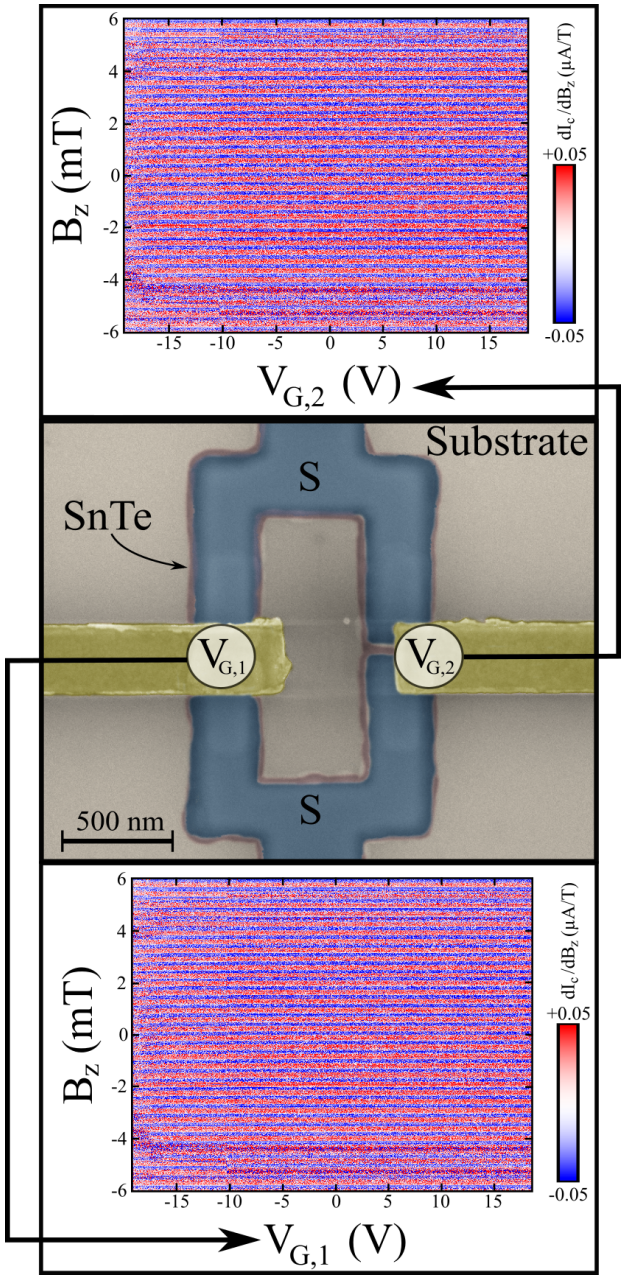

Figure 48: A false color SEM image of the $2 \times 0.5\,\mu m^2$ SQUIDs with local gates at each *S-N-S* junction is shown in the middle. For each local gate voltage the SQUID dependency of gate voltage $V_{G,1}, V_{G,2}$ is investigated. Therefor the DC SQUID sensitivity dI_c/dB_z is measured as function of magnetic field B_z while one gate is tuned between $-20\,V \leq V_{G,1/2} \leq 20\,V$. No change in the SQUID response is observed over the entire voltage regime. The independency of V_G is attributed to the metallic character of *SnTe*.

SQUID Measurements Assisted by In-Plane Magnetic Fields

With the independence of gate voltages caused by the strong metallicity of the TCI material, a key diagnostic for local device control is lost. For further testing of the induced superconducting state, the samples are subjected to assisting in-plane magnetic fields $B_{x,y}$, which act as Zeeman splitting fields. Interestingly, for $B_x = 204mT$ a $0 - \pi$ transition of the SQUID is observed, as illustrated in *figure 50(a)*. The $I_c(\Phi)$ data shows a clear shift of the superconducting phase $\varphi = \pi$ relative to each other. To give a clearer picture of said shift, the $\varphi = 0$ state for $B_x = 200\,mT$ and the $\varphi = \pi$ state for $B_x = 204\,mT$ is offset in *figure 50(b)*. The $\varphi = \pi$ state is highlighted in green, whereas the $\varphi = 0$ state is labeled by a yellow background. For in-plane magnetic fields $200\,mT < B_x < 204\,mT$ a change in the $I_c(\Phi)$ SQUID periodicity from Φ_0 to $\Phi_0/2$ is found. Such HIFQ $\Phi_0/2$ excitations are known to appear at transitions between $\varphi = 0, \pi$ phases of superconducting quantum states, which were discussed in section *Integer and Half-Integer Flux Quantization* of PART II. If they are induced by externally applied Zeeman fields, they are the manifestation of exchange field-induced spatial oscillations of the superconducting order parameter and hence superconductivity carried by finite momentum CP with non-zero COMM. Entering the FFLO regime would not only access $\varphi = 0, \pi$ phases, but enable the demonstration of φ_0-junction behavior of the TCI weak links by the *Zeeman modulation* of the order parameter. For further testing, mappings of the ciritical current I_c in dependence of normalized flux threading Φ/Φ_0 and in-plane Zeeman fields along the x-direction in range of $-400\,mT \leq B_x \leq +400\,mT$ are performed. The resulting data, measured at $T = 500\,mK$, is shown as a color-

contour plot in *figure 51(a)*. As before, clear SQUID oscillations $I_c(\Phi)$ are observed, which are not influenced by small Zeeman fields $|B_x| \leq 165\,mT$. The slight tilt of the pattern as a function of B_x is attributed to the imperfect alignment of the SQUID within the $3D$-vector magnet, enabling in-plane magnetic field components to thread through the effective SQUID area in out-of-plane direction. In the range of $\pm 165\,mT \leq B_x \leq \pm 185 mT$, the I_c of the SQUID is strongly suppressed and hence only weak $I_c(\Phi)$ oscillations can be observed. This repeats for $\pm 185\,mT \leq B_x \leq \pm 350\,mT$, where I_c is rising once more, strengthening the SQUID oscillations. Here, several interesting points can be found in the data. First, in this regime several B_x controllable $0-\pi$ phase transitions, each accompanied by HIFQ periodicities, are observed and thus confirm a tunable φ_0- DC SQUID based on *SnTe* TCI weak links. To be able to better resolve the φ_0-regime, the data gathered within the shaded box in *figure 51(a)* is plottet as SQUID sensitivity dI_c/dB_z in dependence of normalized flux Φ/Φ_0 and Zeeman fields B_x in *figure 51(b)*. The individual $0-\pi$ shifts are highlighted. Interestingly, the transitions repeat in regular modulation of $\triangle B_x^{0-\pi} \approx 21\,mT$.

The second finding is that the $I_c(\Phi)$ dependence on the B_x field also shows oscillating behavior. By following the *"golden rule"* of superconducting devices subjected to external magnetic fields, which states that every oscillation of I_c in dependence of a magnetic field is a manifestation of magnetic flux penetrating the device to some extend, this means that the Fraunhofer-like dependence observed for $I_c(B_x)$ originates from in-plane flux penetrating the weak links. Since the $I_c(B_x)$ oscillation is periodic for $\triangle B_x \approx 215\,mT$, this yields, at $\Phi_0 = \triangle B_x\, A_{eff}^x$, an effective area $A_{eff}^x \approx 0.01 \mu m^2$. If one considers the profile of the *SnTe* weak

link, this matches the cross section spanned by $A_{eff}^{crossection} = W \cdot t$, where W is the width of a weak link and t its thickness. The patterned width $W = 800\,nm$ and the deposited $SnTe$ thickness $t = 30\,nm$ result in a transversal cross section area $A_{eff}^{transversal} \approx 0.0098\mu m^2$ of the JJ. This suggest circulating supercurrents traveling along the surface of the TCI, providing further evidence for TSS transport contribution. This scenario can be viewed similarly to *Aharanov-Bohm flux* induced by the in-plane Zeeman fields $B_{x,y}$ and is illustrated in *figure* 49. The B_x induced flux modulation effect (FME) (illustrated in pink) is based on a circulating current and is proportional to $A_{eff}^{transversal}$. If subjected to B_y, a change of the flux modulation is expected to happen due to an effective change in the penetrated area $A_{eff}^{longitudinal}$ (which is represented by a green circulating current). A similar effect has recently been demonstrated in 3D TI JJ by Chen et al.[158].

[158] Chen et al. *arXiv preprint*, arXiv:1801.08504v1:1–22, 2018

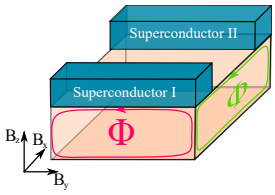

Figure 49: Illustration of the Aharanov-Bohm flux scenario in the individual weak links induced by the in-plane magnetic field causing flux modulation Φ effect in $I_c\left(B_x, B_y\right)$. The effect is caused by circulating currents which are proportional to the dimensions W, L and t of each weak link.

To further discuss this possible scenario it is important to test the influence of the in-plane magnetic field B_{ip}^{α} for different magnetic field angles α. Here, $\alpha = 0°$ $(90°)$ defines the state where the Zeeman field is pointing directly in B_x $\left(B_y\right)$ direction. Considering two essentially different scenarios, which are FFLO physics and Aharanov-Bohm flux modulation, two distinct features are to be expected:

Firstly, if the FFLO state results in a spatially variation of the superconducting order parameter $\triangle_{FFLO}(x)$ and thus inserts a shift in the overall superconducting phase, a strong deformation of the $I_c\left(\Phi, B_{ip}^{\alpha}\right)$ pattern has to occur as the coupling of B_x, B_y does not necessarily has to be equal.

Secondly, if FME is truly the case, the Fraunhofer-like field modulation of $I_c\left(B_{ip}^{\alpha}\right)$ must necessarily differ between B_x and B_y due to the different dimensions of the weak links in longitudi-

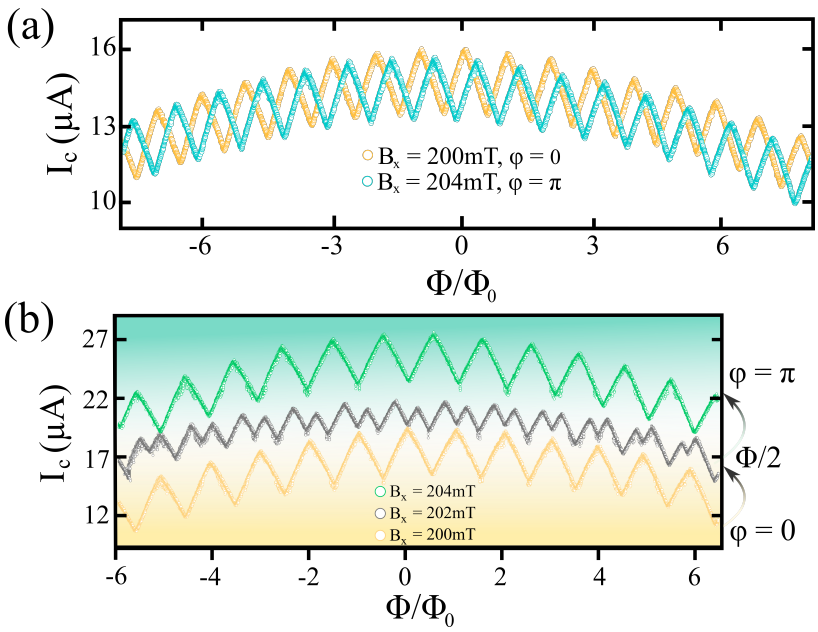

Figure 50: (a) magnetic flux dependence of the critical current I_c in assistance of in-plane magnetic field B_x. The assisting magnetic field induces a π-transition of the SQUID. (b) shows that the transition between $\varphi = 0 \rightarrow \varphi = \pi$ is accompanied by a $\Phi_0/2$ half quantum periodicity. The data is measured at $T = 500\,mK$. The data of (b) is offset for the sake of clarity.

nal transport direction ($\propto L$) and transversal transport direction ($\propto W$).

In *figure 51*, $I_c\left(\Phi, B_{ip}^{\alpha}\right)$ color contour plots for in-plane magnetic field angles $\alpha = 0°, 10°, 20°, 45°, 90°$ are shown, demonstrating the $I_c\left(\Phi, B_{ip}^{\alpha}\right)$ evolution under in-plane magnetic field rotation. The B_{ip}^{α}-rotation alters the I_c interference pattern. By tuning $\alpha = 0° \longrightarrow 90°$, distortions of the SQUID $I_c(\Phi)$ response is visible. This matches with the FFLO induced order parameter oscillations. However, the strongest distortion of the SQUID $I_c(\Phi)$ response is found in in-plane magnetic fields $B_y < 165mT$ at $\alpha = 90°$. Measurements comparable to this one, conducted on topological JJs, found a strong suppression of the modulation effect for one magnetic field direction B_x, B_y. This was attributed to the SML influence of the TSSs, causing only coupling perpendicular to the current-bias direction. We argue therefore that the FFLO transi-

tions in our devices is not restricted to the coupling of TSSs, but suggest RSS-induced coupling to $\triangle_{FFLO}(x)$ as measurable contribution. This conforms to recent findings of giant RSS in *SnTe* systems. $0-\pi$ transitions and entry to φ_0-states in RSS ballistic junction can be expected when the magnetic field induced dephasing equals the dephasing by the propagation time of a given 1D channel. This is achieved, when the Zeeman energy equals the Thouless energy $E_Z = E_{th}$ and thus $g_{eff}\,\mu_B B_{ip} = \hbar v_F / L$. The effective field $\triangle B_{ip}^{0-\pi}$ between two successive $0-\pi$ transitions naturally explains the observed $\triangle B_x^{0-\pi} \approx 21\,mT$ periodicity and yields an *effective g-factor*

$$g_{eff} \approx 52\,.$$

For the calculation of g_{eff} the fermi velocity $v_F = 1.84 \times 10^4\,ms^{-1}$ found through the Thouless energy estimation is used, as they are measured at the same device and were not subjected to any further structuring sequences, which may influence the structural quality of the *SnTe* film. The measured g_{eff} perfectly match the theoretically predicted g values for *SnTe* surface bands along the L-points of the BZ of $g \simeq 60$[159] and $g \simeq 42 - 56$[160].

A periodic feedback of I_c in dependence of B_{ip} (and thus E_Z) is also predicted in the suggested scenario of Pientka et al.[161] for induced topological superconductivity. *Figure 53* illustrates the SQUID response to B_{ip}. Together with the scenario of induced flux Φ_{FME} through FME, the oscillations on the second I_c node, which appear $\triangle B_x^{0-\pi}$ periodically, fit to the zeeman-induced topological superconducting scenario in the planar junction limit. For each $\triangle E_Z = E_{th}$ cycle, the weak links are tuned then through a topologically protected superconducting $\varphi = \pi$ state. In *figure 54*, the evolution of the ABS spectrum of the device is galleried.

[159] Hayasaka and Fuseya. *J. Phys.: Condens. Matter*, 28 (31LT01):1–5, 2016

[160] Bernick and Kleinman. *Solid State Commun.*, 8: 569–575, 1970

[161] Pientka et al. *Phys. Rev. X*, 7(021032), 2017

When the ABS are splitted due to the Zeeman field, I_c is reduced and shows halfed periodicity. The minimum in I_c is obtained for $E_Z^{SQUID} = E_{th}/2$. The data match the theoretical predicitions made by Pientka et al. and provide evidence of stable magnetic field-induced $\varphi = \pi$ states, which occur periodically and are accompanied by a minimum in I_c. On balance the results strongly suggest the presence of topological superconductivity and thus Majorana fermions.

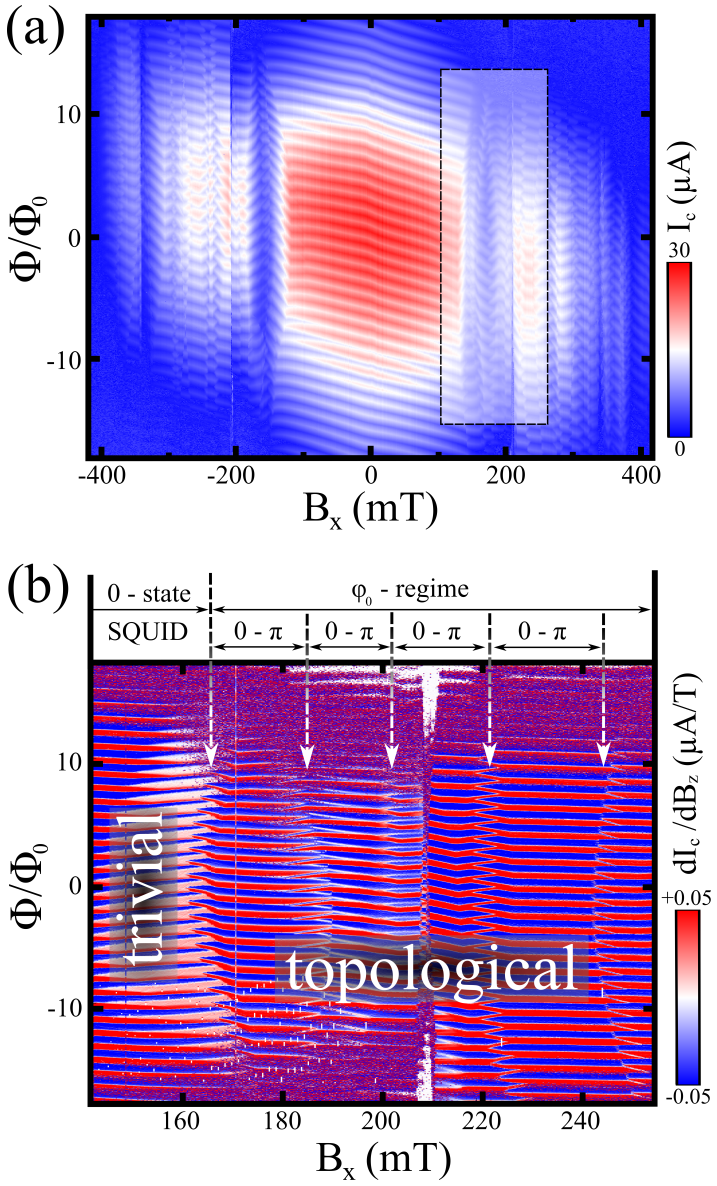

Figure 51: (a) Color contour map showing the critical current I_c in dependence of magnetic flux Φ and in-plane assisting fields B_x. For a critical in-plane field $B_x^{crit} = 165\,mT$ the SQUID enters the φ_0- regime, accompanied by π-transitions which happen periodically for $B_x^{0-\pi} \approx 20\,mT$. Interestingly, the critical current oscillates not only in SQUID geometry $I_c(\Phi)$, but also for $I_c(B_x)$ with the periodicity $\triangle B_x \approx 200\,mT$, which estimates an effective area $A_{eff} \approx 0.01\mu m^2$. (b) shows a SQUID sensitivity mapping dI_c/dB_z of the magnetic field window illustrated by the dashed rectangular in (a). The individual $0-\pi$ transitions are highlighted and arrows mark the single HIFQs. This individual transitions host topological superconducting states. The data is measured at $T = 500\,mK$.

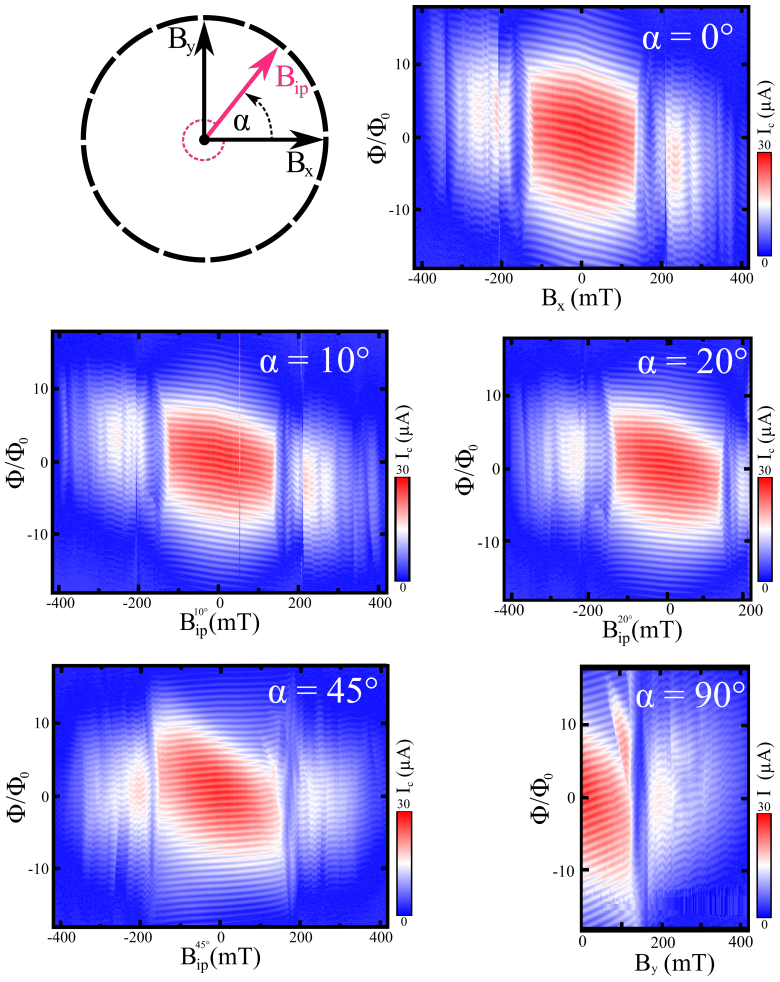

Figure 52: Color contour mappings of the SQUID's critical current I_c in dependence of magnetic flux Φ and in-plane assisting fields $B_{x,y}$ for several in-plane magnetic field angles α. Different modulation patterns for different α are observed. The data is measured at $T = 500\,mK$.

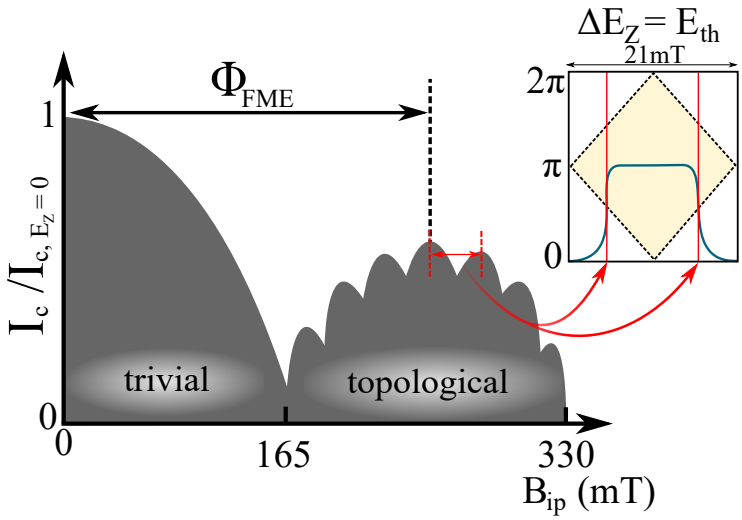

Figure 53: Illustration of the SQUIDs critical current I_c response as function of an in-plane magnetic field B_{ip}. The presentation shows the flux modulation and the $\triangle E_Z = E_{th}$ transitions, both giving rise to oscillations in the $I_c(B_{ip})$ pattern. The superconducting ground state of the device is trivial for $B < 165mT$. For larger fields the superconducting ground state is topologically non-trivial as indicated by the modulated oscillations in I_c with a periodicity of $\triangle B_x^{0-\pi} \approx 21\,mT$ due to $\triangle E_Z = E_{th}$.

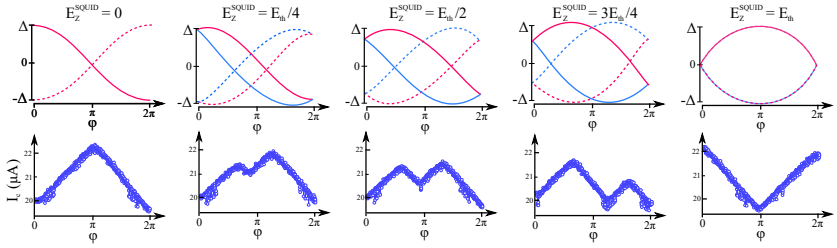

Figure 54: Gallery of the evolution of the ABS spectrum of the superconducting weak links for one interval of $\triangle E_Z = E_{th}$. The formation of a topological superconducting state manifests itself as minimum in the critical current I_c and with halfed periodicty in φ. The minimum in I_c and the $\varphi = \pi$ state are strong indicators for the presence of Majorana fermions.

Conclusion of the Superconducting TCI Thin Film Devices

In the scope of this thesis, superconducting devices - JJs & SQUIDs - based on sputtered TCI *SnTe* thin films have been successfully established. Transport experiments conducted on the samples show unconventional device characteristics with strong evidence of originating in the non-trivial topology of the *SnTe*. Among the auxiliary findings are the anomalous Fraunhofer patterns of JJs, saw-tooth CPRs, high SQUID inductance and large effective g-factors of the weak links. Strikingly, in-plane magnetic field measurements succeed in manifesting φ_0-SQUIDs with tunable $0-\pi$ transitions. The global phase control of the device confirms that these transitions enable controlled transitions between trivial and topological superconductivity, and thus Majorana fermions. These outcomes are desireable for possible technological applications in the field of memory storage[162] and fault-tolerant quantum computing[163]. Further, the data supports TCI thin film devices as an interesting new playground for fundamental research in the field of topological superconductivity and Majorana physics.

[162] Lindner and Robinson. *Nat. Phys.*, 11:307–315, 2015
[163] Moore. *Nature*, 464:194–198, 2010

Part IV

Results of the Bulk Superconducting Devices

Overview

Device applications require high quality samples in terms of crystallinity and interfaces. With state-of-the-art deposition techniques, thin films of topological ternary Heuslers are difficult to prepare and often lack the required quality because of defect formation. Single crystals do not suffer these restictions, but are limited in device design due to the bare surfaces often being too rough to form smooth interfaces. In the following chapter, we present a new and versatile method of combining high quality bulk ternary Heusler single crystals with the advantages of thin film deposition and device fabrication. Special focus is given to the all *in-situ* preparation to ensure excellent film interfaces. The feasibility of the procedure is demonstrated by fabricating SQUIDs out of bulk single crystals with advanced *focused ion beam* (FIB) techniques. This part begins with a demonstration of the preparation of *bulk-thin film hybrids,* followed by the individual FIB structuring of SQUIDs consisting of *S-c-S* and *S-I-S* weak links. Afterwards, the electrical transport measurements are given for both systems and results are discussed.

All in-situ Processing Technique

As described in the section *Topological Half-Heusler Alloys - YPtBi & LuPtBi* of PART I, the single crystals are grown by SHEKHAR ET AL. at the MAX-PLANCK-INSTITUTE FOR CHEMICAL PHYSICS AND SOLIDS. Despite having been polished, the $YPtBi$ and $LuPtBi$ single crystal pieces possess very rough surfaces even detectable by conventional optical microscopy. Such high roughness values and contaminated surfaces make it impossible to pattern intact insulating tunnel barriers with typical thicknesses between $1\,nm$ and $3\,nm$. To combat this issue, the single crystals are spanned into a micro vise and are placed in a vacuum chamber with base pressure $p \sim 10^{-8}\,mbar$. The sputtering system is depicted in *figure* $55(a)$ and a schematic illustration of the single crystal mounted in the micro-vise is given in *figure* $55(b)$. After reaching the required vacuum quality, the single crystals are cleaved by a blade mounted on top of the vise to ensure a smooth and clean surface structure. Immediatly after the cleavage, a $0.4\,nm$ $Al_{96}Si_4$ film is deposited via DC sputtering on top of the fresh single crystal surface without any vacuum break. To induce the oxidization of the Al the samples are left to rest in a controlled O_2 atmosphere for 30 minutes. This procedure is known to produce insulating Al_2O_3 barriers without oxidizing the underlaying material due to the excellent passivation of $Al\,/\,Al_2O_3$ interfaces[164]. The subsequent procedure

[164] Boeve et al. *J. Appl. Phys.*, 89(482), 2001

is repeated until the desired barrier thickness is reached. For the following *S-I-S* based SQUIDs the procedure is done three times, resulting in a thickness of roughly 1.2 nm $AlOx$. Following the oxidization steps, the samples are coated through DC sputtering with $1 - 1.5\mu m$ thick polycrystalline $Al_{96}Si_4$, a conventional s-wave superconductor frequently used to characterize spin-polarization in ferromagnets via MESERVEY-TEDROW tunneling spectroscopy[165]. Compared to pure Al, the $Al_{96}Si_4$ has a higher T_c ranging from 1.5 K to 3 K depending on the crystallinity, the Si-doping and the film thickness[166]. This procedure results in freshly cleaved topological materials, which are coated with a thin film barrier and an s-wave superconductor. The superconductors ($YPtBi/LuPtBi$ and $Al_{96}Si_4$) share different T_c's, which is necessary for tunneling spectroscopy experiments. The further shaping of the device hybrids is done in a FIB system (FEI *Helios NanoLab DualBeam*). The FIB processing for the *S-c-S* and *S-I-S* bulk SQUIDs is demonstrated individually in the following chapters.

[165] Meservey, Tedrow, and Fulde. *Phys. Rev. Lett.*, 25 (1270), 1970

[166] Chevrier et al. *Phys. Rev. B*, 36(9115), 1987

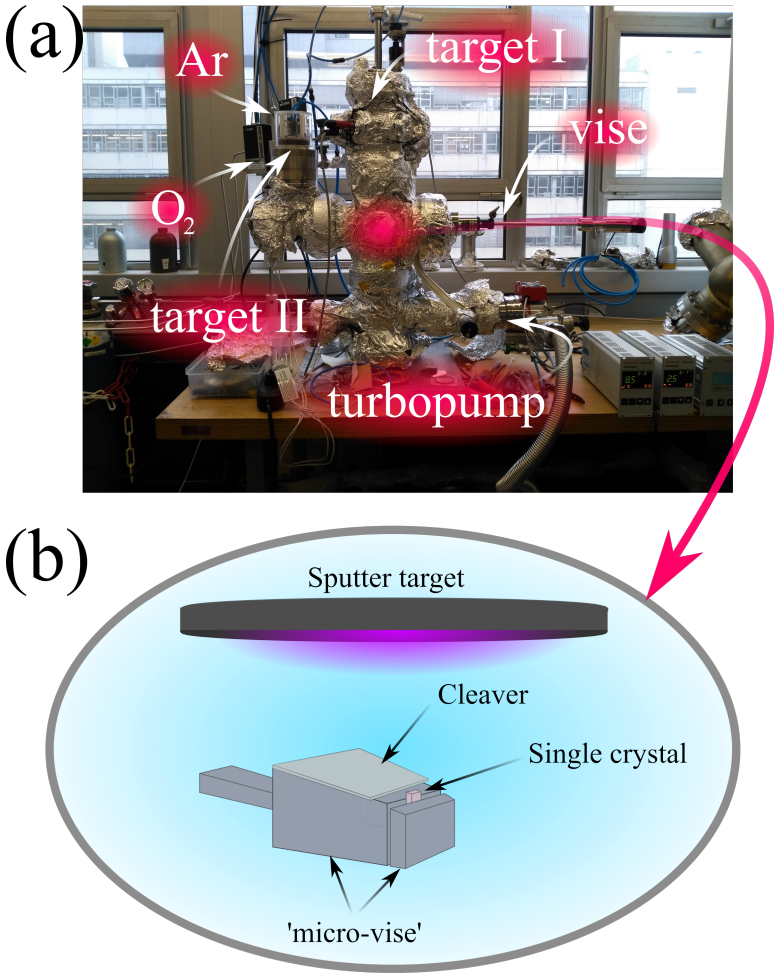

Figure 55: (a) Photograph of the processing setup. Technical details (target positions, gas valves etc.) are labeled. (b) Schematic illustration of the inner chamber, located at the red highlighted area in the photograph. It illustrates the principle of the all *in-situ* process. The single crystal piece is positioned in a micro vise. A mounted cleaver cuts the crystal along a given crystal direction. Directly after, the sputter process starts depositing thin films on the bare single crystalline surface. Following this recipe, the resulting bulk heterostructure surfaces are never exposed to air and device degradation is limited.

Processing of Superconducting Devices Solely Consisting of Superconducting Topological Insulator

In this section, the FIB processing of the SQUIDs consisting solely of superconducting topological insulator material is exemplified. The individual steps are illustrated in *figure* $56(a) - (h)$, from the bare single crystal piece in (a) to the defined constricted JJ in (h). In (a) a false color SEM image shows a single crystal piece (highlighted in pink) suitable for further processing. From the single crystal plateau in (a) a thin lamella with dimensions of $(2\,\mu m \times 15\,\mu m \times 5\,\mu m)$ is cut with a Ga^+-ion beam with $30\,keV$ particle beam energy. Prior to the beam etching, a Pt film (roughly $100\,nm$) is deposited on top of the target area via beam induced decomposition of precursor molecules to minimize the irradiation damage (the penetration length of Ga^+-ions is estimated to around $40\,nm$ in Pt). With a micromanipulator (*Omniprobe 100 - Oxford instruments*) the lamellas are freed and can be transferred to a target TEM grid holder. The lamella (illustrated in orange), fixed to the micromanipulator (highlighted in purple) with locally deposited Pt, is shown in *figure* $56(b)$. In (c) the freed single crystal fin (red), which is fixed to a TEM grid holder through Pt contacts, is shown. The deposited Pt is highlighted in beige. A smaller piece of the lamella is cut and transferred to a target Si wafer (blue) with Au contact pads (yellow), enabling 4W measurements in later device analytics. This step is shown in *figure* $56(d)$. The single crystal piece is fixed to each Au contact through local Pt deposition to guarantee good electrical contact. In *figure* $56(e)$ the single crystal is formed through a Ga^+ beam etching into SQUID geometry, before the *S-c-S* weak links are designed (shown in (f)). In (g) a top view of the completed topological bulk SQUID is shown and (h) provides a close-up view on one of the constricted

weak links. Following the patterning, the entire device is coated with roughly 250 nm SiO_2, deposited by FIB-cracked precursor molecules. The deposition is done from all sides and accessible angles to give uniform protection. This coating shields the device from direct exposure to air, which is known to heavily degrade compound systems consisting of transition metals, such as La, Y, Lu, by oxidization.

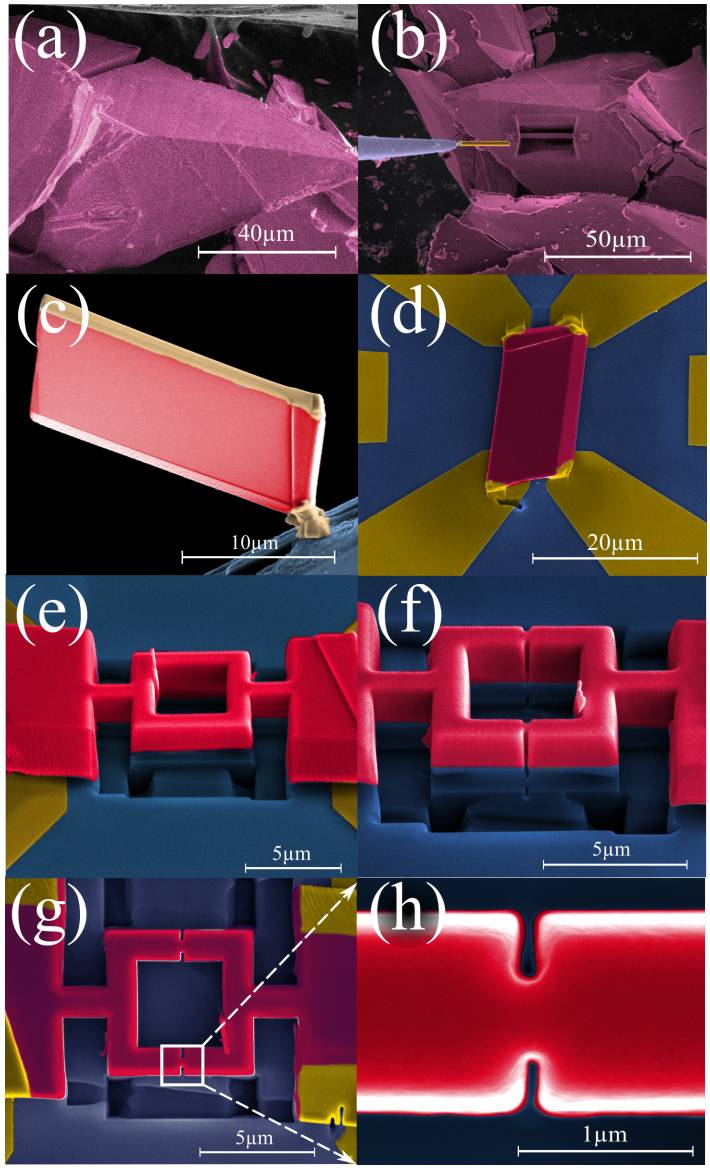

Figure 56: Series of false color SEM images illustrating the single FIB fabrication steps. (a) shows a processable single crystal piece (pink). (b) shows a freed single crystal lamella (orange), which is ready for transfer by the micromanipulator (light blue) to a TEM grid holder. There, the lamella is fixated for further processing (shown in (c)) and afterwards placed between the contact pads of the substrate ((d)). (e) demonstrates how the SQUID is cut out of the single crystal lamella and (f) illustrates the forming of the *S-c-S* weak links. (g) provides a top view of the finished single crystalline SQUID. (h) shows a close-up view of one of the *S-c-S* weak links.

Processing of Superconducting Topological Insulator - Barrier - Conventional Superconductor Hybrid Devices

In this section, the FIB processing of the superconducting topological insulator - barrier - conventional superconductor heterostructures is demonstrated. The overall procedure is similar to the one demonstrated in the previous section, *Processing of superconducting devices solely consisting of superconducting topological insulator,* so this part will concentrate only on the steps, which differ. In *figure 57(a),* the freed lamella consisting of the $YPtBi - AlOx - Al_{96}Si_4$ system (blue) is placed on a TEM grid (orange). The Pt shielding is marked in beige. Up to this step, the processing has been identical. Note that in this false color SEM image, no interface between the $YPtBi - Al_{96}Si_4$ is observable. The reason for this is that during the cutting of the lamella, ablated material of the single crystal is redeposited on all sides of the system stack. To restore sample quality, this redeposition film is removed through a cross section cleaning protocol. This polishing is done with Ga^+-ions at moderate currents ($80 - 150\,pA$, $1.5 - 3^\circ$ tilting angle) to peel off the redeposited material layer by layer. In *figure 57(b)* the lamella after cross section cleaning is shown. A clear heterostructure has been restored, as can be seen from the sharp interface contrast between the $Al_{96}Si_4$ film (blue) and the $YPtBi$ bulk crystal (pink). Smaller pieces of $2 - 5\,\mu m$ are sliced out of the lamella and glued to the micromanipulator, as demonstrated in *figure 57(c).* The systems are transferred to target Si wafers (grey) with pre-patterned Au contact leads (yellow) and placed between them as illustrated by *figure 57(d).* In order to prepare SQUID rings, quadratic holes are cut into the fins as illustrated in *figure 57(e).* The holes are cut directly into the interface region to allow $YPtBi - AlOx - Al_{96}Si_4$

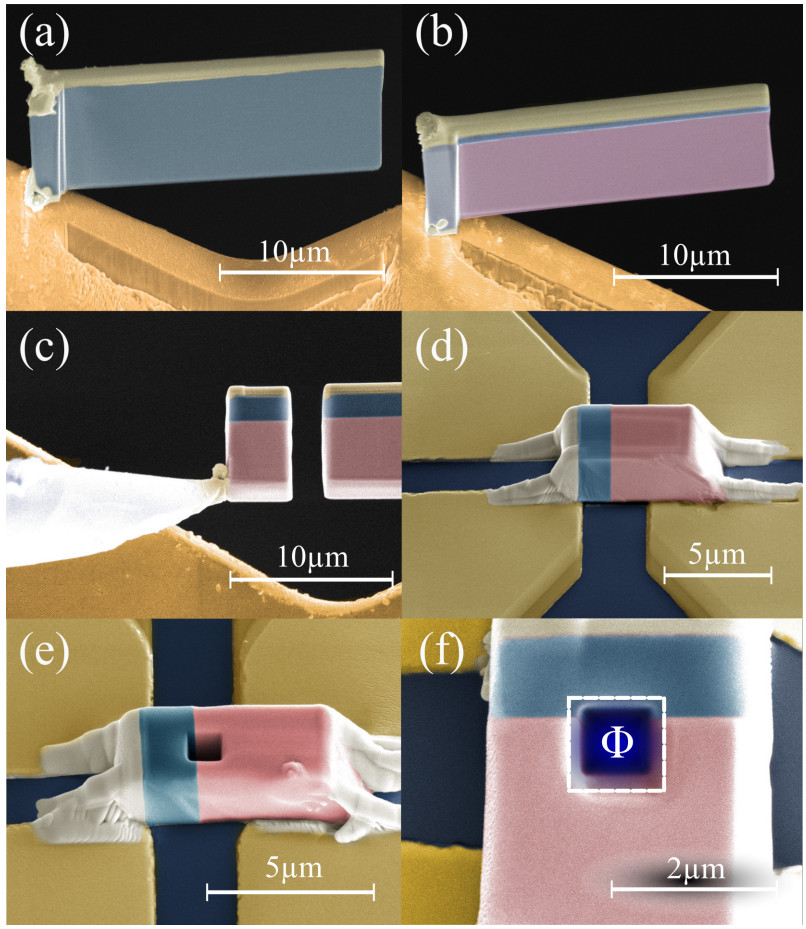

Figure 57: Gallery of false color SEM images illustrating those FIB fabrication steps differing from the ones for S-c-S SQUIDs. In (a), a freed lamella mounted onto a TEM grid holder (orange) is shown. No heterostructure is observed due to redeposited material on exposed surfaces during cutting process. (b) shows the lamella after cross section polishing. The redeposited material has been removed and a clear heterostructure is visible. The s-wave superconductor is highlighted in blue and the Heusler single crystal in pink. (c) smaller pieces are cut out of the lamella and are transfered with a micromanipulator (grey) to the target substrate and placed between contact leads (golden, shown in (d)). To form SQUIDs from the heterostacks, a rectangular hole is cut into the S-I-TSC interface (illustrated in (e)). (f) shows the prepared SQUID and the effective area of penetrating magnetic flux is highlighted.

junctions. The top view of a patterned heterojunction SQUIDs is given in *figure 57(f)* with a highlighted effective area for magnetic flux Φ threading. As described for the SQUID consisting entirely out of superconducting TI material, the device is coated with 250 *nm* SiO_2 to provide protection against degradation.

Transport Investigations of the Fabricated Single Crystalline SQUIDs

Investigations of the Micropatterned LuPtBi Bulk SQUIDs

This section discusses the electrical transport characterization of the SQUIDs consisting of *S-c-S* weak links. The SQUIDs are made entirely out of bulk *LuPtBi* and are measured in a *sionludi* cryostate setup at Institute Néel in Grenoble. Unless stated differently, all measurements in this section are carried out at a base temperature $T = 85\,mK$. At this temperature, the current-biased dV/dI characteristic of the device shown in *figure 56* is given in *figure 58*. The formation of a superconducting gap is clearly visible, but the inner gap resistance of the device does not result in a $dV/dI = 0\,\Omega$ state.

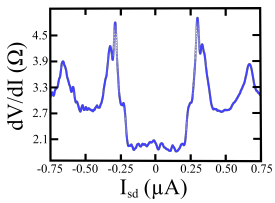

Figure 58: Current-biased differential resistance dV/dI measurement of a *LuPtBi* bulk SQUID. The superconducting gap as well as several Andreev peaks are visible, yet the inner gap device resistance of the system remains finite $dV/dI > 0\,\Omega$. Since a well defined superconducting state is lacking, a quantitative device analysis is difficult. The data is measured at $T = 85\,mK$.

This makes a quantitative device analysis difficult due to the lack of a well defined superconducting state. The cause for the finite resistance of the single crystal remains puzzeling. It is possible that the $250\,nm$ SiO_2 coating did not result in a homogenous film. A porous film structure could locally expose the *LuPtBi* surface to atmosphere. The resulting locally induced device oxidization might be responsible for the finite resistance of the bulk crystal. However, several interesting observations can be taken from this measurement. First, the gap transition shows a superconducting double-gap known for *multiband superconductors*, which has recently been predicted for superconducting half-Heusler compounds with present TSSs[167]. Second, Andreev peaks similar

[167] Brydon et al. *Phys. Rev. B*, 96(094526):1–16, 2017

to the ones observed for the TCI thin film samples occur. These states persist until up to comparably high out-of-plane magnetic fields B_z as demonstrated by the color-contour plot in *figure 59(a)*. The peaks are present up to $B_z = 600\,mT$. On closer inspection, weak SQUID oscillations can be observed for small bias currents $I_{sd} \leq \pm 250\,nA$ and small B_z. The colour-contour plot of *figure 59(b)* better resolves this regime and the I_c oscillations are indeed visible. The estimated periodicity is $\triangle B_z = 4.5\,mT$. This gives an effective area of penetrating flux $A_{eff} \backsimeq 0.46 \mu m^2$. Compared to the SQUID area of the *LuPtBi* SQUID demonstrated in *figure 56(g)*, this is far too small and can not be attributed to the SQUID response of the device. Considering the other device dimensions taken from the SEM image, i.e. width W, length L and thickness t, does not result in reasonable agreement with the measured data either. Hence, the origin of such oscillations has to remain a mystery and one has to come to the conclusion, that, because of the finite device resistance and unidentified I_c oscillations, the micropatterned *S-c-S* SQUIDs do not allow for further quantitative statements.

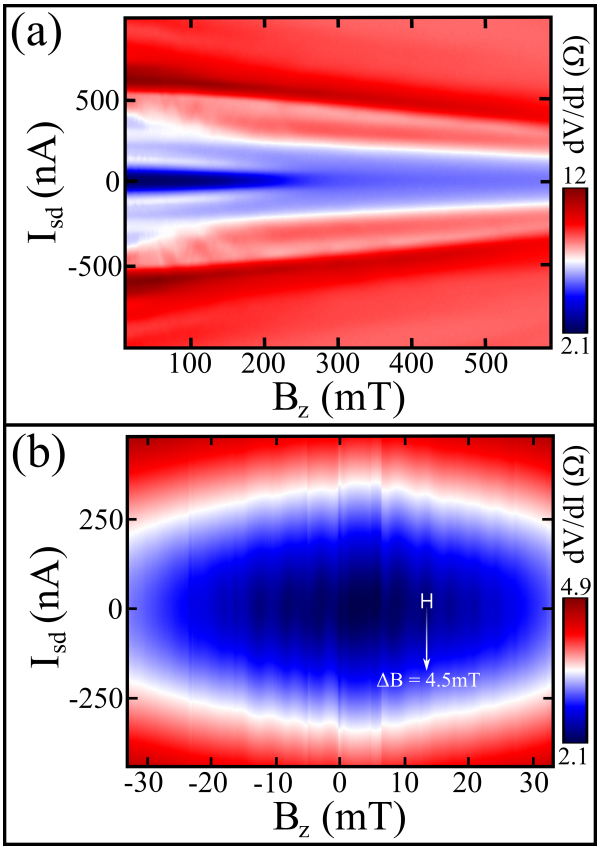

Figure 59: (a) shows the $LuPtBi$ single crystalline bulk SQUID response in dependence of the biased current I_{sd} up to comparably large magnetic fields B_z. For small currents and magnetic fields, weak oscillations are observed. (b) shows a finer magnetic field scan to resolve the critical current oscillations. The periodicity $\triangle B_z = 4.5\,mT$ yields an effective area $A_{eff} = h/(2e\triangle B_z) = 0.46\mu m^2$, which does not match the fabricated SQUID dimensions. The data is measured at $T = 85\,mK$.

Investigations of the Micropatterned YPtBi Bulk Heterostructure SQUIDs

This section discusses the electrical transport characterization of the SQUIDs consisting of *S-I-S* weak links. Unless stated otherwise, all data taken from these devices is measured at a base temperature $T = 85\,mK$. *Figure 60* displays a current-biased dV/dI measurement. The image shows a clear double-gap structure resulting from the two different T_c's of $YPtBi$ and $Al_{96}Si_4$. However, as for the *S-c-S* bulk SQUIDs, the heterosystems show finite resistance $dV/dI > 0\,\Omega$, making quantitative diagnostic difficult. Since both device series share the finite resistance problem, device degradation due to oxidization is a likely explanation.

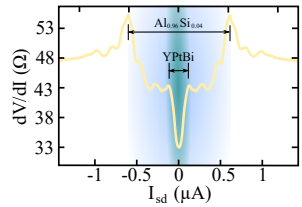

Figure 60: Current-biased differential resistance dV/dI measurement of a $YPtBi - AlOx - Al_{96}Si_4$ junction SQUID. Two distinct superconducting gaps are measured, matching the different critical temperatures of both superconductors. However, the overall device resistance remains finite $dV/dI > 0\,\Omega$. The data is measured at $T = 85\,mK$.

Compared to the $LuPtBi$ bulk SQUIDs, the $YPtBi - AlOx - Al_{96}Si_4$ SQUIDs show a stronger response to applied magnetic fields, as shown in *figure 61(a)*. The $I_c\,(B_z)$ oscillations appear to be of irregluar width $\triangle B_z$. Some oscillation periodicities match the fabricated SQUID area, but the irregularities suggest flux-trapping in the device as a more plausible explanation of the change in I_c. Interestingly, overmodulated I_c oscillations with periodicity $\triangle B_z = 180\,mT$ can be observed. The data is presented in *figure 61(b)*. As for the other bulk SQUIDs, no combination of the device dimenions W, L and t results in considerable data agreement. The response of the SQUID to in-plane magnetic field B_y gives the possibility to better resolve the $I_c\,(B)$ pattern at expense of quantitative validity. The resulting pattern is shown in *figure 61(c)*. Clear I_c oscillations are observable and show irregular dependence, suggesting a scenario of different superconducting phase modulations. Such effects have been predicted for devices consisting of topological superconductors[168]. But the absence of a

[168] Karnaukhov. *Sci. Rep.*, 7 (7124), 2017

well-defined superconducting state prevents further inferences or analysis of the SQUID behavior. Therefore, the devices can merely support superconducting topological half-Heusler materials as an interesting field of study for potential new physics, but are unable to give solid quantitative data.

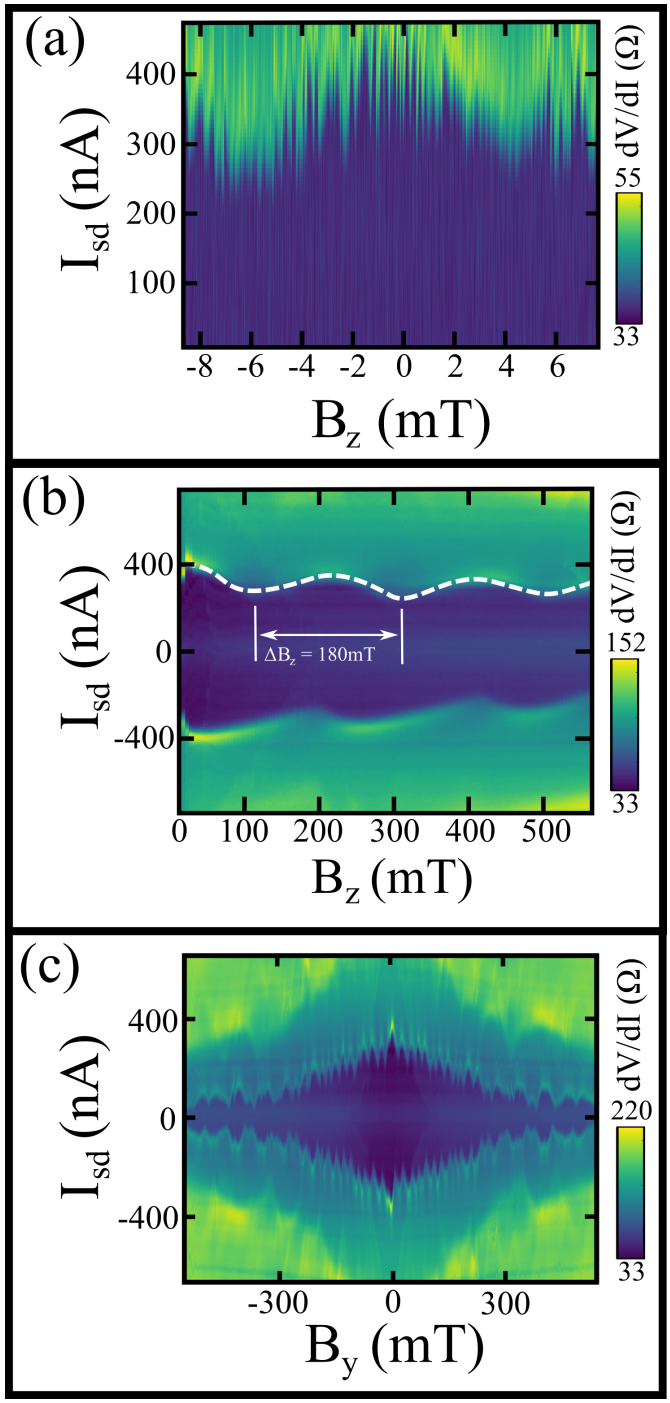

Figure 61: (a) shows the SQUID response in dependence of the magnetic field B_z and the bias current I_{sd}. Clear oscillations in the critical current are visible. (b) shows the SQUID characteristics for larger B_z. Modulated onto the small oscillations illustrated in (a) are further oscillations of periodicity $\triangle B_z = 180\,mT$. (c) shows the SQUID response for in-plane magnetic field B_y, allowing a better resolved oscillation pattern at the expense of analyzability. The data is measured at $T = 85\,mK$.

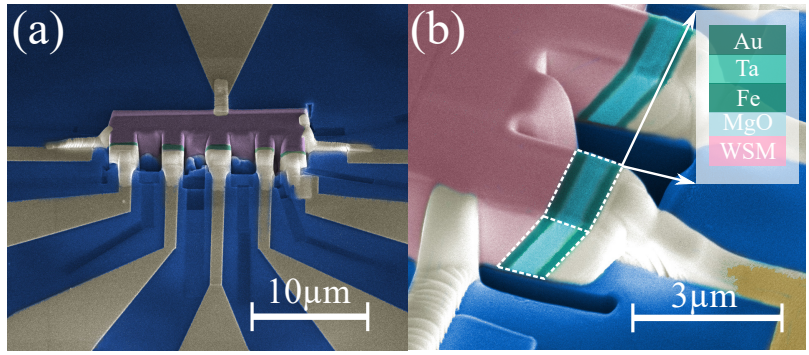

Figure 62: (a) To demonstrate the versatility of the FIB microfabrication approach, an exemplary false color SEM image showing a tunnel junction system with bulk single crystal back electrodes is given. (b) shows a close-up view of one of the tunnel stacks of the sample, consisting of a Weyl semimetal (WSM, pink) back electrode, a thin *MgO* barrier and a *Fe/Ta/Au* top electrode (light and dark teal).

Concluding Remarks to the Single Crystalline Bulk Samples

Even if the bulk single crystalline bulk SQUIDs ended up not showing the anticipated results, the main focus of this chapter was a demonstration of the versatility and feasibility of the novel *top-down* microprocessing approach. The developed technique is not restricted to superconducting materials or Josephson devices. In order to tackle other issues in the field of topological matter and condensed matter physics, different device architectures can be patterned with the technique, e.g. magnetic tunnel junctions consisting of topological Weyl semimetal bulk back electrodes and magnetic thin film top electrodes. A false color SEM image of such a fabricated system is exemplarily shown in *figure 62(a) - (b)*. The experimental investigation of these devices is omitted at this point, as it would be clearly beyond the scope of this thesis. Therefore, it shall demonstrate solely that the FIB microfabrication technique may open a door to new experimental access to functional bulk devices.

CONCLUSION AND OUTLOOK

In this last chapter, the results obtained in the framework of this thesis are summarized. A few specific points are emphasized and further possible approaches for research in the corresponding field of study are encouraged.

In this thesis, we succeeded in growing topological crystalline thin films via co-sputtering techniques. Growing high-quality thin films through sputtering is important to the technological integration of materials, as it should pave the way for a cheaper, easier and more cost efficient commercial utilization thereof. In particular, the moderate growth conditions (room temperature to $T = 150°C$) are, from the technological point of view, desireable. To our knowledge, no other research team has successfully deployed this deposition technique for growing TCI thin films at the point of writing, and only one other group published results demonstrating successfully sputtered 3D TI thin films of comparable quality[169]. Due to the low roughness of the $SnTe$ thin films, another appealing approach is their integration as bottom electrodes in mesoscopic tunnel devices. This enables the investigation of electronic transport in vertical direction, which is of great interest for future integration in existing architectures. Furthermore, tunnel devices allow the testing of the tunnel magnetoresistive response to an upper ferromagnet electrode[170] and inelastic

[169] Wang et al. *Sci. Rep.*, 6 (25291), 2016

[170] Götte et al. *Phys. Rev. Appl*, 2(054010):1–12, 2014

electron tunnel spectroscopy could be utilized as additional experimental method for testing TSSs[171]. Just replacing the upper ferromagnetic electrode with a superconducting one allows for analysis the transport in a MESERVEY-TEDROW[172] manner, which might be interesting to investigate due to spin-polarized tunneling originating from TSSs.

A second major achievement within this work is the patterning of fully operational Josephson junctions and SQUIDs out of *SnTe/Nb* and *SnTe/Ta* hybrid film systems. The devices demonstrate magnetic field-controllable $0-\pi$ transitions and strongly hint at the presence of topological superconductivity and Majorana fermions. All three properties are highly desirable for potential spintronic and quantum computing applications. Here, further investigations of superconducting devices based on other topological materials, i.e. Dirac materials[173] and Weyl semimetals[174], are of interest as the results would significantly foster current discussion in the field of topological superconductivity. The recipe for sample design, the methods used for analysis and further collaborations required to tackle this problem have been established in the course of this thesis.

A further aim of this doctoral thesis was the development of a new all *in-situ* structuring recipe for fabricating microscopic devices out of macroscopically sized single crystals using FIB techniques. This is of interest for general solid state research as thin films often lack the required quality, whereas high-quality bulk single crystals are often restricted in terms of electronic transport analysis. The structuring method applied here is a promising alternative. It is not limited to designing Josephson junctions and SQUIDs, but can easily adapted to fit other device layouts, i.a. tunnel junctions.

[171] Cascales et al. *Appl. Phys. Lett.*, 107(252402):1–4, 2015

[172] Meservey and Tedrow. *Low Temp. Phys.*, 13:pp. 405–409, 1974

[173] Yu et al. *arXiv preprint*, arXiv:1801.04365v1:1–25, January 2018

[174] Khanna et al. *Phys. Rev. B*, 95(201115), 2017

However, the role of topological materials in solid state physics is evolving at such rapid speed that predictions are quite difficult to make. What can be said with certainty is that topological physics will lead to big "breakthroughs" in fundamental research within the next decade. To mirror the introduction, this thesis closes with a quote from Kafka:

"Der Gedanke einmal in seiner Größe gefasst, kann nicht mehr verschwinden; solange es Menschen gibt wird auch der starke Wunsch da sein, den Turm zu Ende zu bauen."

In this context, I think topological materials will have a huge impact on the research and technology of the future and I hope the work in this thesis may provide a modest contribution.

Bibliography

Akiyama et al. *J. Phys. Conf. Ser.*, 468(052001):1–5, 2014.

Akiyama et al. *Nano Res.*, 9(2):pp. 490–498, 2016.

Ando. *J. Phys. Soc. Jpn.*, 82(10200):1–32, 2013.

Ando and Fu. *Annual Reviews of Condensed Matter Physics*, 6:361–381, 2015.

Ariad and Grosfeld. *Phys. Rev. B*, 95(161401):1–5, 2017.

Arutyunov et al. *Sci. Rep.*, 2012.

Assaf et al. *Appl. Phys. Lett.*, 105(102108), 2014.

Assaf et al. *Sci. Rep.*, 6(20323), 2016.

Bakurskiy et al. *Appl. Phys. Lett.*, 108(042602):1–5, 2016.

Bao et al. *Sci. Rep.*, 2(726), 2012.

Bardeen, Cooper, and Schrieffer. *Phys. Rev.*, 108:1175–1204, 1957.

Beenaker. *Annual Reviews of Condensed Matter Physics*, 4:113 – 136, 2013.

Beenaker et al. *Phys. Rev. Lett.*, 110(017003), 2003.

Beenaker et al. *Phys. Rev. Lett.*, 110(017003), 2013.

Bergmann. *Phys. Rep.*, 107(1), 1984.

Bernevig and Zhang. *Phys. Rev. Lett.*, 96(106802), 2006.

Bernevig et al. *Science*, 314(1757), 2006.

Bernick and Kleinman. *Solid State Commun.*, 8:569–575, 1970.

S. Blügel, Y. Mokrousov, T. Schäpers, and Y. Ando, editors. *Topological Matter - Topological Insulators, Skyrmions and Majoranas*, volume 139 of *Schriften des Forschungszentrum Jülich - Reihe Schlüsseltechnologien*, 2017. Forschungszentrum Jülich GmbH.

Bocquillon et al. *Nat. Nanotechnol.*, 12:137–143, 2017.

Boeve et al. *J. Appl. Phys.*, 89(482), 2001.

Brennan et al. *Appl. Phys. Lett.*, 101(211604), 2012.

Bruno et al. *Physics Procedia*, 36:239–244, 2012.

Brydon et al. *Phys. Rev. Lett.*, 116(177001):1–5, 2016.

Brydon et al. *Phys. Rev. B*, 96(094526):1–16, 2017.

Butch et al. *Phys. Rev. B*, 84(220504):pp. 1–5, 2011.

Cascales et al. *Appl. Phys. Lett.*, 107(252402):1–4, 2015.

Chadov et al. *Nat. Mater.*, 9:541–545, 2010.

Chang et al. *Science*, 340:167–170, 2013.

Chen et al. *arXiv preprint*, arXiv:1801.08504v1:1–22, 2018.

Chevrier et al. *Phys. Rev. B*, 36(9115), 1987.

Chiodi et al. *Phys. Rev. B*, 86(064510), 2012.

Chiu and Schnyder. *Phys. Rev. B*, 90(205136):1–26, 2014.

Clarke et al. *SQUID Sensors: Fundamentals, Fabrication and Applications*, volume 329 of *Series E: Applied Sciences*. Kluwer Academic Publishers, 1996.

Colwell. *Hot Chips Symposium*, 25(16035983), August 2013.

Cox et al. *Nanofabrication*, 1:53–64, 2014.

Dankert et al. *Nano Lett.*, 15:7976–7981, 2015.

Das-Sarma et al. *npj Quantum Inf.*, 1(15001), 2015.

Dimitrova and Feigel'man. *Phys. Rev. B*, 76:014522, 2007.

Donnier-Valentin and Wernsdorfer. *Research Highlights Institute Néel*, 6, 2012.

D'yakonov and Perel. *JETP Lett.*, 13:467, 1971.

Eilenberger. *Z. Phys.*, 214:195–213, 1968.

Faggin et al. *IEEE Micro*, 16(6):10–20, 1996.

Fan et al. *Nat. Mater.*, 13:699–704, 2014.

Faucher et al. *Physica C*, 368:211–217, 2002.

Finck et al. *Phys. Rev. X*, 4(041022):1–9, 2014.

Fu and Kane. *Phys. Rev. Lett.*, 100(096407), 2008.

Fu, Kane, and Mele. *Phys. Rev. Lett.*, 98(106803):pp. 1–4, 2007.

Fulde and Ferrell. *Phys. Rev.*, 135:A550–A564, 1964.

Galetti et al. *Phys. Rev. B*, 89(134512), 2014.

Gerstenberg and Hall. *J. Electrochem. Soc.*, 111(8):936–942, 1964.

Ginzburg and Landau. *Zh. Teor. Fiz.*, 20:1064–1082, 1950. [english translation].

Gor'kov. *Sov. Phys. JETP*, 7:505–508, 1958.

Goswami et al. *Nat. Nanotechnol.*, 11:861–865, 2016.

Götte et al. *Phys. Rev. Appl*, 2(054010):1–12, 2014.

Götte et al. *Sci. Rep.*, 6(36070):1–9, 2016.

Guo and Chen. *arXiv preprint*, arXiv:1710.07169v1, October 2017 2017.

Hart et al. *Nat. Phys.*, 13:87–93, 2017.

Hasan and Kane. *Rev. Mod. Phys.*, 82(3045):3045 – 3067, 2010.

Hasan et al. *Phys. Scr.*, T164(014001):1 – 22, 2015.

Hashimoto et al. *Supercond. Sci. Technol.*, 27(104002):1–9, 2014.

Hashimoto et al. *Phys. Rev. B*, 92(174527):1–8, 2015.

Hayasaka and Fuseya. *J. Phys.: Condens. Matter*, 28(31LT01):1–5, 2016.

He et al. *Phys. Rev. Lett.*, 106(16)(166805):1–5, 2011.

Heikkilä et al. *Phys. Rev. B*, 66(184513), 2002.

Hikami, Larkin, and Nagaoka. *Progress in Theoretical Physics*, 63 (2):pp. 707–710, 1980.

Hou et al. *Phys. Rev. B*, 92(235134):1–9, 2015.

Hsieh et al. *Nat. Commun.*, 3(982):1–6, 2012.

Huang et al. *Phys. Rev. X*, 5(031023):1–9, 2015.

Iizumi et al. *J. Phys. Soc. Jpn.*, 38:443–449, 1975.

Josephson. *Phys. Lett.*, 1:251–253, 1962.

Josephson. *Adv. Phys.*, 14(56):419–451, 1965.

Kallaher et al. *Phys. Rev. B*, 79(075322), 2009.

Kane and Mele. *Phys. Rev. Lett.*, 95(146802), 2005.

Karnaukhov. *Sci. Rep.*, 7(7124), 2017.

Kato et al. *Science*, 306(1910), 2004.

Khan et al. *J. Appl. Phys.*, 105(083723):1–5, 2009.

Khanna et al. *Phys. Rev. B*, 95(201115), 2017.

Kieler et al. *Supercond. Sci. Technol.*, 20:318–322, 2007.

König et al. *Science*, 318(766), 2007.

Kodama et al. *J. Appl. Phys.*, 54(7):4050–4053, 1983.

Kou et al. *Solid State Commun.*, 10:1–20, 2014.

Kresin. *Phys. Rev. B*, 34(7587), 1986.

Kronenberg et al. *Phys. Rev. B*, 94(161108):1–5, 2016.

S. Kruchinin, H. Nagao, and S. Aono. *Modern Aspects of Superconductivity*. Number 978-981-4261-60-9. World Scientific Publishing Co. Pte. Ltd., first edition, 2011.

Kurter et al. *Nat. Commun.*, 6(7130):1–6, 2015.

Larkin and Ovchinnikov. *Sov. Phys. JETP*, 20:762–769, 1965.

Lee et al. *Phys. Rev. Lett.*, 113(197001):1–5, 2014a.

Lee et al. *Nano Lett.*, 14:5029–5034, 2014b.

Li et al. *Nat. Nanotechnol.*, 9:218–224, 2014.

Li et al. *arXiv preprint*, arXiv:1707.03154v1, 2017.

Liang et al. *Nat. Mater.*, 14:280–284, 2015.

Likharev. *Rev. Mod. Phys.*, 51(101), 1979.

Lin et al. *Nat. Mater.*, 9:546–549, 2010.

Linder et al. *Phys. Rev. Lett.*, 104(067001):1–4, 2010.

Lindner and Robinson. *Nat. Phys.*, 11:307–315, 2015.

Liu et al. *IEEE Trans. Appl. Supercond.*, 19(3):245–248, 2009.

Loder et al. *J. Phys.: Condens. Matter*, 25:362201, 2013.

Loder et al. *Sci. Rep.*, 5:15302, 2015.

Lu et al. *Phys. Rev. B*, 94(014504):1–9, 2016.

Maier et al. *Phys. Scr.*, T164(014002):5–8, 2015.

Marmorkos et al. *Phys. Rev. B*, 48(4):2811–2814, 1993.

McCumber. *J. Appl. Phys.*, 39(3113), 1968.

Meinert. *Phys. Rev. Lett.*, 116(137001):1–5, 2016.

Mengui et al. *Braz. J. Phys.*, 36(A2):pp. 324–327, 2006.

Meservey and Tedrow. *J. Appl. Phys.*, 40(2028), 1969.

Meservey and Tedrow. *Low Temp. Phys.*, 13:pp. 405–409, 1974.

Meservey, Tedrow, and Fulde. *Phys. Rev. Lett.*, 25(1270), 1970.

Mizuno and Aomine. *Jpn. J. Appl. Phys.*, 26:1607–1608, 1987.

Molenaar et al. *Supercond. Sci. Technol.*, 27(104003):1–6, 2014.

Moore. *Electronics Magazine*, 38(8), April 1965.

Moore. *Nature*, 464:194–198, 2010.

Mourik et al. *Science*, 336(6084):1003–1007, 2012.

Murani et al. *Nat. Commun.*, 8(15941), 2017.

Murphy et al. *Phys. Rev. B*, 96(094507), 2017.

Mutjaba. "intel xeon e5-2600 v3 and server processors unleashed for high-performance computing". Technical report, wccftech.com, September 2014.

Nanda et al. *Nano Lett*, 17(6):3396–3401, 2017.

Oostinga et al. *Phys. Rev. X*, 3(021007):1–7, 2013.

Ortmann, Roche, and Valenzuela, editors. *Topological Insulators - Fundamentals and Perspectives*. Wiley-VCG Verlag GmbH & Co., 2015.

Park et al. *Phys Rev B*, 96:064518, 2017.

Peng et al. *Phys. Rev. B*, 94(085409):1–22, 2016.

Pientka et al. *Phys. Rev. X*, 7(021032), 2017.

Puurunen. *J. Appl. Phys.*, 97(121301), 2005.

Qi and Zhang. *Rev. Mod. Phys.*, 83(1057):1057 – 1110, 2011.

Qu et al. *Sci. Rep.*, 2(339):1–5, 2012.

Qu et al. *Nat. Commun.*, 4:2710, 2013.

Radovan et al. *Nature*, 425:51–55, 2003.

Roulleau et al. *Phys. Rev. B*, 81(155449), 2008.

Sato and Ando. *Rep. Prog. Phys.*, 80(076501):1–42, 2017.

Sato and Saitoh. *Spintronics for Next Generation Innovative Devices*. Wiley-VCG Verlag GmbH & Co., 2015.

Savage. "a new spin on computing". Technical report, MIT Technology Review, August 2006.

Schuler. *Transport properties and defects in polycrystalline $CuGaSe_2$ thin films and heterostructures*. Phd thesis, FU Berlin, 2002.

Sessi et al. *Science*, 354(6317):1269 – 1273, 2016.

She et al. *Phys. Rev. Lett.*, 110(026802):1–5, 2013.

Shekhar et al. *Nat. Phys.*, 11:645–649, 2015a.

Shekhar et al. *arXiv preprint*, arXiv:1502.00604v2, 2015b.

Shen et al. *Nano Lett.*, 15(6):pp. 3827–3832, 2015.

Sigrist and Ueda. *Rev. Mod. Phys.*, 63:239–308, 1991.

Simonite. "intel puts the brakes on moore's law". Technical report, MIT Technology Review, March 2016.

Sist et al. *IUCrJ*, 3(5):377–388, 2016.

Skocpol et al. *J. Appl. Phys.*, 45(4045), 1974.

Skuse. "the trouble with quantum computing". Technical report, E&T .- Engineering and Technology, November 2016.

Snelder et al. *Supercond. Sci. Technol.*, 27(104001):7pp., 2014.

Snyder et al. *arXiv preprint*, arXiv:1710.06077v2:1–5, November 2017.

Sochnikov et al. *Phys. Rev. Lett.*, 114(066801):1–6, 2015.

Soloviev et al. *Beilstein J. Nanotechnol.*, 8:2689–2710, 2017.

Song et al. *Phys. Rev. B*, 93(195302):1–8, 2016.

Stewart. *Appl. Phys. Lett.*, 12(277), 1968.

Suominen et al. *Phys. Rev. B*, 95(035307):1–11, 2017.

Tafti et al. *Phys. Rev. B*, 84(184504):pp. 1–5, 2013.

Tanaka et al. *Phys. Rev. Lett.*, 105(097002):1–4, 2010.

Tanaka et al. *Nat. Phys.*, 8:800–803, 2012.

Theuerer and Hauser. *J. Appl. Phys.*, 35:554–555, 1964.

Thouless et al. *Phys. Rev. Lett.*, 49(405), 1982.

M. Tinkham. *Introduction to Superconductivity*. Number 978-0-486-43503-9. Dover Publications, second edition, 2004.

Tkachov et al. *Phys. Rev. B*, 92(045408):1–7, 2015a.

Tkachov et al. *Phys. Rev. B*, 92(045408):1–7, 2015b.

Usadel. *Phys Rev.Lett.*, 25:507–509, 1970.

Veldhorst et al. *Nat. Mater.*, 11:417–421, 2012.

Visani et al. *Nat. Phys.*, 8:539–543, 2012.

von Klitzing et al. *Phys. Rev. Lett.*, 45(494), 1980.

Waldrop. *Nature*, 530:144–147, 2016.

Wan et al. *Nat. Commun.*, 6(7426):1–5, 2015.

Wand et al. *Nano Res.*, 3(12):874–880, 2010.

Wang et al. *Sci. Rep.*, 3(2181):pp. 1–7, 2013.

Wang et al. *Sci. Rep.*, 6(25291), 2016.

Wang et al. *Nat. Commun.*, 8(366), 2017.

Weng et al. *MRS Bull.*, 39(10):pp. 849–858, 2014.

Wiedenmann et al. *Nat. Commun.*, 7(10303), 2016.

Wilczek. *Nat. Phys.*, 5:614–618, 2009.

Williams et al. *Phys. Rev. Lett.*, 109(056803):1–5, 2012.

Wollmann et al. *Phys. Rev. Lett.*, 71(2134), 1993.

Wu et al. *Phys. Rev. Lett.*, 98(136801):1–6, 2007.

Xiong et al. *Science*, 350(6259):413–416, 2015.

Xu et al. *Nat. Phys.*, 10:943–950, 2014a.

Xu et al. *Sci. Rep.*, 4(5709):pp. 1–7, 2014b.

Xu et al. *Science*, 347(6219):294–298, 2015a.

Xu et al. *Phys. Rev. Lett.*, 114(1):017001, 2015b.

Yamakage et al. *Phys. Rev. B*, 85(180509):1–5, 2012.

Yang et al. *Phys. Rev. B*, 94(075304):1–10, 2016.

Yoshida et al. *Phys. Rev. B*, 86:134514, 2012.

Yoshimi et al. *Nat. Mater.*, 13:253–257, 2014.

Yu and Cardona. *Fundamentals of Semiconductors - Physics and Materials Properties*. Number 978-3-642-00709-5. Springer-Verlag Berlin Heidelberg, fourth edition, 2010.

Yu et al. *arXiv preprint*, arXiv:1801.04365v1:1–25, January 2018.

Zeljkovic et al. *Nat. Phys.*, 10:572–577, 2014.

Zhang and Yi. *Nat. Commun.*, 4:2711, 2013.

Zhang et al. *Nat. Phys.*, 5:438–442, 2009.

Zhao et al. *Sci. Rep.*, 6(22377), 2016.

Zheng et al. *Sci. Rep.*, 4(6535), 2014.

Scientific Contribution

List of Publications

† Klett et al., *Proximity induced superconductivity and quantum oscillations in topological crystalline insulator SnTe thin films*, Nano Letters 18(2), pp 1264-1268, 2018

† Manos, Klett et al., *Tunneling magnetoresistance of perpendicular CoFeB-based junctions with exchange bias*, Journal of Applied Physics 122(103904), 2017

† Beyer, Klett, et al., *Imaging of carbon nanomembranes with helium ion microscopy*, Beilstein Journal of Nanotechnology 6(1):1712-1720, 2015

List of other contributions

† DPG Spring Conference 2015, *"Focused ion beam structured topological matter: A new and versatile method to fabricate high quality devices consisting of topological insulators"*, Poster, Berlin, *March 2015*

† SPP1666 "Topological Insulator" DFG Meeting 2015, *"Implementation of topological matter as tunnel backelectrodes into devices"*, Poster, Bad Sooden - Allendorf, *September 2015*

† Invited Talk - Centre National de la Recherche Scientifique Alpes, *"Hunting Majoranas: FIB structured superconducting quantum inference devices out of topological insulator single crystals"*, Talk, Grenoble, *December 2015*

† DPG Spring Conference 2016, *"FIB structured superconducting quantum interference devices out of topological insulator single crystals"* , Talk, Regensburg, *March 2016*

† SPP1666 "Topological Insulator" DFG Meeting 2016, *"Proximity induced superconductivity and quantum interference in topological crystalline insulator SnTe devices"*, Poster, Frankfurt, *October 2016*

† Spin Mechanics IV, *"Proximity induced superconductivity and quantum interference in topological crystalline insulator SnTe devices"*, Poster, Lake Louise, *February 2017*

† DPG Spring Conference 2017, *"Proximity induced superconductivity and quantum interference in topological crystalline insulator SnTe devices"*, Talk, Dresden, *March 2017*

† Invited Talk - Karlsruhe Institute of Technology, *"Proximity induced superconductivity and quantum interference in topological crystalline insulator SnTe devices"*, Talk, Karlsruhe, *July 2017*

† Young Scientist Meeting SPP1666 "Topological Insulators", *"Inelastic electron tunneling spectroscopy at tunnel junctions with integrated topological electrodes"*, Talk, Detmold, *September 2017*

List of abbreveations

ABS	Andreev Bound State
AR	Andreev Reflection
BCS	Bardeen-Cooper-Shrieffer
BZ	Brillouin zone
CB	Conduction band
COMM	Center-of-mass momentum
CP	Cooper pair
CPR	Current-phase relation
FFLO	Fulde-Ferrell-Larkin-Ovchinnikov
FIB	Focused Ion Beam
FME	Flux modulation effect
HLN	Hikami-Larkin-Nagaoka
HIFQ	Half-integer flux quantum
IFQ	Integer flux quantum
JJ	Josephson junction
MBS	Majorana bound state

MC	Magnetoconductivity
MR	Magnetoresistance
QHE	Quantum Hall effect
QSHE	Quantum spin Hall effect
RSS	Rashba spin splitting
RCSJ	Resistively and capacitatively shunted junction
S	Superconductor
SHE	Spin Hall effect
SIA	Structural inversion asymmetry
SML	Spin-momentum locking
SOC	Spin-orbit coupling
SQUID	Superconducting quantum interference device
STI	Strong topological insulator
S-c-S	Superconductor - constriction - superconductor
S-I-S	Superconductor - insulator - superconductor
S-N-S	Superconductor - normal conductor - superconductor
TCI	Topological crystalline insulator
TI	Topological insulator
TKNN	Thouless, Kohomoto, Nightingale, den Nijs
TSM	Topological semimetal
TSS	Topological surface state

VB	Valence band
WAL	Weak antilocalization
WTI	Weak topological insulator

Acknowledgements

- Danksagung

Das Ende meiner Dissertation ist allen gewidmet, die mich durch die letzten Jahre begleitet und geführt haben - Ihr Alle verdient meinen Dank und noch viel mehr! Ohne euch wäre vieles schwerer, wenn nicht gar unmöglich geworden. Besonders Prof. Dr. Günter Reiss möchte ich danken für die Option in einem so aufregenden Thema der aktuellen experimentellen Festkörperphysik im "Center for Spinelectronic Materials and Devices" der Universität Bielefeld promovieren zu dürfen. In den vergangen dreieinhalb Jahren durfte ich stark von seiner Erfahrung, seinem Engagement und Fachkompetenz profitieren. Weiterer Dank gehört Dr. Jan-Michael Schmalhorst für aufmunternde Worte und lehrreiche Stunden im Labor. Besonders hervorheben möchte ich an dieser Stelle die Betreuung durch Dr. Karsten Rott in allen Bereichen der Mikrostrukturierung (FIB, REM, SIMS & Lithographie). Die gemeinsame Zeit war mir fachlich, vorallem aber auch menschlich eine ganz besondere Freude.
Auch der kompletten Arbeitsgruppe möchte ich herzlich danken. Die vier Jahre sind für mich rückblickend wie im Flug vergangen, was nicht zu guter Letzt an dem wunderbaren Kollektivgefüge, dem tollen Kollegium und dem angenehmen Arbeitsklima gele-

gen hat. Ich werde euch alle vermissen - ganz besonders Andreas “Manni” Becker, Denis Dyck und Jan Krieft. Es war mir eine Ehre, ihr Guten!

Für aufregende Messzeiten und informative Diskussionen, sowohl fachlich wie auch menschlich, möchte ich mich persönlich bei allen Projektpartnern - besonders aber bei Prof. Dr. Wolfgang Wernsdorfer, Dr. Kiril Bosirov und Joachim Schönle vom Karlsruher Institut für Technologie, sowie dem Institut Néel in Grenoble bedanken. Hervorheben möchte ich auch Prof. Dr. Claudia Felser, Dr. Daniel Ebke, Dr. Chandra Shekhar und Benedikt Ernst vom Max-Planck-Institut für chemische Physik fester Stoffe; die letzten Jahre waren sehr lehrreich und haben mich vieler Erfahrung bereichert!

Ein ganz besonderes Dankeschön und ein großes Lob möchte ich an dieser Stelle an Torsten Hübner, Matthias Simonis, Oliver Reimer, Jan Haskenhoff, Thomas Lilienkamp, Michael Stührenberg und Hanno Meyer zu Theenhausen aussprechen. Dieses Grüppchen besonderer Physiker hat mich durch mein komplettes Studium begleitet. Sie haben aber auch in den letzten Jahren weiterhin dafür gesorgt, dass bei all der Arbeit der nötige Spass nicht zu kurz kam. Danke für eine großartige Zeit!

Ein großes Lob und ein noch viel größeres Dankeschön gebührt meiner geliebten Schwester Séverine Klett. Sie musste sich die ein oder andere Stunde mit dieser Arbeit um die Ohren schlagen - in dem verzweifelten Unterfangen diese Arbeit in “lesbares Englisch” zu übersetzen und die letzten eingeschlichenen Tippfehler aus zu merzen.

Weiterer Dank an dieser Stelle geht an meine Jugendfreunde: Alexander Vogt, Marc Kleinegees, André Lahl, Dominik Siede, Lars Bühren, Jan-Niklas Sieweke, Lennart Idensen und Stefan Kaminsky. Danke

Leute, ich schulde euch mehr als ich es hier in Worte zu fassen mag!
An dieser Stelle möchte ich nochmal einen großen Dank aussprechen, diesmal an meine ganze Familie die mich während meines Studiums bedingungslos unterstützt hat. Besonders bedanken möchte ich mich aber bei meinen Großeltern Willy & Magdalena Janke und Christa & Willi Klett, sowie meinen tollen Schwiegereltern, Sabine Möllering-Illner und Kurt Illner. Sie alle haben mir, vorallem in den letzten Jahren meines Studentendaseins, mit gelegentlichen Geldspritzen, gutem Rat, Geduld und Unterstützung jeglicher Art unter die Arme gegriffen.
Ich möchte hier an dieser Stelle meiner Freundin Corinna Illner danken, die mich in jeder Art und Weise in den vergangenen Jahren des Studiums und der Promotion zu unterstützen und aufzuheitern wusste. Ich danke dir von Herzen für deine erwiesene Geduld, die Mühe, sowie dein Verständnis und den gegebenen Rückhalt!
Der Abschluss der Danksagung ist meinen wundervollen Eltern, Heike und Volker Klett, gewidmet. Mit ihrer bedingungslosen Liebe, permanenten Unterstützung, unbegrenzter Geduld und emotionalen sowie mentalen Beistand haben Sie mich mein ganzes Leben lang begleitet. Durch ihren Rat, ihre Erfahrung und Führung war ich in der Lage alle die bisherigen Hürden zu meistern. Für all dies, ihr beiden, schulde ich euch mehr als ich jemals die Möglichkeit haben werde es auszudrücken zu können - Danke Mama, Danke Papa!